University of Alberta

Compensator transmission measurement and thickness verification

with an a-Si EPID

by

Geetha Vijayan Menon   ©

A thesis submitted to the Faculty of Graduate Studies and Research in partial

fulfillment of the requirements for the degree of Doctor of Philosophy

in

Medical Physics

Department of Physics

Edmonton, Alberta

Fall 2004

Canada

To
my family

ACKNOWLEDGEMENT

"If I have seen further than others, it is by standing upon the shoulders of giants."
<div align="right">

Sir Isaac Newton
</div>

I take this opportunity to express my gratitude to all those who contributed to my achievement through their advice or support. The first person I want to thank is my supervisor, Dr. Ron Sloboda, for it was a great pleasure to have conducted this research under his supervision. I am very grateful to him for ensuring my progress, for being constantly available for providing guidance and suggestions, for his patience in revising manuscripts and the thesis, and for his motivation. I admire him for his exemplary teaching skills and consider myself privileged to be one of his students. I am also grateful to all the faculty members, especially my committee members Dr. G. Greeniaus, Dr. R. Hooper, Dr. G. Fallone, Dr. R. Scrimger, and Dr. S. Pistorius for providing constructive and valuable comments for the improvement of the thesis.

I am also thankful to all the members of the Medical Physics department who have always been very helpful during the course of both my degrees. In particular, I would also like to thank Dr. Marc Mackenzie, the radiation therapists, staff of the mould room, machine room, and TMG for having helped me in my experimental work. I am also grateful to Ms. Sherry Connors for all her professional advice.

Special thanks goes to my buddy, Isabelle Gagné, for all the good times we had especially during the lunch and chat breaks. I would also like to thank my wonderful friends – Charlie, Brad, Charles, Teo, Steven, Tara, Heather, and the rest of the gang.

I am deeply indebted to my parents, who have always supported me in all my endeavors and been a constant source of inspiration and encouragement. I am also very grateful to my husband, Vijayan, and son, Shyam, for their love and understanding during the period of my research.

It is possible that I may have inadvertently forgotten to acknowledge someone, but my sincere thanks is extended to all my acquaintances at the Cross Cancer Institute, University of Alberta, and back home in India.

Table of Contents

List of Tables

List of Figures

smaller than the plotted symbols. Similarly the 95% confidence interval plots are not shown as they passed through the symbols.

List of Symbols

A x B	Field size
C	Contrast
$f(P)$	Calibration curve relating pixel value to ion chamber reading
Cu	Copper
d_{max}	Depth of maximum dose
E_L	Pixel position at the left edge of the slab in pitch calculation
E_R	Pixel position at the right edge of the slab in pitch calculation
f_{50}	Critical frequency
I_B	Background intensity
I_O	Object intensity
L	Physical length of slab used for pixel pitch measurement
L_P	Length of the image in number of pixels
M	Magnification factor at SDD with EPID positioned at 140 cm = 1.413
P_b	Average pixel value in the brightest region of the image
P_d	Average pixel value in the darkest region of the image
P_p	Pixel pitch
R^{comp}	Fluence reading with attenuator
R^D	Fluence reading on the day of any measurement
R^{open}	Fluence reading for open field
$R_{PV\,SYNC}$	Number of rows scanned per PV SYNC pulse
R_{tot}	Total number of rows of aS500 EPID
S_c	Collimator scatter factor
S_{EPID}	EPID scatter factor
S_p	Phantom scatter factor
t	Thickness normal to the top surface of compensator
t_{fr}	Frame time
t_P	Attenuation path length of a primary ray through the compensator
T_P	Primary transmission component

T_S	Scatter transmission component
T_T	Total transmission component
α	Constant in an exponential relation
η	Dose rate servo stability
κ	Hardening coefficient
$k_{\overline{FF}}$	Mean of flood field pixel values or scaling factor
μ_0	Initial attenuation of the incident beam
μ_{ss}	Effective linear attenuation coefficient for steel shot
θ	Angle between beam CAX and primary ray path
σ	Random image noise
ϕ_s^{comp}	Energy fluence of singly scattered photons from compensator
ϕ^{open}	Energy fluence for open field
$\mathfrak{R}$	Relative Unit

List of Abbreviations

ACPU	Acquisition central processing unit
a-Si	Amorphous silicon
CAP	Customer acceptance procedure
CAX	Central beam axis
CF	Compensator factor
CI	Corrected image
CNR	Contrast-to-noise ratio
CT	Computed tomography
DF	Dark field
DMLC	Dynamic multileaf collimator
DRR	Digital reconstruction radiograph
DRS	Dose rate servo
EPID	Electronic portal imaging device
FF	Flood field
Gy	Gray
IAS2	Image acquisition system 2
IC	Ion chamber
ICRU	International Commission on Radiation Units and Measurement
IDU	Image detection unit
IMRT	Intensity modulated radiation therapy
Linac	Linear accelerator
MeV	Mega Electron Volts (mono-energetic photons)
MLC	Multileaf collimator
ms	millisecond
MTF	Modulation transfer function
MU	Monitor unit
MV	Mega Volts (X-ray spectrum)
OAR	Off-axis fluence correction
OAX	Off-axis position

OFR	Off-axis fluence ratio measured for compensator QC
OI	Object image
PCB	Printed circuit board
PLS	Pulse length servo
PV	PortalVision
QA	Quality assurance
QC	Quality control
RMTF	Relative modulation transfer function
ROI	Region of interest
ROI_{CAX}	Region of interest along central beam axis
RU	Relative unit
SAD	Source-to-axis distance
SCD	Source-to-compensator distance
SD	Standard deviation
SDD	Source-to-detector distance
SED	Source-to-EPID distance
SLIC	Scanning liquid ion chamber
SPR[*]	Scatter-to-primary ratio (modified)
SSD	Source-to-surface distance
TFT	Thin film transistor
TLD	Thermoluminescent dosimeter
VBA	Visual basic application

CHAPTER 1: INTRODUCTION

1.1 RADIATION THERAPY

Radiation oncology is in a stage of rapid expansion with regards to its available therapeutic tools and our fundamental understanding of cancer. The in-depth understanding of oncology in the field of medicine has gone a long way since the discovery of x-rays and each step in the process of development has helped in improving cancer detection and treatment. Several ingenious modes of therapy have evolved in recent years, making significant breakthroughs in several areas of cancer treatment. With resourceful applications of imaging modalities like computed tomography (CT) and magnetic resonance imaging (MRI), the detection and localization of cancer has improved dramatically. For cancer treatment, radiation therapy (or radiotherapy) has proven to be one of the primary methods of care along with surgery, chemotherapy, and hormone therapy. Radiotherapy uses a stream of high-energy particles or waves, such as x-rays, gamma rays, and beta particles, to destroy or damage cancer cells. Radiotherapy is delivered as: (i) teletherapy (long-distance therapy), where the radiation from an external source such as a linear accelerator (linac), Co-60 unit, or orthovoltage unit is used, or as (ii) brachytherapy (short-range therapy), where a radioactive source is in contact with or in the proximity of the tumor. With both modalities, a high degree of dose conformality can usually be achieved in contemporary practice with respect to the treatment volume. For teletherapy, this has been accomplished with the recent introduction of conformal therapy and intensity modulated radiation therapy (IMRT), where high dose volumes are shaped using dynamic methods involving multi-leaf collimators (MLCs) and calculated using inverse planning methods [Br, 1988a; Br, 1988b; Bo, 1990].

The success of a radiotherapy treatment course depends on the dose distribution achieved by the radiation beam in the treatment volume [Br, 1997]. The fundamental intention of any newer treatment modality like 3D conformal radiotherapy is to increase local control of disease by delivering a high dose to the tumor volume while

1

reducing the level of normal tissue complication by sparing surrounding tissues or irradiating them to a minimal dose. This is achieved in practice by irradiating the treatment volume with radiation fields from different directions. With the introduction of multi-leaf collimators (MLCs), the field margins around the tumor can be more tightly defined, allowing increased prescribed dose to the treatment volume. Small changes in the dose distribution can significantly affect tumor control, however, and may increase normal tissue complications. For adequate control of disease at the tumor site with minimal hazard to the surrounding tissue, it is absolutely necessary to be treating with accurate treatment fields and doses [He, 1994]. According to the International Commission on Radiation Units and measurements (ICRU), the accuracy in dose delivery should be within ± 5%, or even lower in conventional radiotherapy [In, 1976; Du, 1984]. Some of the factors affecting the accuracy of radiation treatment are: incorrect alignment of the patient relative to the treatment beam, incorrect placement of shielding blocks, distortion of the patient (e.g. change in posture and weight loss), patient motion, motion of skin marks relative to the internal anatomy, organ motion, and mechanical misalignment of the treatment machine [Ha, 1973; Ra, 1985; Me, 1997]. To reduce negative outcomes due to treatment positioning inconsistencies, frequent monitoring of the patient position during treatment is crucial [Ma, 1974; Ve, 1982]. The need for exact positioning of patients just before and during radiotherapy treatment has become even more important in recent years, and is essential for high quality treatment.

1.2   PORTAL IMAGING IN RADIOTHERAPY

Superior radiotherapy treatment of cancer necessitates routine verification of the treatment setup and the dose delivered to assure the safety and quality of treatments, particularly complex ones such as IMRT [Ma, 1976; Ve, 1982]. Online verification of the treatment setup and proper patient positioning relative to the treatment beam is the goal of *portal imaging* (i.e. the imaging of different treatment fields or ports). Portal imaging was conceived with the idea of being able to image the

2

patient during treatment, by placing a detector (such as film) beyond the patient to capture the exit radiation, such that the treatment volume could be verified under actual treatment conditions. Munro has published a very interesting history of portal imaging dating back to the first recorded online image and extending up to modern electronic devices [Mu, 1995]. The first mention of portal imaging was for a case of esophageal cancer treated by rotation therapy using a 180 kVp x-ray beam that was viewed by a fluoroscopic screen, and corrections were performed remotely [Ne, 1942]. The use of films for portal imaging was introduced in 1951 for a treatment using a 2 MeV Van de Graaff generator [Ha, 1951]. Developments in film technology led to improvements in the contrast of port films for use in on-line imaging [Pe, 1960; Sp, 1962]. With the introduction of slow and wide latitude films, the imaging time could be extended for the whole length of the treatment [Sw, 1966; Ma, 1976]. In the field of port films, the latest improvement by means of increased quantum efficiency has been brought about by the enhanced contrast localization (EC-L) system where a fine grain, very low speed, high gamma film is sandwiched between two phosphor screens with a 1 mm thick copper front plate. Alternatively, in 1958, non-film portal imagers were introduced for online treatment verification by means of a television-roentgen systems that used an x-ray image intensifier and TV camera for imaging [St, 1958; Wa, 1958]. Since the late 1980s several electronic devices, such as the camera-based detector [Mu, 1990a], ion chamber array [Me, 1990], amorphous silicon flat panel [An, 1992], and amorphous selenium detector [Wa, 1996], have been introduced for real-time imaging of megavoltage treatments.

Over the years the role of portal imaging devices has evolved from being just a setup verification tool to also include transit dosimetry measurements. These two major uses of portal imagers are described in the following sub-sections.

1.2.1 Treatment Field Setup Verification

The main objective of portal imaging is to determine the accuracy of patient positioning for setup verification. A portal image shows the position of the bony

anatomy relative to the edges of the radiation field and hence provides a measure of verification of the treatment [Mu, 1998]. Although image quality at megavoltage energies is poorer than at diagnostic energies, a portal image is considered mandatory as a legal record and represents good clinical practice. Portal images are obtained using either slow speed films enclosed in cassettes lined with copper screens or electronic imaging devices. The images thus obtained are compared with localization images from a treatment simulator or with digitally reconstructed radiographs (DRRs) to confirm the treatment setup accuracy [Cr, 1996; Gi, 1998]. Portal imaging has also been helpful in detecting the effect of organ motion in radiotherapy treatment, which is conventionally dealt with by using implanted radio-opaque markers, adding extra margins around the gross tumor volume, or by respiratory gating [We, 1997]. Significant research has gone into tracking organ motion, especially of the prostate, using portal imaging techniques [Kr, 1998; Wu, 2001; Li, 2003].

1.2.2 Dosimetric Verification

Portal images contain dosimetric as well as geometric information. The use of portal imaging for dosimetric verification has recently generated a lot of interest amongst researchers [Fi, 1993; He, 1995; Bo, 1997a]. When compared to detectors such as diodes and TLDs that can only measure point doses, portal imaging devices offer an advantage in being able to make measurements across the entire radiation field.

Two main goals in performing portal dosimetry are to obtain the transmission dose at the detector plane behind the patient from portal images (Fig. 1.1), and to predict the dose in the patient exit plane from these images [Mc, 2004]. Information from the detectors used for portal dosimetry (such as optical densities from films or pixel values from digital devices) is initially translated into total transmission dose at the detector plane using appropriate algorithms that also correct for field size and patient thickness dependencies, and account for any non-linearity of response of the detector used. Several ingenious methods have been investigated to predict exit doses

4

from the transmission dose estimated from portal images. The exit dose can be predicted by first separating the scatter from the primary component, back-projecting to the exit dose plane, and then using Monte Carlo and analytical models to generate pencil beam kernels for dose calculation [Sw, 1996; Mc, 2000; Sp, 2000]. In the measurement of transmission dose, there will be significant scatter contribution from the patient and beam modifying devices in the beam path. Further, exit dose distributions can be used to determine mid-plane doses [Bo, 1998] taking into consideration any inhomogeneities in the path of interest.

Dosimetric measurements made from portal images can be used for ascertaining the quality of treatment by either (i) comparing the exit dose to the treatment planned exit dose, or (ii) by calculating the transmission dose using a physical model and comparing it to the measured transmission dose [La, 2001]. A limitation is that differences between measured and planned doses can arise if there are changes in the patient setup or condition (e.g. weight loss) or in the output of the therapy machine [Mu, 1999]. Portal dosimetry is still an investigational area, but with considerable potential to improve the accuracy of radiotherapy delivery.

1.3 ELECTRONIC PORTAL IMAGING DEVICES (EPIDs)

Port films are currently being replaced by electronic portal imaging devices. First introduced over a decade ago, EPIDs are filmless imaging systems that offer real time operation in digital mode for online verification of the treatment setup. An EPID is designed to improve the quality of patient treatment by enhancing the geometric accuracy of the setup (Fig. 1.2). It accomplishes this by monitoring the positions of the radiation beam, shielding blocks, and other accessories with respect to the patient. Digital images of the treatment port can be captured and displayed throughout each treatment fraction. Any patient positioning errors made evident by the EPID images may be corrected before continuing the patient's treatment, to assure accurate delivery of the planned dose. The major advantage of EPIDs is that they produce digitized images immediately for on-line review and approval of patient positioning, thereby

5

reducing setup time and systematic errors. This in turn speeds up treatment delivery time and improves the accuracy of both conventional and sophisticated treatments, including IMRT.

The specific advantages of EPIDs over port films are that [Cu, 1997; St, 1998]: (i) the image is directly obtained in a digital format, permitting the software enhancement of image contrast and electronic archiving [Me, 1990], (ii) the radiation beam parameters used in treatment planning or equipment control can be measured and verified, (iii) there is better determination of field displacements, (iv) no screen-film or storage-phosphor cassettes are needed, (v) soft copy image display is possible, and (vi) automated image comparison is feasible (would replace subjective assessment of alignment and increase the speed of the process).

Although EPIDs enable a megavoltage X-ray image of the treatment field to be recorded and registered with a reference image during treatment with high-resolution [Jo, 1991], the image contrast is unfortunately inherently low due to the high-energy beam. Moreover, there is the possibility of out-of-plane rotation of the patient during setup, resulting in complex distortions in the projected images. Consequently, the registration of portal images and their quantitative processing is a very challenging task. Another potential drawback is a smaller field of view arising because of the typically larger isocenter to detector distance for EPIDs compared to film cassettes.

1.3.1 Types of EPIDs

Following the introduction of EPIDs for clinical use in the late 1980's, there have been three distinctly different imaging devices made commercially available. These are categorized as first generation types and include the video-based and ionization chamber systems, followed by the newer amorphous silicon (a-Si) flat panel EPIDs [Bo, 1992; Mu, 1995; He, 2001; An, 2002].

1.3.1.1 Video based EPIDs

Generally, video-based systems make use of metal plates in combination with phosphor screens to form an image that is viewed using a video camera. Early video-based EPIDs used mirrors for the transfer of the signal to the camera, which was later followed by fiber-optic coupling for better performance. Both types are discussed in the following paragraphs.

The mirror-based video (or fluoroscopic) system consists of an assembly of a metal plate, fluorescent screen, mirror, and camera enclosed in a light-tight housing. Interaction of incident radiation in the metal (~1.0 – 1.5 mm copper, steel or brass) creates high-energy electrons that produce fluorescence in a gadolinium oxysulphide (Gd_2O_2S:Tb) phosphor screen. The resulting light that diffuses through the screen is directed by a 45° mirror to a lens-camera combination (Fig. 1.3) where the analog images are digitized to produce a video signal. Image quality can be improved by adding digital image frames in a frame buffer and by applying dark current corrections to reduce quantum noise [Gr, 2002]. For use in dosimetry the images have to be corrected for optical "cross talk" and for the modestly non-linear radiation response of the EPID [Pa, 1998b]. The advantage of this imager is that the detector covers the treatment field such that almost the entire radiation field can be sampled at high acquisition rates [Ma, 1997, Pa, 1998b]. Herman *et al.* have estimated that ~2 - 4% of the incident radiation interacts to produce the measurable signal, depending on the thickness of phosphor [He, 2001]. A major drawback is the poor light collection efficiency because of extensive scatter of light photons in the phosphor. The signal generated in the camera is from those light photons that exit from the phosphor within a cone subtended by the lens of the camera (~0.1% to 0.01% of photon emitted) [Mu, 1995]. The rest of the light signal is scattered in all directions after it exits the phosphor. This reduced light collection efficiency leads to poor image quality [An, 1996]. Improvement in this area has involved experimenting with various types of metal plates, varying the thickness of the phosphor, and using different cameras and processing mechanisms for optimum signal generation [Mu, 1990a; Bi, 1997; Dr,

7

2000]. Over and above these drawbacks, the mirror based EPIDs are very bulky causing difficulty in linac movement.

The fiber optic video system is similar to the mirror-based EPID except that it incorporates a 2-D array of fiber optic image reducers [Wo, 1990] in place of the mirror (Fig. 1.4) that was found to be cumbersome and also contributed to glare. The electrons generated in the copper plate produce fluorescence in the phosphor, which is directed to the fiber optic channels of polystyrene in acrylic cladding. The light transfer depends on the differences in refractive indices of the polystyrene and acrylic and follows the principle of total internal reflection [Bo, 1992]. The main drawback of this EPID is that small irregularities in the shape and alignment of the fiber bundles cause significant distortions in the image.

1.3.1.2 Scanning liquid ionization chamber (SLIC) EPID

The concept of ion chamber EPIDs was developed by Meertens *et al.* at the Netherlands Cancer Institute in the mid-1980s [Me, 1985; Va, 1988, Me, 1990]. Varian has commercialized this imager as its PortalVision SLIC EPID. These EPIDs are very similar in operation to conventional air-filled ion chambers except that a liquid is used for increased signal detection because of its greater density. The detector has 256 x 256 pairs of perpendicularly oriented electrodes on two printed circuit boards (PCBs) placed on either side of a 1 mm thick liquid layer of iso-octane (Fig. 1.5(a)), a microprocessor-based controller, and a data acquisition system (Fig. 1.5(b)). The system can be connected to the linac gantry by a retractable arm. The first set of electrodes is connected to a 256-channel electrometer system and the second set to a 256-channel high voltage (HV) switch system. The liquid layer serves as the ionization medium between the two PCBs that also provide electrical shielding and structural support. There is a front screen (1 mm thick stainless steel/plastoferrite) for radiation buildup. The detector is functionally equivalent to a matrix of individual ion chambers of size 1.27 mm x 1.27 mm x 1 mm, yielding a full field of view of about 325 x 325 mm. This device with its compact size has good geometric reliability. A limitation here

8

is that of quantum utilization, as only one image receptor (HV line) is read at a time. Since the 20 ms sampling time for each row is fairly long, a SLIC EPID can only measure dose rate, and raw signals must be extensively processed to obtain dose [Es, 1996]. The pixel value to dose relation for this EPID follows a square root response. Background signals are generated in the electrometers and the ion chambers, whose sensitivities change with time, and therefore the detector requires routine calibration. Image enhancement is performed on low contrast and unsharp megavoltage images using methods such as linear contrast enhancement, 3 x 3 spatial domain convolution filtering, and global histogram modification [Mu, 1995]. Arithmetic image operations make it possible to compare images, generate double exposures, and average images.

1.3.1.3 Amorphous silicon flat-panel EPID

The latest commercial EPID to enter the market is the a-Si flat panel EPID that provides high quality portal images with doses as little as ~2 cGy as compared to ~5 cGy for film. The EPID utilizes a light sensitive a-Si panel (Fig. 1.6(a)) with a metal plate for buildup and a phosphor layer that emits optical photons when irradiated. The a-Si panel is a glass plate carrying a matrix of pixels, each consisting of an amorphous silicon photodiode to convert light quanta to electron-hole pairs and an amorphous thin film transistor (TFT) or field-effect transistor (FET) switch for readout. The pixel switch (or active element) is connected to a pixel storage capacitor that holds the image charge induced by the incident radiation (Fig. 1.6(b)) [An, 1992]. The electronics to drive the switches and to read the charge captured is located in the detector as well. The arrays are read out sequentially by switching the rows to a conducting state by means of the gate control circuitry (Fig. 1.6(c)). Further details of the operation of a particular commercial imager can be found in Section 2.2.2.1.

An a-Si EPID offers many operational advantages. The most important one of these is its superior image quality which derives from its use of ~50% of the light emitted by the scintillator, a much better light transfer efficiency than that achieved by video-based EPIDs [An, 2002]. Other advantages include its linear dose response [An,

9

1998], its high resistance to radiation damage [Bo, 1996], and its versatility for radiographic and fluoroscopic applications [An, 1993].

1.3.2 Applications of EPIDs in Dosimetry

Ever since the introduction of EPIDs for therapy verification, several investigators have attempted to use the devices for dosimetric measurements. The earliest studies were aimed at verification of the field shape and other linac setup parameters [Bi, 1992; Ki, 1993; Va, 1993]. Following the initiative of Fiorino to use port films for patient dosimetry [Fi, 1993] and further research done with EPIDs, their application in portal dosimetry began in the mid-1990s. One of the earliest works by Kirby *et al.* used a camera-based EPID to measure exit doses to within 3% of values obtained with a silicon diode [Ki, 1995]. Heijmen *et al.* used a Philips SRI-100 fluoroscopic EPID to relate portal doses to the image grey scale measured with the EPID [He, 1995]. Another Netherlands group in 1996 published a transmission dose rate measurement study using the SLIC EPID for different phantom-detector geometries, in which measurements were compared with ion chamber data [Es, 1996]. A year later the same group obtained 2D exit dose estimates having an accuracy of < 2% using a convolution model suggesting the use of EPIDs as an alternative to ion chamber dosimetry [Bo, 1997a]. Interest in portal dosimetry research increased with the use of EPIDs for patient setup of complicated treatments such as those involving dynamic multileaf collimators (DMLCs) [Pa, 1998b]. Since 1999 a significant amount of work has also been done with a-Si EPIDs to employ this latest generation device for dose measurement. As mentioned earlier, the strengths of this EPID are its linear dose response, good detection efficiency, and relatively fast readout. One of the first reported studies involved relative dosimetry measurements by El-Mohri [El, 1999], which was followed by several major contributions [Mc, 2001; Gr, 2002; Ki, 2003]. A recent milestone in the dosimetric application of EPIDs for dosimetry has been their use for the verification of IMRT treatments [Gr, 2003; Wa, 2003]

10

A major area of use of EPIDs has been in tracking prostate motion using radio-opaque markers. Vigneault *et al.* used daily on-line EPID images to assess prostate movement with respect to pelvic bony structures [Vi, 1997]. Significant differences in portal dose images compared with planned dose distributions derived from CT data were observed by Kroonwijk for prostate cancer patients because of variations in rectal filling [Kr, 1998; St, 2000]. Gold markers as small as 1 mm were used by Nederveen *et al.* to successfully track organ motion automatically with respect to a fixed reference point at the field boundary using portal images [Ne, 2001]. Other interesting studies involving EPIDs include their use in breathing synchronized radiotherapy [Ku, 1999] and for digital mammography [Ve, 2000].

EPIDs have also been employed to design and perform quality control of custom-made compensators. Yin [Yi, 1994] and Roback [Ro, 1995] used transmission dosimetry to evaluate compensators. Evans describes a method for calibrating a SLIC EPID to obtain radiological thickness maps for use in designing breast compensators [Ev, 1995]. Low *et al.* compared EPID measured fluence profiles to intended fluence profiles for compensating filters, and found agreement to within 3% [Lo, 1996b]. In 1999, Pasma *et al.* developed a method to determine the 2D thickness profile of a compensator using a fluoroscopic EPID to an accuracy of 0.5 mm [Pa, 1999]. In our work we have used an a-Si EPID to perform similar measurements, an overview of which is given in the following section.

1.4 COMPENSATORS

In radiotherapy, conforming the delivered dose distribution to the planning target volume is a fundamental objective. To obtain a desired shape for the isodose distribution, several techniques have been incorporated in treatment practice such as the use of multiple fields (treatment with radiation portals from different directions), bolus (tissue equivalent material placed in contact with the body), wedges, and tissue-compensators (beam modulators placed away from the body) [Kh, 1994]. Compensators are more practical for megavoltage treatments since bolus creates

11

buildup of dose on the skin, thereby resulting in the loss of skin-sparing. Custom-made compensators serve as filters to modulate the radiation beam in the presence of tissue inhomogeneities, variations between beam entry and exit points, and variations in source-to-skin distance. Lately, they have also been used for IMRT.

1.4.1 Types of Compensators

Compensators are designed using the topographical data of the patient contour through which the radiation field is directed [Wi, 2000] or from a modulation matrix produced by the treatment planning system using CT data [Me 2003]. The required shape is then determined by calculating necessary thicknesses on a two-dimensional grid. Several different methods and materials are used to construct compensators. Some of the criteria for choosing compensator material are that they should (i) have suitable densities (too high will result in decreased transmission and too low in increased thicknesses), (ii) offer reproducible production, (iii) be reusable, and (iv) have skin sparing effect [Va, 1995]. Materials that have been used for compensator manufacture include aluminum [El, 1959], wax [Bo, 1974], solid lead [Cu, 1976], lead sheets [Le, 1974], acrylic [Ro, 1995], Lipowitz metal [Lo, 1995], and stainless steel granulates [Va, 1995]. The compensator is often fabricated by machining solid material or pouring molten material into a mould. In our center, steel shot is used as the compensator material in milled Styrofoam moulds [see Section 4.1].

1.4.2 Compensator Verification

Since compensators are custom clinical accessories, it is recommended that their accuracy in terms of size, shape, thickness variation, and mounting be confirmed before the commencement of treatment [Fr, 1998]. There are no standard procedures for verification of compensators; therapy clinics usually follow their own protocols developed in-house. Conventional methods of compensator quality control (QC) involve ion chamber or film measurements of the energy fluence transmitted through the compensator. In our center, the compensator factor (ratio of energy fluences for a

compensated to an open field on the central beam axis) and four off-axis fluence ratios (ratio of energy fluence at an off-axis position to that along the central axis) are determined. The energy fluences are measured with an ion chamber at a depth of 5 cm in a water equivalent phantom, at isocenter. The main drawbacks to ion chamber and film techniques are the tediousness in measuring several off-axis factors in the case of the former, and the significant processing and readout time associated with the latter. These inefficiencies warrant an alternative technique that enables faster verification without compromise in measurement accuracy. This thesis develops such a technique using an a-Si EPID (see Sections 1.5.4 and 1.5.5).

1.5 OBJECTIVES AND STUDIES PERFORMED

Of the several types of EPIDs introduced over the past two decades, this work makes use of an a-Si EPID [Mu, 1995; An, 2002]. Quite recently, the use of a-Si EPIDs has expanded beyond patient set-up verification to include applications such as measurement of delivered dose, verification of photon beam flatness/symmetry, and compensator design and verification [Mc, 2001; Gr, 2002; Me, 2003]. The goal of this work was to employ a commercial a-Si EPID for compensator quality assurance purposes by studying its operating characteristics and suitability for this application, and by developing the necessary methodology. The specific objectives of this study are briefly discussed in the following sections.

1.5.1 EPID Operating Characteristics

At the commencement of this work in 2001 the Varian PortalVision aS500 EPID (Varian Medical systems, Palo Alto, CA) based on amorphous silicon technology had just entered the commercial market. Since our primary objective with this EPID was to employ it for dosimetric purposes, we needed first to determine appropriate operating parameters. Hence initially after acceptance we made a detailed study of several operating parameters to determine suitable values for subsequent imaging and dosimetric applications.

13

1.5.2 EPID Quality Assurance[♦]

After EPID installation and acceptance, periodic monitoring of its mechanical features, image quality and operational consistency is necessary. Although each vendor demonstrates compliance with a set of performance specifications at acceptance, it is essential for good clinical practice to regularly monitor these specifications in order to maintain the quality of EPID performance [He, 2001]. Our objective therefore was to perform a longitudinal quality assurance (QA) study[†] for the aS500 EPID, making use of a variety of established methods to assess image quality and dose response stability.

1.5.3 Compensator Quality Control[*]

After characterizing the EPID operating parameters and evaluating its performance, we employed the detector to make dosimetric QC measurements for custom-made compensators. In this work, our objective was to develop the methodology to use the aS500 EPID as a replacement detector for an ion chamber in a water equivalent phantom, traditionally used clinically. Although compensator verification with fluoroscopic and SLIC EPIDs had been reported earlier [Lo, 1996b; Pa, 1999], the use of a-Si EPIDs had not yet been investigated.

1.5.4 Compensator Thickness Measurements[*]

Having established the capacity of the aS500 EPID to serve as an ion chamber replacement for compensator QC, in subsequent work we investigated the use of the

---

[♦] G. V. Menon and R. S. Sloboda, "Quality assurance measurements of a-Si EPID performance," Medical Dosimetry. **29**, 11-17 (2004).

[†] A series of QC measurements performed over an extended time period.

[*] G. V. Menon and R. S. Sloboda, "Compensator quality control with an amorphous silicon EPID," Medical Physics. **30**, 1816-1824 (2003).

[*] G. V. Menon and R. S. Sloboda, "Compensator thickness verification using an amorphous silicon EPID," Medical Physics. **31**, 1-13 (2004).

14

EPID to measure 2-D compensator thickness distributions. The objective was to make a comparison with an intended distribution in order to verify the accuracy of compensator fabrication and mounting. Once again, such measurements had not yet been performed with an a-Si EPID.

1.6 OVERVIEW OF THE THESIS

The thesis is logically organized in six chapters. Chapter 2 contains a detailed description of the Varian PortalVision aS500 EPID used for this work, its clinical acceptance criteria, and the selection of suitable operating parameters for dosimetric purposes. Chapter 3 reports the results of a longitudinal quality assurance study of the performance of the EPID in terms of image quality and dosimetric quality. Chapter 4 presents an investigation of the use of the aS500 EPID as an ion chamber replacement in an existing compensator QC protocol. This chapter presents the basic approach underlying the use of the EPID as a dosimetric tool, and an analysis of experimental results obtained. A more complete form of compensator verification strategy involving measurement of the compensator 2-D thickness distribution is presented in Chapter 5. Here transmission measurements are combined with a model of primary transmission of the linac beam through a compensator to determine the thicknesses. Finally, Chapter 6 summarizes the principal findings, giving an assessment of the practical problems, the success of the work, and opportunities for future studies in this area.
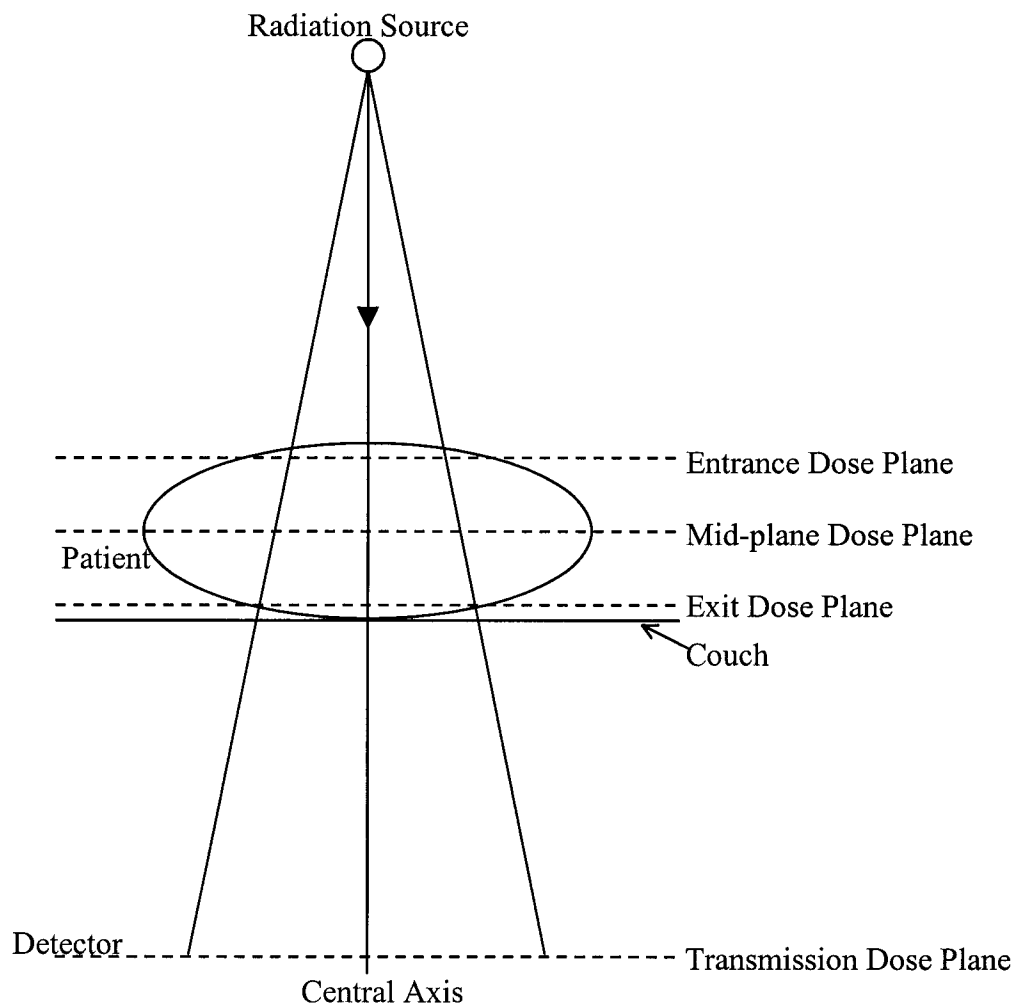
Figure 1.1: Schematic illustration of the different dose planes of interest in portal dosimetry [Bo, 1998].

Entrance dose plane: defined at the depth of dose maximum on the central axis.

Mid-plane dose plane: halfway between the entrance and exit dose planes perpendicular to the central beam axis.

Exit dose plane: defined at the depth of dose maximum upstream from the exit surface on the central axis.

Transmission dose plane: defined at the depth of dose maximum in a radiation measuring system.

16
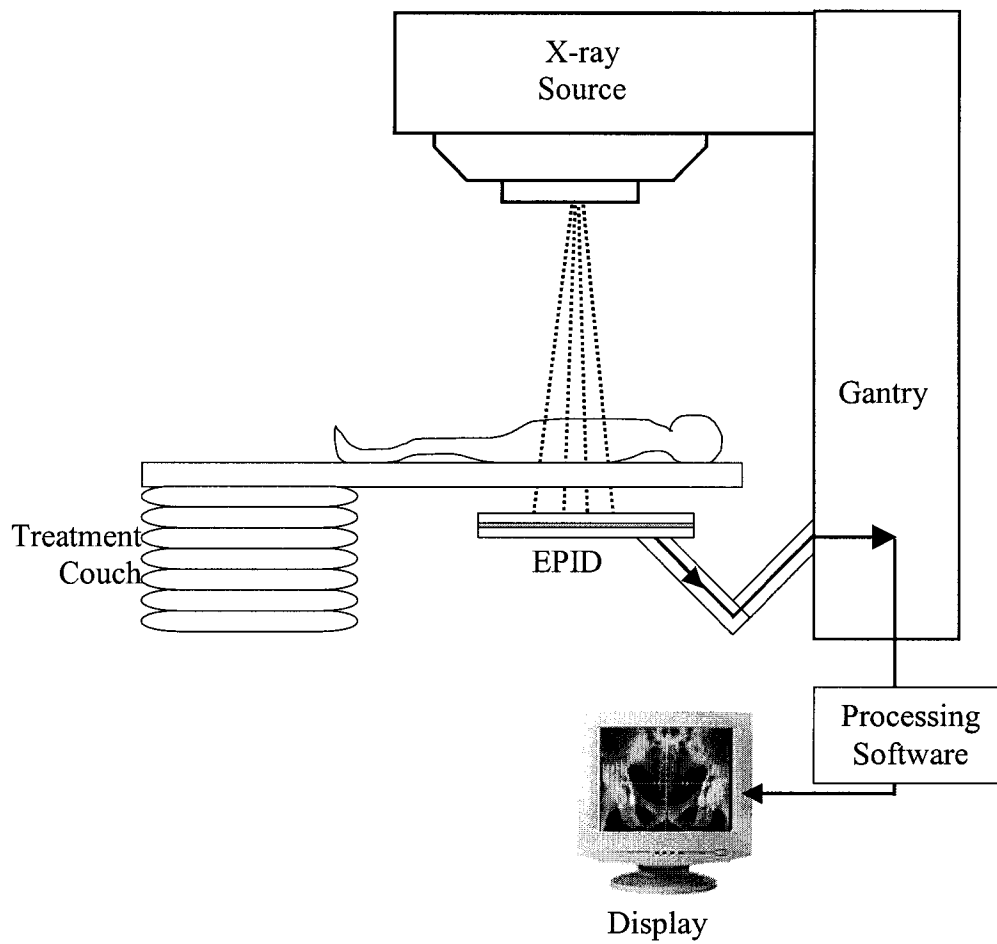
Figure 1.2: Schematic representation of an a-Si portal imaging setup for treatment verification.

17

Metal +
Phosphor screen

Mirror

Camera

Lens
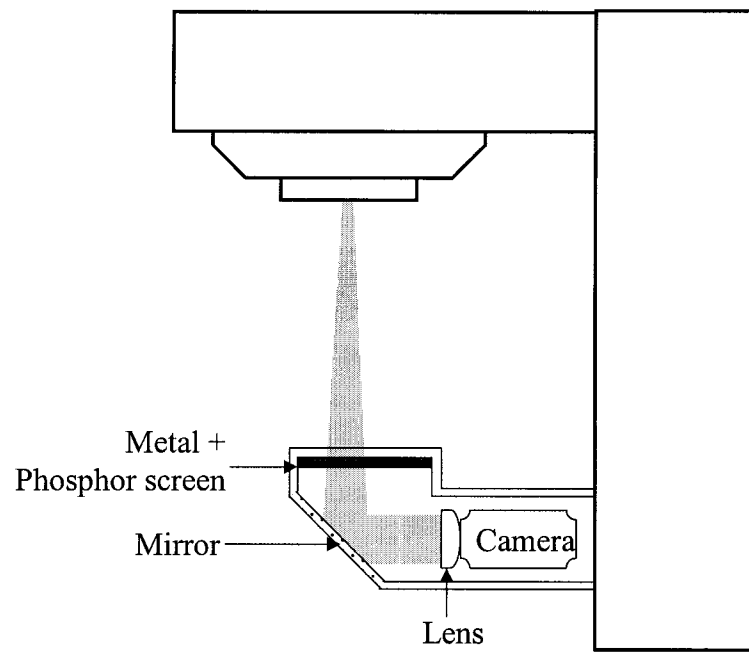
Figure 1.3: A mirror-based video system [Mu, 1995].

18
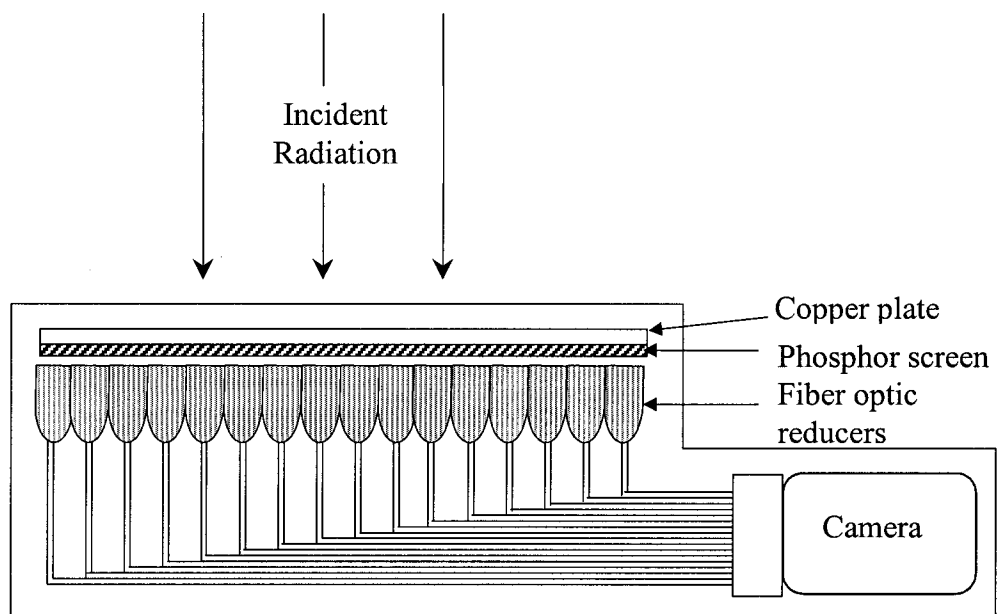
Figure 1.4: A fiber optic video system [Bo, 1992].

(a)

Incident
Radiation

Upper stabilizing plate

Buildup

256 x 256 perpendicularly arranged electrodes

Upper electrode plate

Iso-octane layer

Lower electrode plate

Lower stabilizing plate

(b)

GANTRY

Electrometer Amplifiers

Control Electronics

Control Unit + Display

Ionization Chamber Matrix

High Voltage Switches
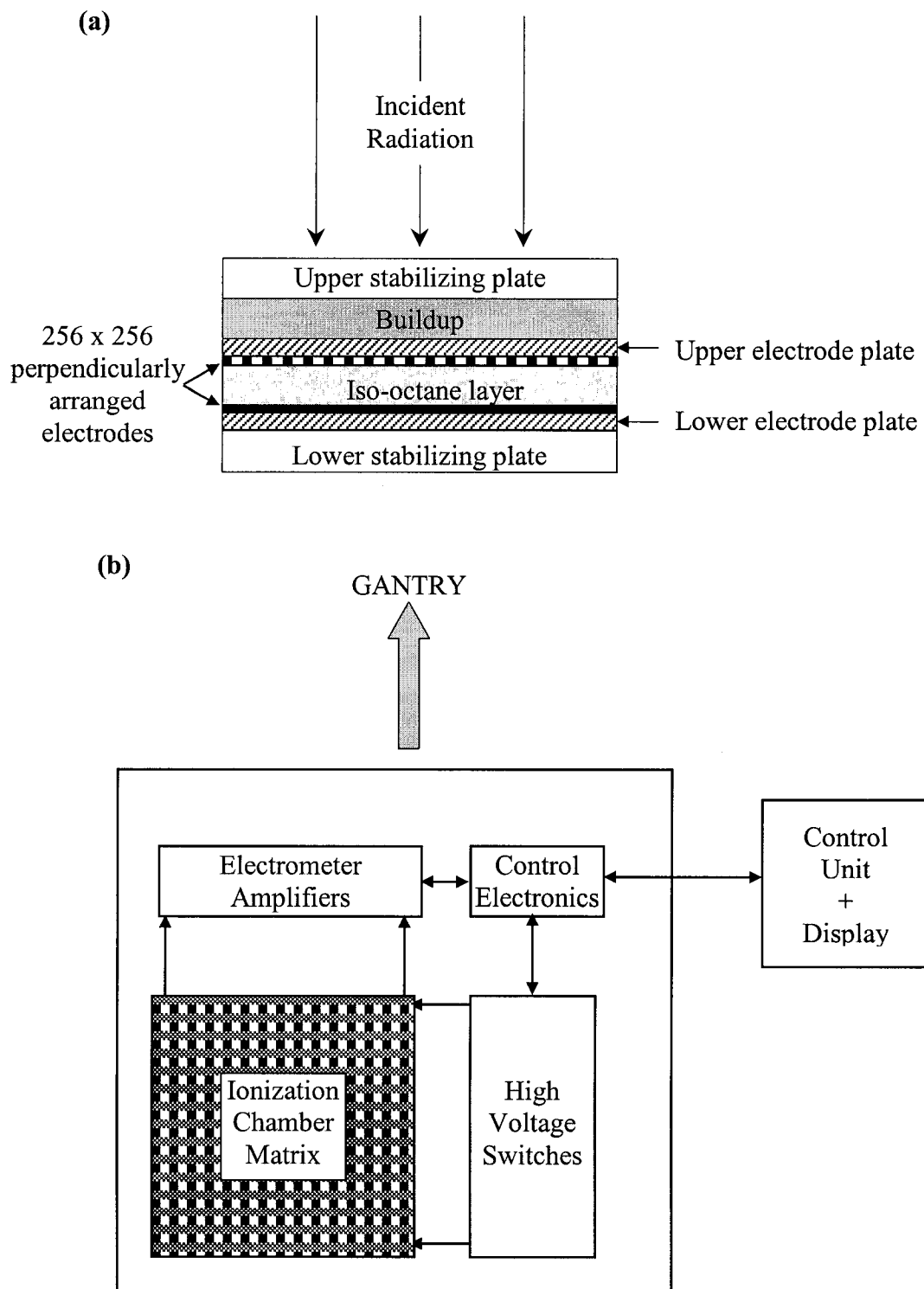
Figure 1.5: **(a)** Cross section (not to scale), and **(b)** schematic representation of a SLIC EPID.

20

(a)

Incident
Radiation

Metal Plate
Phosphor Screen
a-Si Photodiode

(b)

Data
Line

Bias
Line
Photodiode

TFT

Gate
Line

(c)

GANTRY

Readout
Electronics

Interface
Electronics

Control
Unit
+
Display

a-Si
Pixel
Matrix

Drive
Electronics
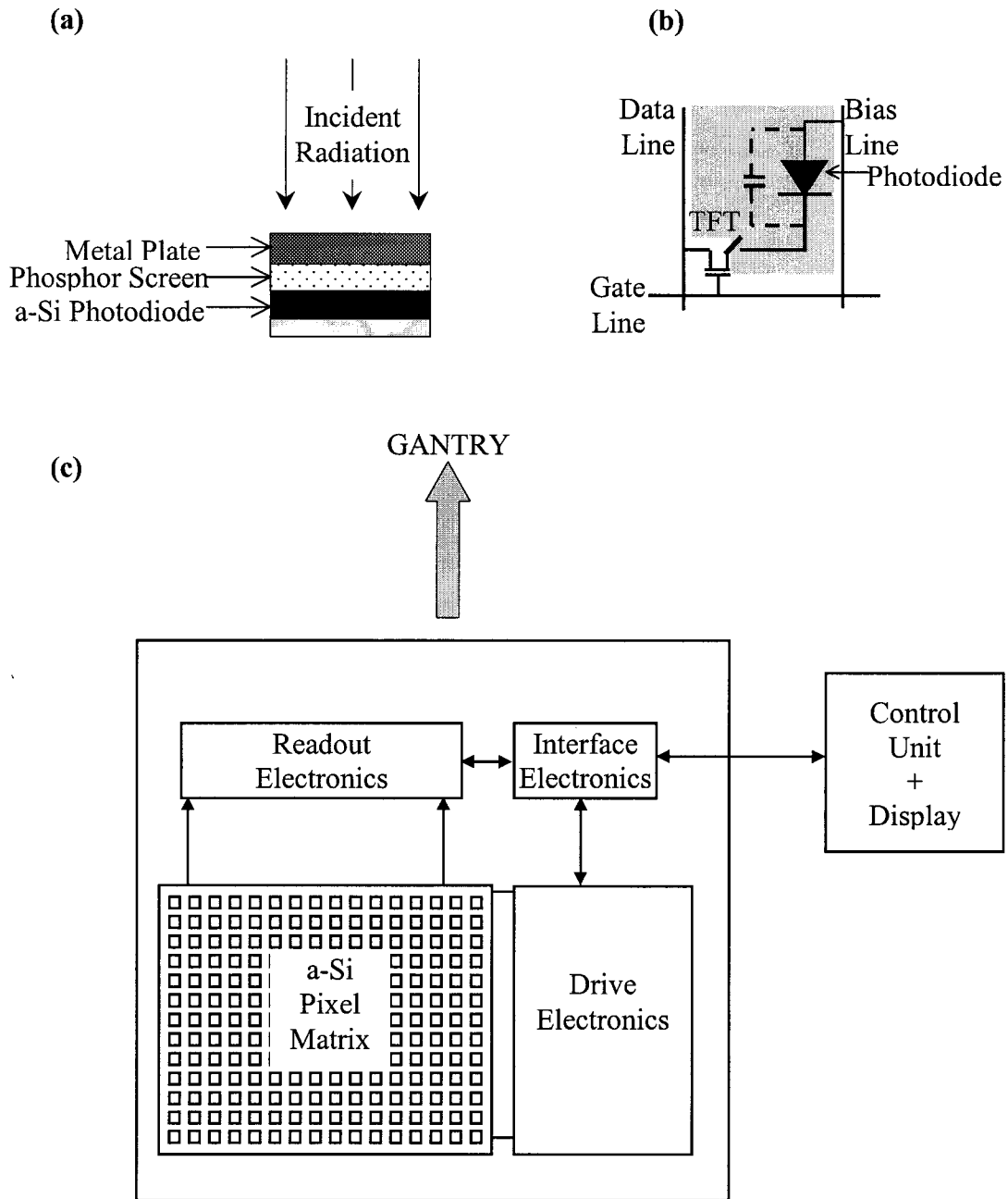
Figure 1.6: **(a)** Three main constituents of an a-Si EPID detector stack (not to scale), **(b)** details of an a-Si pixel, and **(c)** schematic drawing of a typical a-Si EPID illustrating the main component assemblies.

1.7 REFERENCES

[An, 1992]   L. E. Antonuk, J. Boudry, W. Huang, D. L. McShan, E. J. Morton, M. J. Longo, and R. A. Street, "Demonstration of megavoltage and diagnostic x-ray imaging with hydrogenated amorphous silicon arrays," Medical Physics. **19**, 1455-1466 (1992).

[An, 1993]   L. E. Antonuk, J. Yorkston, W. Huang, J. H. Siewerdsen, and R. A. Street, "Considerations for high frame rate operation of two dimensional a-Si:H imaging arrays," Materials Research Society Symposium. Proceedings **297**, 945-950 (1993).

[An, 1996]   L. E. Antonuk, J. Yorkston, W. Huang, H. Sandler, J. H. Siewerdsen, and Y. El-Mohri, "Megavoltage imaging with a large-area, flat-panel, amorphous silicon imager," International Journal of Radiation Oncology Biology Physics. **36**, 661-672 (1996).

[An, 1998]   L. E. Antonuk, Y. El-Mohri, W. Huang, K-W Jee, J. H. Siewerdsen, M. Maolinbay, V. E. Scarpine, H. Sandler, and J. Yorkston, "Initial performance evaluation of an indirect-detection, active matrix flat-panel imager (AMFPI) prototype for megavoltage imaging," International Journal of Radiation Oncology Biology Physics. **42**, 437-454 (1998).

[An, 2002]   L. Antonuk, "Electronic portal imaging devices: a review and historical perspective of contemporary technologies and research," Physics in Medicine and Biology. **47**, R31-R65 (2002).

[Bi, 1992]   J. Bijhold, K. G. A. Gilhuijs, and M. van Herk, "Automatic verification of radiation field shape using digital portal images." Medical Physics. **19**, 1007-1014 (1992).

[Bi, 1997]   J-P. Bissonnette, I. A. Cunningham, and P. Munro, "Optimal phosphor thickness for portal imaging," Medical Physics. **24**, 803-814 (1997).

[Bo, 1974]   R. J. Boge, R. W. Edland, and D. C. Matthes, "Tissue compensators for megavoltage radiotherapy fabricated from hollowed Styrofoam filled with wax", Radiology. **111**, 193-198 (1974).

[Bo, 1990]   T. Bortfeld, J. Bürkelbach, R. Boesecke, and W. Schlegel, "Methods of image reconstruction from projections applied to conformation radiotherapy," Physics in Medicine and Biology. **35,** 1423–1443 (1990).

[Bo, 1992]   A. L. Boyer, L. Antonuk, A. Fenster, M. van Herk, H. Meertens, P. Munro, L. E. Reinstein, and J. Wong, "A review of electronic portal imaging devices (EPIDs)," Medical Physics. **19,** 1-16 (1992).

[Bo, 1996]   J. M. Boudry and L. E. Antonuk, "Radiation damage of amorphous silicon, thin-film, field effect transistors," Medical Physics. **23,** 743-754 (1996).

[Bo, 1997a]   R. Boellaard, M. van Herk, H. Uiterwaal, and B. J. Mijnheer," Two-dimensional exit dosimetry using a liquid filled electronic portal imaging device and a convolution model," Radiotherapy and Oncology. **44,** 149-157 (1997).

[Bo, 1998]   R. Boellaard, M. Essers, M. van Herk, and B. J. Mijnheer, "New method to obtain the midplane dose using portal in vivo dosimetry," International Journal of Radiation Oncology Biology Physics. **41,** 465-474 (1998).

[Br, 1988a]   A. Brahme, "Accuracy requirements and quality assurance of external beam therapy with photons and electrons," Acta Oncologica. Supplement **1,** Chapter 2:9–15 (1988).

[Br, 1988b]   A. Brahme, "Optimization of stationary and moving beam radiation therapy techniques," Physics in Medicine and Biology. **12,** 129–140 (1988).

[Br, 1997]   A. Brahme, "The need for accurate target and dose specifications in conventional and conformal radiation therapy: an introduction," Acta Oncologica. **36,** 789-791 (1997).

[Cr, 1996]   C. L. Creutzberg, V. G. M. Althof, M. de Hoog, A. G. Visser, H. Huizenga, A. Wijnmalen, and P. C. Levendag, "A quality control study of the accuracy of patient positioning in irradiation of pelvic fields.

23

International Journal of Radiation Oncology Biology Physics. **34**, 697–708 (1996).

[Cu, 1976] J. R. Cunningham, D. J. Wright, H. P. Webb, I. J. Rawlinson, and P. M. K. Leung, " A semi-automatic cutter for compensating filters," International Journal of Radiation Oncology Biology Physics. **1**, 355-358 (1976).

[Cu, 1997] A. Curtin-Savard and E. B. Podgorsak, "An electronic portal imaging device as a physics tool," Medical Dosimetry. **22**, 101-105 (1997).

[Dr, 2000] D. G. Drake, D. A. Jaffray, and J. W. Wong, "Characterization of a fluoroscopic imaging system for kV and MV radiography," Medical Physics. **27**, 898-905 (2000).

[Du, 1984] A. Dutreix, "When and how can we improve precision in radiotherapy," Radiotherapy & Oncology. **2**, 275-292 (1984).

[El, 1959] F. Ellis, E. J. Hall, and R. Oliver, "A compensator for variations in tissue thickness for high energy beams," British Journal of Radiology. **32**, 421-422 (1959).

[El, 1999] Y. El-Mohri, L. E. Antonuk, J. Yorkston, K. –W. Jee, M. Maolinbay, K. L. Lam, and J. H. Siewerdsen, "Relative dosimetry using active matrix flat panel imager (AMFPI) technology," Medical Physics. **26**, 1530-1541 (1999).

[Es, 1996] M. Essers, R. Boellaard, M. van Herk, J. H. Lanson, and B. J. Mijnheer, "Transmission dosimetry with a liquid-filled electronic portal imaging device," International Journal of Radiation Oncology Biology Physics. **34**, 931–941 (1996).

[Ev, 1995] P. M. Evans, V. N. Hansen, W. P. M. Mayles, W. Swindell, M. Torr, and J. R. Yarnold, "Design of compensators for breast radiotherapy using electronic portal imaging," Radiotherapy and Oncology. **37**, 43-54 (1995).

[Fi, 1993]   C. Fiorino, A. del Vecchio, G. M. Cattaneo, M. Fusca, B. Longobardi, P. Signorotto, and R. Calandrino, "Exit dose measurements by portal film dosimetry," Radiotherapy and Oncology. **29**, 336-340 (1993).

[Fr, 1998]   B. Fraass, K. Doppke, M. Hunt, G. Kutcher, G. Starkschall, and J. Van Dyke, "American Association of Physicists in Medicine Radiation Therapy Committee Task Group 53: Quality assurance for clinical radiotherapy treatment planning," Medical Physics. **25**, 1773-1836 (1998).

[Gi, 1998]   L. M. Girouard, J. Pouliot, X. Maldague, and A. Zaccarin, "Automatic setup deviation measurements with electronic portal images for pelvic fields," Medical Physics. **21**, 1180-1185 (1998).

[Gr, 2002]   E. E. Grein, R. Lee, and K. Luchka, "An investigation of a new amorphous silicon electronic portal imaging device for transit dosimetry," Medical Physics. **29**, 2262-2268 (2002).

[Gr, 2003]   P. B. Greer and C. C. Popescu, "Dosimetric properties of an amorphous silicon electronic portal imaging device for verification of dynamic intensity modulated radiation therapy," Medical Physics. **30**, 1618-1627 (2003).

[Ha, 1951]   H. F. Hare, S. W. Lippincott, D. Sawyer, J. G. Trump, E. W. Webster, K. A. Wright, W. W. Evans, and R. C. Granke, "Physical and clinical aspects of supervoltage rotational therapy," Radiology. **57**, 157-168 (1951).

[Ha, 1973]   A. G. Haus and J. E. Marks, "Detection and evaluation of localization errors in patient radiation therapy," Investigative Radiology. **8**, 384-391 (1973).

[He, 1994]   M. G. Herman, R. A. Abrams, and R. R. Mayer, "Clinical use of on-line portal imaging for daily patient treatment verification," International Journal of Radiation Oncology Biology Physics. **28**, 1017-1023 (1994).

[He, 1995]   B. J. M. Heijmen, K. L. Pasma, M. Kroonwijk, V. G. Althof, J. C. de Boer, A. G. Visser, and H. Huizenga, "Portal dose measurement in

radiotherapy using an electronic portal imaging device (EPID)," Radiotherapy and Oncology. **49**, 125-132 (1995).

[He, 2001] M. G. Herman, J. M. Balter, D. A. Jaffray, K. P. McGee, P. Munro, S. Shalev, M. Van Herk, and J. W. Wong, "Clinical use of electronic portal imaging: Report of AAPM Radiation Therapy Committee Task Group 58," Medical Physics. **28**, 712-737 (2001).

[In, 1976] International Commission on Radiation Units and Measurements, "Determination of absorbed dose in a patient irradiated by beams of X or gamma rays in radiotherapy procedures," ICRU Rep. **24**, ICRU Publications, Bethesda, Maryland (1976).

[Jo, 1991] S. M. Jones and A. L. Boyer, "Investigation of an FFT-based correlation technique for verification of radiation treatment setup," Medical Physics. **18**, 1116-1125 (1991).

[Le, 1974] P. M. K. Leung, J. van Dyk, and J. Robins, "A method of large irregular field compensation," British Journal of Radiology. **47**, 805-810 (1974).

[Ki, 1993] M. C. Kirby and P. C. Williams, "Measurement possibilities using an electronic portal imaging device," Radiotherapy and Oncology. **29**, 237-243 (1993).

[Ki, 1995] M. C. Kirby and P. C. Williams, "The use of an electronic portal imaging device for exit dosimetry and quality control measurements," International Journal of Radiation Oncology Biology Physics. **31**, 593-603 (1995).

[Ki, 2003] W. Kilby and C. Savage, "The effect of the Varian amorphous silicon electronic portal imaging device on exit skin dose," Physics in Medicine and Biology. **48**, 3117-3128 (2003).

[Kh, 1994] F. M. Khan, *"The Physics of Radiation Therapy,"* 2nd Edition, Williams & Wilkins, Baltimore, MA (1994).

[Kr, 1998] M. Kroonwijk, K. L. Pasma, S. Quint, P. C. M. Koper, A. G. Visser, and B. J. M. Heijmen, "In vivo dosimetry for prostate cancer patients using

an electronic portal imaging device (EPID); detection of internal organ motion," Radiotherapy and Oncology. **49**, 125-132 (1998).

[Ku, 1999]   H. D. Kubo, E. G. Shapiro, and E. J. Seppi, "Potential and role of a prototype amorphous silicon array electronic portal imaging device in breathing synchronized radiotherapy," Medical Physics. **26**, 2410-2414 (1999).

[La, 2001]   K. A. Langmack, "Portal imaging," British Journal of Radiology. **74**, 789-804 (2001).

[Li, 2003]   D. J. Little, L. Dong, L. B. Levy, A. Chandra, and D. A. Kuban, "Use of portal images and BAT ultrasonography to measure setup error and organ motion for prostate IMRT: implications for treatment margins," International Journal of Radiation Oncology Biology Physics. **56**, 1218-1224 (2003).

[Lo, 1996b] D. A. Low, Z. Li, and E. E. Klein, "Verification of milled two-dimensional photon compensating filters using an electronic portal imaging device," Medical Physics. **23**, 929-938 (1998).

[Ma, 1974]   J. E. Marks, A. G. Haus, G. H. Sutton, and H. L. Griem, "Localization error in the radiotherapy of Hodgkin's disease and malignant lymphoma with extended mantle fields," Cancer. **34**, 83-90 (1974).

[Ma, 1976]   J. E. Marks, A. G. Haus, G. H. Sutton, and H. L. Griem, "The value of frequent treatment verification films in reducing localization error in the irradiation of complex fields," Cancer. **37**, 2755-2761 (1976).

[Ma, 1997]   L. Ma, P. B. Geis, and A. L. Boyer, "Quality assurance for dynamic multileaf collimator modulated fields using a fast beam imaging system," Medical Physics. **24**, 1213–1220 (1997).

[Mc, 2000]   B. M. McCurdy and S. Pistorius, "Photon scatter in portal images: physics characteristics of pencil beam kernels generated using the EGS Monte Carlo code," Medical Physics. **27**, 312-320 (2000).

27

[Mc, 2001]   B. M. C. McCurdy, K. Luchka, and S. Pistorius, "Dosimetric properties of an amorphous silicon electronic portal imaging device," Medical Physics. **28**, 911-924 (2001).

[Mc, 2004]   L. N. McDermott, R. J. W. Louwe, J.-J. Sonke, M. B. van Herk, and B. J. Mijnheer, "Dose-response and ghosting effects of an amorphous silicon electronic portal imaging device," Medical Physics. **31**, 285-295 (2004).

[Me, 1985]   H. Meertens, M. van Herk, and J. Weeda, "A liquid ionization detector for digital radiography of therapeutic megavoltage photon beams," Physics in Medicine and Biology. **30**, 313-321 (1985).

[Me, 1990]   H. Meertens, M. van Herk, J. Bijhold, and H. Bartelink, "First clinical experience with a newly developed electronic portal imaging device," International Journal of Radiation Oncology Biology Physics. **18**, 1173-1181 (1990).

[Me, 1997]   E. Melian, G. S. Mageras, Z. Fuks, S. A. Leibel, A. Niehaus, H. Lorant, M. Zelefsky, B. Baldwin, and G. J. Kutcher, "Variation in prostate position quantification and implications for three-dimensional conformal treatment planning," International Journal of Radiation Oncology Biology Physics. **38**, 73–81 (1997).

[Me, 2003]   G. V. Menon and R. S. Sloboda, "Compensator quality control with an amorphous silicon EPID," Medical Physics. **30**, 1816-1824 (2003).

[Mu, 1990a] P. Munro, J. A. Rawlinson, and A. Fenster, "A digital fluoroscopic imaging decice for radiotherapy localization," International Journal of Radiation Oncology Biology Physics. **18**, 641-649 (1990).

[Mu, 1995]   P. Munro, ''Portal imaging technology: Past, present, and future,'' Seminars in Radiation Oncology. **5**, 115–133 (1995).

[Mu, 1998]   P. Munro, "X-ray quantum limited portal imaging using a-Se flat panel arrays," Medical Physics. **5**, 689-702 (1998).

[Mu, 1999]   P. Munro, *Megavoltage Radiography for Treatment Verification,*" in *"Modern Technology of Radiation Oncology: A Compendium for*

28

Medical Physicists and Radiation Oncologists," Chapter **13**, 481-508. ed: J. Van Dyk. Madison, WI: Medical Physics Publishing (1999).

[Ne, 1942]   J. Neilsen and S. H. Jensen, "Some experimental and clinical lights on rotation therapy, its basis and possibilities," Acta Radiologica. **23**, 51-66 (1942).

[Ne, 2001]   A. J. Nederveen, J. J. W. Lagendijk, and P. Hofman, "Feasibility of automatic marker detection with an a-Si flat-panel imager," Physics in Medicine and Biology. **46**, 1219-30 (2001).

[Pa, 1998b]   K. L. Pasma, M. Kroonwijk, J. C. J. de Boer, A. G. Visser, and B. J. M. Heijmen, "Accurate portal dose measurement with a fluoroscopic electronic portal imaging device (EPID) for open and wedged beams and for dynamic multileaf collimation," Physics in Medicine and Biology. **43**, 2047–2060 (1998).

[Pa, 1999]   K. L. Pasma, M. Kroonwijk, E. B. van Dieren, A. G. Visser, and B. J. M. Heijmen, "Verification of compensator thicknesses using a fluoroscopic electronic portal imaging device," Medical Physics. **26**, 1524-1529 (1999).

[Pe, 1960]   C. R. Perryman, J. D. McAllister, and J. A. Burwell, " Cobalt 60 radiography," American Journal of Roentgenology. **83**, 525-532 (1960).

[Ra, 1985]   I. Rabinowitz, J. Broomberg, M. Goitein, K. McCarthy, and J. Leong, "Accuracy of radiation field alignment in clinical practice," International Journal of Radiation Oncology Biology Physics. **11**, 1857-1867 (1985).

[Ro, 1995]   D. M. Roback and B. J. Gerbi, "Evaluation of electronic portal imaging device for missing tissue compensator design and verification," Medical Physics. **22**, 2029-2034 (1995).

[Sp, 1962]   E. B. Springer, L. Pape, F. Elsner, and M. L. Jacobs, "High-energy radiography (Cobalt 60 and Cesium 137) for tumor localization and treatment planning," Radiology. **78**, 260-262 (1962).

[Sp, 2000]   L. Spies, P. M. Evans, M. Partridge, V. N. Hansen, and T. Bortfeld, "Direct measurement and analytical modeling of scatter in portal imaging", Medical Physics. **27**, 462-471 (2000).

[St, 1958]   M. Strandquist and B. Rosengren, "Television-controlled pendulum therapy," British Journal of Radiology. **31**, 513-514 (1958).

[St, 1998]   M. Strotzer, J. Gmeinwieser, M. Volk, R. Frund, J. Seitz, C. Manke, H. Albrich, and S. Feuerbach, "Clinical application of a flat panel x-ray detector based on amorphous silicon technology," American Journal of Radiology. **171**, 23-27 (1998).

[St, 2000]   J. C. Stroom, M. Kroonwijk, K. L. Pasma, P. C. Koper, E. B. van Dieren, and B. J. Heijmen, "Detection of internal organ movement in prostate cancer patients using portal images," Medical Physics. **27**, 452-461 (2000).

[Sw, 1966]   R. W. Swain and R. J. Steckel, "Beam localization in cobalt and megavoltage therapy during treatment," Radiology. **86**, 529 (1966).

[Sw, 1996]   W. Swindell and P. M. Evans, "Scattered radiation in portal images: a Monte Carlo simulation and a simple physical model," Medical Physics. **23**, 63-73 (1996).

[Va, 1988]   M. van Herk and H. Meertens, " A matrix ionization chamber imaging device for on-line patient setup verification during radiotherapy," Radiotherapy and Oncology. **11**, 369-378 (1988).

[Va, 1993]   M. van Herk, K. Gilhuijs, P. Williams, P. Cinquin, L. Cionini, and W. Swindell, "Role of electronic portal imaging in high dose/high precision radiotherapy," Radiotherapy and Oncology. **29**, 269-270 (1993).

[Ve, 1982]   L. J. Verhey, M. Goitein, P. McNulty, J. E. Munzenriter, and H. D. Suit, "Precise positioning of patients for radiation therapy," International Journal of radiation Oncology Biology Physics. **8**, 289-294 (1982).

[Ve, 2000]   S. Vendantham, A. Karellas, and S. Suryananayanan, "Mammographic imaging with a small format CCD-based digital cassette: physical

characteristics of a clinical system," Medical Physics. **27**, 1832-1840 (2000).

[Vi, 1997]   E. Vigneault, J. Pouliot, J. Laverdière, J. Roy, and M. Dorion, "Electronic portal imaging device detection of radioopaque markers for the evaluation of prostate position during megavoltage irradiation: a clinical study," International Journal of radiation Oncology Biology Physics. **37**, 205-212 (1997).

[Wa, 1958]   H. Wallman and N. Stalberg, "A television-roentgen system for pendulum therapy," British Journal of Radiology. **31**, 576-577 (1958).

[Wa, 1996]   H. Wang, T. Falco, and B. G. Fallone, "A metal screen-amorphous selenium based image receptor in megavoltage portal imaging," Medical Physics. **21**, 237-244 (1994).

[Wa, 2003]   B. Warkentin, S. Steciw, S. Rathee, and B. G. Fallone, "Dosimetric IMRT verification with a flat-panel EPID," Medical Physics. **30**, 3143-3155 (2003).

[We, 1997]   S. Webb, *The physics of conformal radiotherapy*," IOP Publishing Ltd, London (1997).

[Wi, 2000]   J. R. Williams and D. I. Thwaites, *Radiotherapy physics in practice*," 2nd Edition, Oxford University Press, Oxford (2000).

[Wo, 1990]   J. W. Wong, W. R. Binns, A. Y. Cheng, L. Y. Gear, J. W. Epstein, J. Klarmann, and J. A. Purdy, "On-line radiotherapy imaging with an array of fiber-optic image inducers," International Journal of radiation Oncology Biology Physics. **18**, 1477-1484 (1990).

[Wu, 2001]   J. Wu, T. Haycocks, H. Alasti, G. Ottewell, N. Middlemiss, M. Abdolell, P. Warde, A. Toi, and C. Catton, "Positioning errors and prostate motion during conformal prostate radiotherapy using on-line isocentre set-up verification and implanted prostate markers," Radiotherapy and Oncology. **61**, 127-133 (2001).

[Yi, 1994]   F-F Yin, M. C. Schell, and P. Rubin, "A technique of automating compensator design for lung inhomogeneity correction using an

electronic portal imaging device," Medical Physics. **21**, 1729-1732 (1994).

CHAPTER 2: PORTALVISION aS500 EPID: DESCRIPTION AND OPERATION

2.1 INTRODUCTION

The application of amorphous silicon flat panel imaging technology in the construction of EPIDs is fairly recent and research is still in progress to describe many of the operational features of these detectors. Though EPIDs are primarily intended to verify radiotherapy setup geometry, there has been growing interest in extending their application to verification of delivered dose, verification of photon beam flatness/symmetry, and compensator design and quality assurance. Of considerable current interest is their potential to replace film for verification of intensity modulated radiation therapy (IMRT) protocols. For dosimetry applications, it is important to identify operating parameters that best suit this purpose. This chapter details extensively the work done to determine appropriate operating parameters for the aS500 EPID, especially for dosimetric applications. This chapter is organized in four major sections: description of the aS500 EPID, acceptance testing, operating parameter determination, and verification of operation for dosimetry.

2.2 DESCRIPTION OF THE aS500 EPID

The Varian aS500 EPID that entered the commercial market in November 1999 is an active matrix flat panel imager [Po, 2000a] that employs amorphous silicon thin film transistor (a-Si TFT) and photodiode arrays. The Varian aS500 EPID used for the preliminary investigation cited in this chapter was installed at the Cross Cancer Institute on 13th February, 2001 (Product code serial # 803860, PortalVision, Varian Medical systems, Palo Alto, CA). It was attached to a Varian 23EX linac (Varian Medical systems, Palo Alto, CA) for an initial period of 11 months and then moved onto a Varian 2300CD linac to which it is currently attached. The EPID is deployed from the linac on a motorized robotic retractable arm that can move the detector in the

33

lateral (X), longitudinal (Y), and vertical (Z) directions (Fig. 2.1), with the origin of the coordinate system being at the linac isocenter[†]. The EPID has a sensitive viewing area of 40 x 30 cm^2 with a pixel pitch of 0.784 mm and a dynamic range of 14 bits.

2.2.1 Parts of the EPID

The Image Detection Unit (IDU) of the aS500 EPID is in the form of a stack having layers that perform various functions in the megavoltage imaging process and incorporates associated electronics (Fig. 2.2(a)). The four distinct parts are discussed in this section (Fig. 2.2) [Po, 2000a].

(a) **Copper plate:** A 1 mm copper (Cu) buildup plate, intended to absorb x-ray photons and emit recoil electrons, forms the first layer in the detector stack. It also serves to partially shield the downstream scintillation screen from any scattered radiation and thus enhances the efficiency of detection of primary incident x-rays.

(b) **Phosphor screen:** A Kodak Lanex Fast B scintillating phosphor screen $(Gd_2O_2S:Tb)$, of thickness 133 mg/cm^2, absorbs the recoil electrons and transforms them to visible light.

(c) **a-Si array:** A 512 x 384 pixel matrix deposited on a glass substrate constitutes the sensitive image-forming layer. Each pixel having a pitch of 0.784 mm consists of an a-Si n-i-p photodiode to integrate the incoming light in charge captures, and a TFT that acts as a three-terminal switch for readout. The fill factor of the pixel is ~83%.

(d) **System electronics:** The electronics associated with the system drive the TFT switches and read out the charge captures (details in Section 2.2.2.1).

The hand controller that accompanies the EPID can automatically position it at programmed source-to-detector distances of 120, 140, 150, 160, and 180 cm. All other vertical positions, along with any lateral and longitudinal motion, have to be manually entered on the hand controller. During acceptance, we measured the position of the

---

[†]In Chapters 4 and 5, the coordinate system origin is specified with respect to the linac focal spot.

imaging plane (photodiode sensitive layer) to be 1.3 cm below the top of the detector stack (Fig. 2.2(b)). The position displayed on the hand controller, which is the distance from the x-ray source to the top of the stack, will henceforth be referred to as the source-to-EPID distance (SED), and the actual source to sensitive layer distance as the source-to-detector distance (SDD). When using an ion chamber for comparative measurements, SDD will represent the distance from the x-ray source to the center of the active volume of the chamber. A summary of the detector specifications is given in Table 2.1.

2.2.2 Image Acquisition

The treatment acquisition task is the principal function of the portal imager. Subcategories included under it are the following: (a) Acquisition workspace, providing capabilities for image acquisition; (b) Review workspace, to review and approve the portal images; (c) Calibration workspace, for the manual or automatic calibration of all the acquisition modes; and (d) Maintenance workspace, for tuning and maintaining the portal vision image acquisition system.

2.2.2.1 Acquisition process

The aS500 EPID operation is synchronized using sync pulses from the linac (Fig. 2.3). The sync signal (SYNC) from the linac runs at a standard frequency that is characteristic of the photon energy mode (6 or 15 MV) selected. Typically in Varian linacs, a train of 6 consecutive sync pulses, appropriately masked, forms a pulse pattern. The actual number of radiation beam pulses output by the linac depends on the pulse repetition rate mask selected for linac operation, i.e. the beam acquisition trigger (ACQ TRIG). The acquisition trigger signal is used directly to trigger the EPID sync generator (PVSYNC), as shown in Fig. 2.3. Between PV sync pulses the EPID reads the accumulated charge from a limited number of rows. Because the readout rate is fixed, the number of rows read between pulses is dependant on PVSYNC. The readout process in any one pixel occurs as follows. Initially a bias voltage of –5V is applied to

the photodiode before exposure. On exposure, charge accumulation occurs in the photodiode capacitance in a ratio proportional to the exposure (Fig. 2.4(a)). After exposure (Fig. 2.4(b)), the gate lines are activated and all TFTs in that row become transparent (Fig. 2.4(c)). Charge is transferred through the drain of the TFT to the data line and then captured by external charge sensitive preamplifiers in the read-out electronics shown in Fig. 2.5. After readout, the pixel is reset to drain off any residual charge before the next SYNC pulse arrives (Fig. 2.4(d)). This reset process is included in the readout cycle. Rows are read out successively by switching on the next row as soon as the current one has been read. The sequence continues until all the lines are read, resulting in one complete image frame. The time between consecutive readouts of the same pixel row is referred to as the frame time [Po, 2000a].

2.2.2.2 Scanning and acquisition modes

The aS500 EPID has two readout scanning modes - high and standard - that can be selected depending on the desired image quality. The modes are specified by the number of frames averaged – for high quality images, more frames are averaged. By default, the high scanning mode on our EPID averages ten frames and the standard mode, two. An optional third scanning mode for IMRT is currently available for imaging throughout the course of a treatment delivery. Image quality is also dependent on the output stability of the machine. User selectable acquisition modes specify photon beam energy, linac pulse repetition rate, and EPID scanning mode, e.g. [6 MV, 300 MU/min, standard scan].

2.2.2.3 Pixel defect identification

In the detector array (~200,000 pixels), there can be several non-functioning pixels that will show up in an unprocessed image as "dead" pixels. A pixel correction procedure is performed to compensate for any defective pixels in the array. Interpolation of data from the four nearest neighboring pixels is done to fill in the missing information [Po, 2000a]. Defective pixels are recognized using a PixCorr

36

program distributed with the PV aS500 EPID software. An IDU drift image (see Section 2.3.2.1.2) is used to identify the defective pixels, and is obtained as follows. First a dark field image is taken. Then the acquisition process is stopped for a period of time to allow the leakage current to be integrated, and a second image is taken. The IDU drift image is obtained by subtracting the first image from the second, and will display the leakage in each pixel and therefore, the defective pixels. The IDU drift image is loaded in the background of the image display and the pixel defects are manually identified. These are added to a pixel defect map that is displayed in the foreground. Figure 2.6 shows the pixel defect map, with 880 defective pixels, created when our aS500 EPID was moved to the Varian 2300CD linac. The defect map is stored on the local hard disk of the PortalVision workstation. When a clinical image is taken, the pixel defect map is loaded and interpolated values for the defective pixels calculated.

2.2.2.4 Linac dose rate servo (DRS) control

Medical linear accelerators have an integral dose rate servo (DRS) unit whose function is to maintain a steady beam output. For Varian dual energy linacs, a pulse length servo (PLS) accomplishes this by adjusting the length of the beam pulse. To avoid variations in portal image intensity within an image frame arising from intentional pulse-to-pulse adjustments of beam fluence, the PLS is switched off during image acquisition. A start delay can be introduced prior to image acquisition to obtain a stable beam, and is applied only to the first image in a series of acquisitions (Fig. 2.7(a)) [Po, 2000a]. For subsequent images, a DRS stabilization time needs to be incorporated whereby a delay is introduced after the DRS has been switched from non-regulating to regulating mode (Fig. 2.7(b)). The DRS minimal switch time is the minimum time interval between acquisitions required for the PLS to switch from the non-regulating to regulating state and back again. In the special case of lengthy acquisitions such as flood field images (see Section 2.2.3) and IMRT, where a large number of frames are averaged, the PLS is kept "on" during image acquisition.

37

2.2.2.5 Acquisition sequences

An image acquisition procedure is prescribed using image sequence templates. The following notation, a-b-c, is used to describe a sequence, where the letters represent images acquired at the start, middle and end of the treatment session respectively. Images may also be acquired before or after the treatment session. The most commonly chosen sequences for acquisition are the single image during treatment (1-0-0), cine loop image acquisition (continuous imaging during the entire treatment session), three images during treatment (1-1-1), double exposure before treatment, and double exposure after treatment.

An example of a [15 MV, 100 MU/min, standard scan] acquisition is shown in Figure 2.8(a). As discussed before, due to the fixed readout rate of the electronics only a limited number of rows can be read out after each beam pulse, the maximum number being at the lowest repetition rate of 100 MU/min. Hence to read all the rows (1 frame) using this acquisition mode, three beam pulses are required. These individual pulses can be seen to form the three bands in the image shown in Fig. 2.8(b).

2.2.2.6 Image storage

PortalVision images contain a range of pixel values from about -100 (white, lower dose) to -4000 (black, higher dose). Following convention, pixel values will be reported as positive values in this work. Images are stored in the file system (Vision database) of the Vision image server as image files. Each file has a 512 byte header containing administrative details followed by the pixel data itself. A PortalVision workstation displays gray level images to the operator, but stored pixel values are the original raw values.

2.2.2.7 The Image Acquisition System 2 (IAS2) database

The operating parameters for image acquisition may be altered in the Image Acquisition System 2 (IAS 2) database by employing the Service Monitor software

38

[Po, 2000a]. This system contains the control and acquisition electronics for the image detection unit (Fig. 2.5). Parameters that can be changed in the database are organized under the following six categories: scanning modes, treatment acquisition modes, calibration sets, energy lookup, no radiation acquisition modes, and the radiation therapy imaging system (RTIS) configuration (see Appendix 2.1: Table A1(a)-(e)). There are several subcategories associated with each category whose parameters may be adjusted to improve image quality.

2.2.3 Calibration of the EPID

EPID calibration is designed to remove background noise and provide a spatially uniform response for clinical imaging. The EPID signal can change with time due to changes in the performance of the detector electronics and also because of changes in beam characteristics. If routine calibration is not performed, images taken with the EPID after a certain length of time will be corrected with an out of date original calibration curve that might not account for ensuing changes in EPID and linac performance. For clinical imaging, where only a verification portal image is of interest, any slight change in the pixel sensitivities can be ignored provided that the images have good clarity. On the other hand, for dosimetry, extraction of the portal dose image from the EPID image depends on an additional dosimetric calibration of the EPID that relates pixel value to dose. If routine calibration is not done, the portal dose image after a certain period will not correspond to the measured pixel value. Hence for best quality verification images in clinical portal imaging and for accurate pixel value to dose conversion in EPID dosimetry it is necessary to perform the EPID cassette calibration routinely, preferably before QA.

As the response of the EPID is dependent on the photon energy and the repetition rate of the radiation beam, calibration is performed separately for each acquisition mode. Calibration involves acquiring a dark field image and a flood field image for each acquisition mode.

A dark field image provides information about background noise and is obtained by taking a base reading for each pixel in the absence of radiation. Any array imperfections or electrometer offsets may be spotted on the dark field image. A large number of frames are averaged to reduce statistical fluctuations; sixty frames for the aS500 dark field calibration procedure. The resultant image displays vertical lines and bands arising from photodiode leakage currents and varying electrometer offsets, respectively (Fig. 2.9(a)).

A flood field image is obtained by irradiating the entire sensitive area of the detector with an open field and is used to correct for variations in individual pixel sensitivities and radiation field inhomogeneity (Fig. 2.9(b)). Thirty frames are acquired and averaged to reduce statistical fluctuations. Unlike a clinical image, a flood field image is taken with the DRS enabled because the extended imaging time needed to collect thirty frames serves to average out any horizontal bands that might appear because of intentional dose rate adjustments.

Dark and flood field calibration images are obtained at an SED of 140 cm with the gantry positioned at an angle of 0° [In, 1996] and the collimator set at 28.6 x 21.4 cm^2 for all acquisition modes. Calibration images for each acquisition mode are stored in the IAS2 database and used to correct for stationary non-uniformities in detector response and dark current in clinical object images. The correction is performed for each pixel in an object image according to

$$CI = \left[\frac{OI - DF}{FF - DF} \right] \times k_{\overline{FF}}, \tag{2.1}$$

where CI and OI are the corrected and uncorrected object images and DF and FF are the dark and flood field images. $k_{\overline{FF}}$, a scaling factor, is the mean of the flood field image pixel values. Test images can be taken during calibration to assess the quality of the correction (Fig. 2.9(c)). Once Eq. 2.1 has been applied to an uncorrected object image, pixel values in the central portions of open fields should be fairly uniform. Calibration of all of the available acquisition modes was performed during EPID

40

acceptance testing (see Section 2.3), and has continued on a monthly basis for the acquisition modes used clinically and for research.

2.3 ACCEPTANCE TESTS

Acceptance tests are performed with a view to providing a baseline for comparison of data during subsequent quality assurance tests. The former include one-time as well as ongoing measurements made repeatedly to verify acceptable performance of a device. There are a variety of EPIDs available in the market today, so that it is not possible to define generic guidelines for acceptance. EPID manufacturers each have their own individual acceptance standards and specifications. This section describes the acceptance procedures conducted for our Varian aS500 EPID installed on a Varian 23EX dual energy linac. The procedures are outlined in detail in the PortalVision Customer Acceptance Procedure (CAP) Reference Manual [Po, 2000b] and data was recorded in accordance with the System Verification Summary (SVS) reference manual [Po, 2000c].

The acceptance tests are broadly classified in two categories: verification of the support arm and verification of the acquisition system. Figure 2.1 illustrates the coordinate conventions, adapted from IEC 1217, used in this work to describe the various motions of the EPID [In, 1996].

2.3.1 Verification of Mechanical Motion of Retractable Arm

2.3.1.1 Position

The detector is held by a retractable support arm (R-arm) that can be swung out during imaging to bring the EPID in line with the treatment head (Fig. 2.1). The true vertical or Z-axis position of the R-arm (actually, the position of the top of the detector stack, see Fig. 2.2(a)) with reference to the linac isocenter, as stipulated by the manufacturer, should be within ±0.3 cm of the position displayed on the EPID hand controller. The actual position with respect to the isocenter was measured using a

41

mechanical front pointer and a ruler. The arm position check was performed at a SED of Z = 120 cm and {X,Y = 0,0 cm} in the lateral and longitudinal directions, respectively. The difference between the displayed and measured positions was found to be 0.05 cm (< tolerance of 0.3 cm).

2.3.1.2 Travel range

The three dimensional position of the EPID is characterized by vertical (Z-axis), longitudinal (Y-axis) and lateral (X-axis) coordinates reported with respect to isocenter as: vrt/lng/lat. The hand controller displays these distances. The travel range of the R-arm supporting the detector is measured in the longitudinal and lateral directions.

2.3.2 Verification of the Image Acquisition System

The quality of EPID images depends both on the output stability of the linac and on the functioning of the detector itself. Consequently, acceptance tests address minimum standards for clinical image formation on both fronts.

2.3.2.1 Tests without radiation

2.3.2.1.1 IDU test image

An IDU test image is obtained by recording the pixel background leakage with no correction performed for defective pixels. Test images taken with the original IDU installed at our center showed a banding around the edges (Fig. 2.10(a)). Figure 2.10(b) shows a test image taken subsequently with a replacement IDU.

2.3.2.1.2 IDU drift image

An IDU drift image is taken to detect the presence of background signal drift in the IDU. A banding along the edge, similar to that for the IDU test image, was seen

42

with the original IDU (Fig. 2.10(c)), which was rectified with the replacement (Fig. 2.10(d)).

2.3.2.1.3 Saw tooth image

An analog signal generator in the acquisition central processing unit (ACPU) produces a saw tooth image that is routed to the analog to digital converter on board the IDU. For a properly functioning converter, the image will exhibit saw tooth modulation as shown in Fig. 2.10(e) for our EPID.

2.3.2.1.4 IDU noise image

IDU noise images verify the system's ability to produce images having consistent background noise properties for consecutive acquisitions. A uniform noise image is hence expected when subtracting two successive images, as seen in Fig. 2.10(f).

2.3.2.2 Tests with radiation

2.3.2.2.1 Dose rate servo (DRS) stability

The DRS stability test was performed on 28.6 x 21.4 cm^2 open field images acquired using [6/15 MV, 300 MU/min, standard scan] acquisition modes. Using a Matlab (MATLAB 5.3, The Mathworks Inc, Nattick, MA) routine, average pixel values from 20 x 20 pixel regions of interest (ROIs) centered on the darkest and brightest regions of the image were determined and the following relation was employed to determine η, the DRS stability [Po, 2000a],

$$\eta = \left(\frac{P_d}{P_b} - 1\right) \times 100, \tag{2.2}$$

where P_d and P_b are the average pixel values in the darkest and brightest ROIs, respectively. It was observed that the DRS stability remained within the manufacturer's

specified value of 3% for images acquired with both high ($\eta = 2.1\%$) and low ($\eta = 0.8\%$) energy photon beams.

2.3.2.2.2 Automatic beam off

The PV system can be programmed to automatically switch off the beam after image acquisition. This functionality was verified by taking a clinical image and specifying "Beam Off" in the image sequence protocol for a test patient. It was observed that the function was readily activated and the beam was automatically switched off after acquisition.

2.3.2.2.3 Spatial resolution

The spatial resolution during acceptance was tested by verifying the visibility of a 1 mm diameter stainless steel wire in an image taken with the EPID positioned at 130 cm using [6/15 MV, 300 MU/min, standard scan] acquisition modes. Both images revealed the wire with adequate detail (Fig. 2.11).

2.3.2.2.4 Contrast resolution

Contrast resolution is a measure of how well an object can be differentiated from its background. It can be defined as the percent difference between the intensity of an object (I_0) and its background (I_B) in an image (Fig. 2.12(a)).

$$C = \left(\frac{I_O}{I_B} - 1 \right) \times 100\% \qquad (2.3)$$

Noise in the imaging system degrades contrast resolution. The contrast resolution of our aS500 EPID images was studied using a contrast-detail phantom (PortalVision, or PV phantom) supplied by the manufacturer [Po, 2000a]. It enables qualitative assessment of the minimum contrast that can be observed for various detail sizes. The 140.00 x 140.00 x 21.75 mm^3 aluminum PV phantom has holes of depths 0.25, 0.50,

44

1.0, 2.0, and 3.0 mm arranged in five rows. The holes in each row have diameters of 1, 2, 4, 7, 10, and 15 mm, respectively. According to Thomason, "Contrast detail phantoms are used to assess the smallest resolvable object with minimum contrast and are scored by recording the number of holes seen at each depth or contrast level" [Th, 1998]. The phantom was placed at the isocenter with the holes facing the EPID for imaging. The window and level on the image display were adjusted to bring into view the maximum number of holes for each acquisition mode (Fig. 2.12(b)). Images were acquired for the two acquisition modes of [6/15 MV, 300 MU/min, standard scan]. The object contrast resolution of the resulting images can be determined using Table 2.2 [Po, 2000a]. However, the conventional method of presenting results is to report the number of holes observed by visual evaluation. During acceptance, 22 holes were observed with the lower energy (Fig. 2.12(c)) and 18 holes with the higher energy (Fig. 2.12(d)).

2.4   OPERATING PARAMETERS FOR IMAGING

EPID operating parameters are maintained in the IAS2 Service Monitor of the Vision system. They can be categorized into two groups: fixed (those that have been fixed by the manufacturer), and default (those that have assigned values but can be changed by the user). The most important ones are given in Tables A1(a)-(e) in Appendix 2.1, which also indicate the functions of the parameters. Appendix 2.2 defines some of the terminology associated with aS500 EPID operation and provides values for fixed parameters.

2.4.1   Parameters Investigated for Better Imaging Performance

This section describes the investigation of some of the operating parameters to determine the most suitable settings for imaging. These parameters had a default value at the time of acceptance testing that was varied systematically in an effort to obtain improved image quality. A 1-0-0 imaging sequence and [6 MV, 300 MU/min, standard scan] acquisition mode was used for imaging except where otherwise indicated. The

baseline acquisition process employed a 1 ms start delay, no sync delay and 2 frame averages per image (see Appendix 2.1). The EPID was positioned at an SED of 140 cm with a collimator setting of 28.6 x 21.4 cm^2. Central axis measurements were obtained by averaging values in a 20 x 20 pixel (~1.5 cm^2) region of interest whose center lay along the central axis of the beam (ROI_{CAX}). The baseline parameters were held constant unless otherwise specified for subsequent measurements.

2.4.1.1 Number of resets

Resetting of the electronics is performed to zero any residual charge in the pixels that would otherwise contribute to the subsequent image frame. We investigated the number of resets required for pixel value consistency in consecutive images by taking four images in quick succession for increasing numbers of resets. For each set of images, the difference in the average pixel value from the ROI_{CAX} for the first and fourth image was determined. It was observed that the differences remained quite constant with resets ranging from 5 to 10 (Fig. 2.13). The default value of 5 resets was hence accepted for our measurements.

2.4.1.2 Sync delay

Sync delay is the wait time after the radiation beam pulse has ended and before row scanning starts (Fig. 2.14(a)). To study its effect in aS500 imaging, we took images with a range of sync delays from 0 to 1000 μs (Fig. 2.14(b)). The images show a horizontal line at the starting row after each beam pulse is delivered, that becomes more apparent with increasing sync delay. A Fourier analysis of these images was performed to determine the power spectrum (product of the Fourier transform and its complex conjugate), as it is a better representation of such variations. Figure 2.15 shows the maximum value of the power spectrum for the sum of all columns in each image. The data suggests that the 0 ms sync delay is associated with the weakest line artifact, and hence it was selected for our imaging purposes.

46

2.4.1.3 Frame averages

Frame averaging is performed to improve image quality by decreasing statistical noise. To determine the effect of frame averaging, images were taken with increasing numbers of frame averages ranging from 1 to 50, and the mean value from a 20 x 20 pixel ROI_{CAX} was determined. For both 6 and 15 MV beam energies, the variation in mean pixel value with increasing number of frame averages showed only a small change (< 4%) up to 25 frame averages, beyond which the pixel values increased (Fig. 2.16), particularly for the 15 MV beam. This could be due to any of the following reasons: (i) the presence of residual charge because of insufficient resets, (ii) drift in linac output arising from the switching off of the DRS system, or (iii) image lag effect [El, 1999]. The values for the 6 MV beam are shown in Table 2.3. The noise in the ROI is calculated by the Vision software as the ratio of the standard deviation in the pixel values to their mean value. The noise showed a steady decrease with increase in number of frame averages (Fig. 2.17). A compromise is hence needed in choosing the number of frame averages, considering both the pixel value and the noise behavior. Figure 2.17 shows that the noise level for 1 frame average is < 0.5% of the average pixel value and therefore nearly negligible. Our experiments were hence conducted with the default clinical setting of 2 frame averages (standard mode).

2.4.1.4 Start delay

The start delay or beam stabilization time is the time in milliseconds between beam on and the start of image acquisition. This time may be increased to allow the beam to stabilize, as EPID images are taken with the dose rate servo switched off. Start delay can only be applied to the first frame of an imaging sequence, i.e. a start delay is not possible for a 0-1-0 type acquisition. The effect of introducing a delay before acquisition on image quality was determined by taking images for a range of start delays from 0 to 500 ms for the [6 MV, 100 MU/min, standard scan] acquisition mode. The time was incremented in steps of 2 ms up to 20 ms, 10 ms up to 100 ms and thereafter in 100 ms steps up to 500 ms. To enable clearer visibility of start delay

47

effects, we acquired only a single image frame. The DRS stability test performed on these images (see Sec. 2.3.2.2.1) showed that there was a small improvement for delays beyond 10 ms (Fig. 2.18), which we infer is the delay needed for the beam to stabilize. For our dosimetric work with this EPID, a start delay was not necessary as the images were acquired using the 0-50%-0 (image taken at the mid point of treatment delivery) acquisition mode.

2.4.1.5 Effect of dark current

Temporal variations in the imaging detector dark current can cause drift in the dark field images used in image calibration (see Sec. 2.2.3). To determine if such variations are of concern the number of frame averages was set to 1 (default = 60) to accentuate any deviation in the dark fields for the [6 MV, 100 MU/min, standard scan] acquisition mode and a series of dark field images were taken at 5-second intervals. Table 2.4 displays the mean pixel value for the ROI_{CAX} (Fig. 2.19) and the noise therein, respectively. The values in the table show that there is no systematic trend in the dark current over a one-minute time span. The mean pixel value from all dark field images was 22.1 ± 0.8. Since this value is only ~1% of a typical image (having values of ~2300 for one frame average), we concluded that the dark current contribution was small, and that short-term dark current fluctuations are negligible.

2.5 VERIFICATION OF SYSTEM OPERATION FOR DOSIMETRY

This section provides details of measurements made to validate several aspects of EPID performance relevant to dosimetry. All measurements were performed with the [6/15 MV, 300 MU/min, standard scan] acquisition mode at an SED of 140 cm unless otherwise indicated.

48

2.5.1 Pixel Pitch

In order to calculate the physical size of an object appearing in an EPID image, we need to know the detector pixel pitch. The manufacturer quotes a pixel pitch of 0.784 cm for the aS500 EPID. This was verified using the EPID imaging geometry in Fig. 2.20 by taking an image of a thin brass slab of length 110.82 ± 0.02 mm and thickness 4.10 ± 0.02 mm (measured using a digital caliper) located on the treatment couch at isocenter (100.0 ± 0.1 cm from the x-ray source). The pixel pitch was then determined as

$$P_p = (L/L_P) \times M, \tag{2.4}$$

where L is the physical length of the slab in mm, L_P is its length in the image in units of pixels, and M is the image magnification factor. With the EPID at an SED of 140 cm, $M = 1.413$. L_P was determined using a Matlab routine that calculated the maximum and minimum pixel values near each end of the slab by averaging over five pixels in the regions just before and after the edge. The mean of the maximum and minimum values was used to locate the position of each edge (Fig. 2.21). Equation 2.4 can hence be rewritten as

$$P_p = L \times \left(\frac{SDD}{SAD}\right) \times \frac{1}{\left(E_R - E_L\right)} \tag{2.5}$$

where L = measured length of brass slab = 110.82 ± 0.02 mm

SDD = Source to detector distance = 141.3 ± 0.1 cm

SAD = Source to axis distance = 100.0 ± 0.1 cm

E_R = Pixel position of the right edge of the slab

E_L = Pixel position of the left edge of the slab

Eq. 2.5 yielded a pixel pitch of 0.783 ± 0.001 mm, which was within experimental error of the manufacturer's stated value of 0.784 mm. It is interesting to note that this level of agreement was only obtained after properly accounting for the offset of the a-Si sensitive layer from the EPID position reported by the hand controller (see Sec. 2.2.1).

2.5.2 Calculation of MU/Image Frame

For a particular beam energy and repetition rate, the number of beam monitor units (MU) delivered per EPID image frame can be estimated as

$$MU_{fr} = M\dot{U} \times t_{fr} \qquad\qquad (2.6)$$

where $M\dot{U}$ is the linac output in MU/s and t_{fr} is the frame time given as

$$t_{fr} = \frac{R_{tot}}{PVSYNC \times R_{PVSYNC}}, \qquad\qquad (2.7)$$

where R_{tot} is the total number of rows (384) and R_{PVSYNC} is the number of rows scanned per PVSYNC pulse [Po, 2000a]. The number of MUs needed to create a single frame image for 6 and 15 MV beams using the aS500 EPID is shown in Fig. 2.22 [Po, 2001].

2.5.3 Additional Buildup for Dose Measurement

The 1-mm thick copper plate in the aS500 EPID used to create recoil electrons is radiologically equivalent to about 1 cm of solid water (Gammex RMI, Middleton, WI) [Mc, 2001], which is not enough to place the sensitive layer at the depth of dose maximum. When the EPID is used for dosimetry, it is desirable to have the sensitive layer at the depth of maximum dose where there is electronic equilibrium. To determine this depth, an experiment was undertaken in which thin slabs of solid water (ranging from 0.1 to 1 cm thick) were successively placed on top of the detector cover, and open field images obtained using the [6/15 MV, 300 MU/min, standard scan] acquisition mode. Pixel values from the ROI_{CAX} (averaged from 3 images) were compared to determine the maximum response depth and therefore the depth of dose maximum. Fig. 2.23 shows that the maximum response for 6 and 15 MV energies occurs with extra buildup thicknesses of 0.5 and 2.1 cm respectively. An additional solid water buildup of 0.5 cm for 6 MV and 2 cm for 15 MV was therefore selected for all of our subsequent dose measurements.

50

2.5.4 Dose Response and Dose Rate Response

The response of an a-Si EPID is linear with energy fluence for open fields, as compared with the square root response of a SLIC EPID [An, 1997]. It is desirable that the EPID signal has no dependence on dose rate in order to minimize the corrections required for interpretation of the data [Ku, 1999].

2.5.4.1 Dose response

Dose response measurements were performed for open fields for a reference field size of 20 x 20 cm^2 at the detector at increasing SEDs of 105 to 160 cm in order, to vary the dose incident on the detector. The images were acquired with the [6/15 MV, 300 MU/min, standard scan] acquisition modes and a 0-1-0 imaging sequence. Fluence measurements corresponding to these setups were performed with a PR-06 Farmer ion chamber (Capintec Instruments Inc, Pittsburg, PA) in a buildup cap providing electronic equilibrium. For the 6 and 15 MV beams, lucite buildup caps having external diameters of 3.8 cm and 5.8 cm, respectively, were used. Average pixel values from the ROI_{CAX} plotted as a function of temperature and pressure corrected ion chamber readings show that the pixel response increased approximately linearly with fluence for both beam energies (Fig. 2.24). aS500 EPID dose response calibration will therefore be more straightforward in comparison to a SLIC EPID.

2.5.4.2 Dose rate response

The dose rate dependence was studied by positioning the detector at an SED of 140 cm and taking open field images for 6 and 15 MV photon beams at all repetition rates. These measurements were conducted immediately following monthly calibration, when all the acquisition modes were calibrated. Each data point on the graph in Fig. 2.25 represents the average pixel value from the ROI_{CAX} for a particular dose rate. The response is dependent on the dose per frame delivered for each repetition rate. The graph shows sigmoid curves for both energies. This behavior can be explained by

51

considering the dose per frame and the frame rate used by the imager as provided by Varian. For the 6 MV beam, the counts/pixel/MU falls from 4714 to 4532 for repetition rates of 100 and 200 MU/min respectively and then increases for increasing repetition rates (i.e. from 300 to 600 MU/min). For the 15 MV beam there is a dip at the higher end because of the decrease in the value of counts/pixel/MU from 4084.3 to 4064.6 for the 500 and 600 MU/min repetition rates respectively [Po, 2001].

2.5.5 Lag Measurements

If there is any latent charge trapped in the detector photodiodes even after resetting, it will contribute to an increased pixel reading in the subsequent image frame. This is known as image lag. Lag in the nth frame has been defined as the ratio of the signal in frame n to the signal before radiation was interrupted [Pa, 2002]. We measured this "memory" effect caused by lag by irradiating the EPID using a 20 x 20 cm^2 open field and [6 MV, 300 MU/min, Standard scan] acquisition mode. Subsequent drift images (radiation off) were obtained after 30 sec and then at one min time intervals. Fig. 2.26(a) shows the steep fall-off of mean pixel values, normalized to the maximum reading from the open field image. A recent work by McDermott et al. has shown that the signal decay in the dark fields following an irradiation is faster for shorter beam times and does not depend on dose delivered [Mc, 2004]. In a second measurement, images of 6 x 6 cm^2 and 20 x 20 cm^2 fields were taken in immediate succession (interval of 35 sec) using the 0-50%-0 acquisition mode which we planned to use for dosimetry measurements [Es, 2001]. A ghost image of the smaller field, produced by the memory effect, is faintly visible in a narrow contrast window in Fig. 2.26(b). After an interval of 15 mins, an additional 20 x 20 cm^2 field image was taken and is shown in Fig. 2.26(c) using the same window and level setting as for Fig. 2.26(b)). The ghost image is no longer visible. Figure 2.26(d) shows corresponding profiles across the central regions of the above images. The differences in pixel values between the 20 x 20 cm^2 background region and the ghost image region in Fig. 2.26(b) are typically ~1%, and vanish in Fig. 2.26(c). This suggests that the phenomenon of incomplete readout is generally negligible for this acquisition mode where images are

acquired at the middle of treatment beam delivery, using the aS500 EPID, especially if images are acquired a few minutes apart. On the other hand, if an imaging sequence is performed in quick succession at the beginning of treatment delivery, the ghosting effect can be significant and has been found to change the EPID response by ~3% if no corrections are applied [Mc, 2004].

2.6 SUMMARY

This chapter describes the acceptance tests and initial work performed with the aS500 EPID to determine some of its fundamental operating characteristics. The acceptance data have been set as a baseline for monthly calibrations and quality assurance measurements. An additional set of measurements was performed to select appropriate operational parameters when using the EPID for dosimetry. Starting with the default values, some of the imaging parameters were changed to produce images of better quality or to provide better operational stability.

The number of resets appeared to affect pixel values but as these remained fairly constant from 5 to 10 resets, we selected 5 resets for our subsequent experiments. We observed that image quality was not markedly improved with the introduction of a start delay at the beginning of the image acquisition process. In any case for our dosimetry measurements, since we are using the 0-1-0-type acquisition, the need for a start delay does not arise. Images of open fields turned out to be the most uniform and artifact-free when no sync delay was introduced. Apart from reducing counting noise, changes in the number of frame averages did not seem to affect pixel values, and hence the default value of 2 frame averages was accepted for dosimetry. It was determined that the image-forming layer of the EPID lay 1.3 cm below the top of the detector stack and that the pixel pitch of the detector was 0.783 ± 0.001 mm when this offset is taken into consideration.

The response of the EPID was found to be linear with respect to dose for open fields. Although the response with changes in linac repetition rate was hypothesized to also be linear, we observed that it was not. Suitable acquisition parameters for

dosimetry for 6 and 15 MV photon are a repetition rate of 300 MU/min, standard quality mode, and a 0-1-0 type acquisition. Extra solid water buildup required atop the EPID to produce electronic equilibrium was determined to be 0.5 cm for the 6 MV beam and 2.0 cm for the 15 MV beam. The effect of lag on aS500 images obtained with our 0-50%-0 acquisition mode was found to be negligible.

In conclusion, the work described in this chapter provided us with a better understanding of aS500 EPID operation and yielded a list of parameters appropriate to the use of the EPID for dose measurement.

2.7   APPENDIX

Appendix 2.1: Changeable parameters in the IAS2 Service Monitor

Table A1(a). Scanning Modes

	Standard	High
Default row cycle time (µs)	250	250
Default Binning Horz.	2	2
Default Binning Vert.	2	2
Start delay (ms)	0	0
Default Frame Averages	2	10
# of frames for DF Cal images	60	60
# of frames for FF Cal images	30	30

Table A1(b). Treatment Acquisition Mode

	6MV, Standard		15MV, Standard	
	100 MU/min	400 MU/min	100 MU/min	400 MU/min
PV Sync (1/10 Hz)	600	3600	300	1800
Binning Horizontal	2	2	2	2
Binning Vertical	2	2	2	2
Sync delay (us)	0	0	0	0
Bias Voltage	-5V	-5V	-5V	-5V
IDU Gain	Gain2	Gain2	Gain2	Gain2
Pulse pattern	1	4	1	4
ACPU input	Image Signal	Image Signal	Image Signal	Image Signal
Rows/PV sync	22	9	22	18
Pulse hopping	1	1	1	1
ACPU gain	4	2	4	2
Frame Averages	2	2	2	2

Table A1(c). Energy Lookup

Dose Rate (MU/min)	Pulse pattern	PV Sync (Hz)
100	1	60
200	2	120
300	3	180
400	4	360
500	5	360
600	6	360

Table A1(d). No Radiation Acquisition Modes

Image Type	Saw Tooth	IDU Noise	IDU Test	ACPU Ground	ACPU Noise	Auxilia-ry	IDU drift	Test Image
ACPU gain	Gain 1	Gain 2	Gain 2	Gain 8	Gain 8	Gain 1	Gain 2	Gain 1
Binning Horz	2	2	2	2	2	2	2	2
Binning Vert	2	2	2	2	2	2	2	2
Rows/PV sync	384	384	384	384	384	384	384	384
Frame Averages	1	1	1	1	1	1	1	1
PV Sync (1/10 Hz)	25000	25000	25000	25000	25000	25000	25000	25000
IDU Gain	Gain 2	Gain 2	Gain 2	Gain 8	Gain 8	Gain 1	Gain 2	Gain 1
Bias Voltage	-5V	-5V	-5V	-5V	-5V	-5V	-5V	-5V

56

Table A1(e). Calibration Sets

	6MV, Standard		15MV, Standard	
	100 MU/min	400 MU/min	100 MU/min	400 MU/min
IDU gain	Gain 2	Gain 2	Gain 2	Gain 2
ACPU Gain	Gain 4	Gain 2	Gain 4	Gain 2
Auto Calibration	Yes	Yes	Yes	Yes
Treatment acquisition mode	6MV, 100 MU/min, Standard	6MV, 400 MU/min, Standard	15MV, 100 MU/min, Standard	15MV, 400 MU/min, Standard
Energy (MV)	6	6	15	15
Dose rate (MU/min)	100	400	100	400
Date & Time of last Calibration	mo/dd/yy	mo/dd/yy	mo/dd/yy	mo/dd/yy
Flood field location	IAS2/CALIBRAT/ flood-1-6MV.cal	IAS2/CALIBRAT/ flood-4-6MV.cal	IAS2/CALIBRAT/ flood-1-15MV.cal	IAS2/CALIBRAT/ flood-4-15MV.cal
Dark field location	IAS2/CALIBRAT/ dark-1-6MV.cal	IAS2/CALIBRAT/ dark-4-6MV.cal	IAS2/CALIBRAT/ dark-1-15MV.cal	IAS2/CALIBRAT/ dark-4-15MV.cal

Appendix 2.2: aS500 EPID terminology

Acquisition central processing unit (ACPU) input: The analog input has to be switched to different sources for different types of acquisitions. The software assigns numbers to the selections: 0→Image signal, from the detector; 1→Auxiliary signal, spare input is not used; 2→Saw Tooth, ACPU on-board saw tooth generator; 3→Ground input, APCU ground.

ACPU gain: The gain of the acquisition CPU has a value ranging from 0 to 3. The default value is 0. Range: minimum = 0, maximum = 3, and default = 0.

Bias voltage: The bias voltage of -40 mV is the minimum voltage that is applied to each photodiode in the a-Si array. The maximum negative voltage that may be applied is –5V.

Dark field image: A dark field image provides information about background noise and is obtained by taking a base reading for each pixel in the absence of radiation.

Default row cycle time: It is the minimum time required for reading out the data from a row automatically. Range: minimum = 100 µs, maximum = 10,000 µs, and default = 500 µs.

Dose Rate Servo (DRS): Integral dose rate servos are present in medical linear accelerators to maintain a steady output. In Varian dual energy linacs, the dose rate is adjusted by varying the beam pulse length.

DRS minimal switch time: DRS minimal switch time is the minimum time between two sequential images within which the DRS can be switched from non-regulating mode back to regulating mode. If the minimum switch time is greater than the time interval between images, the DRS remains non-regulating during the interval. Range: minimum = 0 s, maximum = 3000 s, and default = 10 s.

DRS stabilization time: DRS stabilization time is the time for which the DRS is switched off prior to image acquisition. Unlike the start delay, which only applies to the first image of a sequence, the DRS stabilization time applies to all intervals between images. Range: minimum = 0 ms, maximum = 5000 ms, and default = 250 ms.

58

Flood field image: It is an open field image covering the entire sensitive area of the detector used to correct for variations in individual pixel sensitivity and radiation field inhomogeneity.

Frame Averages: A number of image frames may be acquired and averaged to improve image quality. This parameter can be altered in two places in the software: (a) in the administration menu, where the effect will be on the object images (2 frames averaged), and (b) in the IAS2 service monitor, where the effect will be on the test images that are acquired after calibration (usually 4 frames are averaged). Range: minimum = 1, maximum = 4,000.

Imaging sequence: The imaging sequence represents the times during a treatment cycle when images are acquired. For example a 0-50%-0 imaging sequence is one where imaging is performed at the mid point of treatment delivery.

Number of frames for DF and FF images: The number of frames that are acquired and averaged for dark and flood fields during calibration are set at 60 and 30, respectively by the manufacturer. However these values can be changed to suit the preferences of the user.

Pulse hopping: The number of beam pulses that are skipped during EPID readout. For example, if the pulse hopping value is 2, then every second beam pulse is used to produce an image. The default value is 1 where every pulse is used and the maximum value is 100.

PV sync: PV sync, which is used for image row readout synchronization, is the frequency of the timing pulses generated by the aS500 trigger board, and is based on accelerator repetition rate (Fig. 2.3). Range: minimum = 0 Hz, maximum = 5,000 Hz, and default = 10 Hz.

Resets: are performed on the a-Si array electronics to zero any residual charge in the pixels that would otherwise contribute to the subsequent image frame.

Start Delay: Start delay is the time between linac beam on and the beginning of image acquisition. This time may be increased to allow for the beam to stabilize, since portal images are acquired when the DRS is in the non-regulating mode. There is no specific default value indicated for the start delay.

59

Sync Delay: Sync delay is the wait time after the beam pulse has stopped and before image row scanning begins. Range: minimum = 0 µs, maximum = 26,000 µs, and default = 0 µs.

Treatment spare time: Measured in milliseconds, it is the calculated estimate of the spare time between the end of the last image and end of the planned treatment.

Table 2.1

Specifications of Varian aS500 EPID serial no: 803860

Commercial name	Varian PV aS500 EPID
Array dimension	40×30 cm^2
Array format	512×384
Pixel	n-i-p photodiode
Pixel pitch	0.784 mm
Diode fill factor	0.83
Photodiode bias voltage	-5 V
TFT dimension	88×11 μm^2
Maximum frame rate	8 frames/sec
Metal converter	1 mm Cu
Phosphor converter	133 mg/cm^2 Gd$_2$O$_2$S:Tb

Table 2.2

Object contrast as a function of hole depth and photon energy for the contrast
detail phantom [Po, 2000b].

Hole Depth (mm)	Object Contrast (%)	
	6MV	15 MV
0.25	0.15	0.10
0.5	0.30	0.19
1.0	0.59	0.38
2.0	1.17	0.76
3.0	1.75	1.05

Table 2.3

Mean pixel values from ROI_{CAX} of two images taken for different numbers of frame averages for the 6 MV beam.

Frame Averages	Pixel value	Stability (%)
1.0	2351.5	2.9
2.0	2445.7	2.3
4.0	2470.6	2.4
5.0	2396.3	2.7
6.0	2450.2	2.3
8.0	2452.1	2.5
10.0	2448.3	2.5
25.0	2488.5	2.3
50.0	2538.5	2.1
100.0	2579.0	2.1

Table 2.4

Average pixel value and noise from sequential dark field images acquired at 5 sec intervals.

Dark Frame #	Av. value in image	Noise %
1	22.7	84.8
2	20.6	94.1
3	22.6	85.1
4	22.9	84.7
5	21.5	90.3
6	22.4	86.5
7	21.1	91.2
8	21.6	89.5
9	22.5	86.7
10	22.9	84.0

62
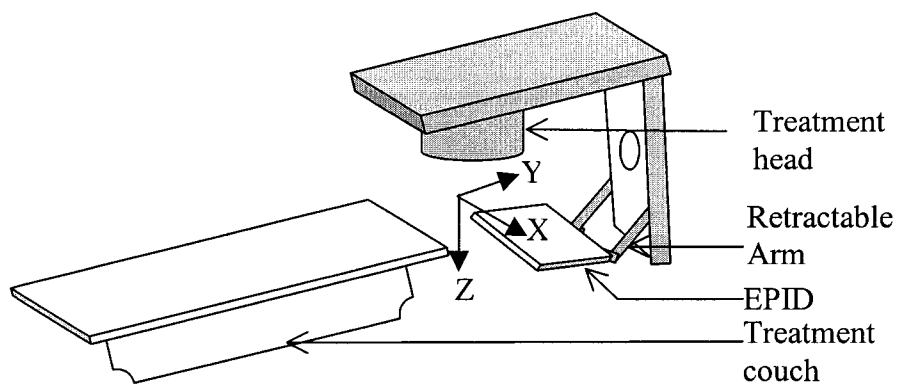
Figure 2.1: Figure shows the EPID attachment on the linac with the retractable arm and the Cartesian co-ordinate system used in this work. The origin of the coordinate system is at the linac isocenter.

(a)

Detector stack

Gate Lines

Data Lines

(b)

Radiation

Cu plate
Gd_2O_2:Tb phosphor
a-Si Photodiodes

Associated Electronics
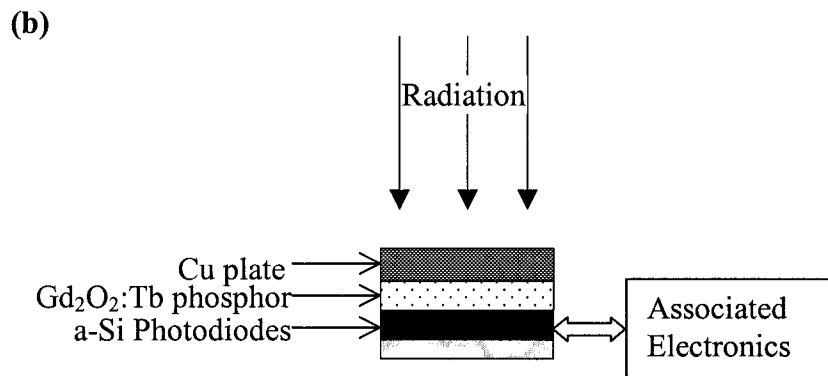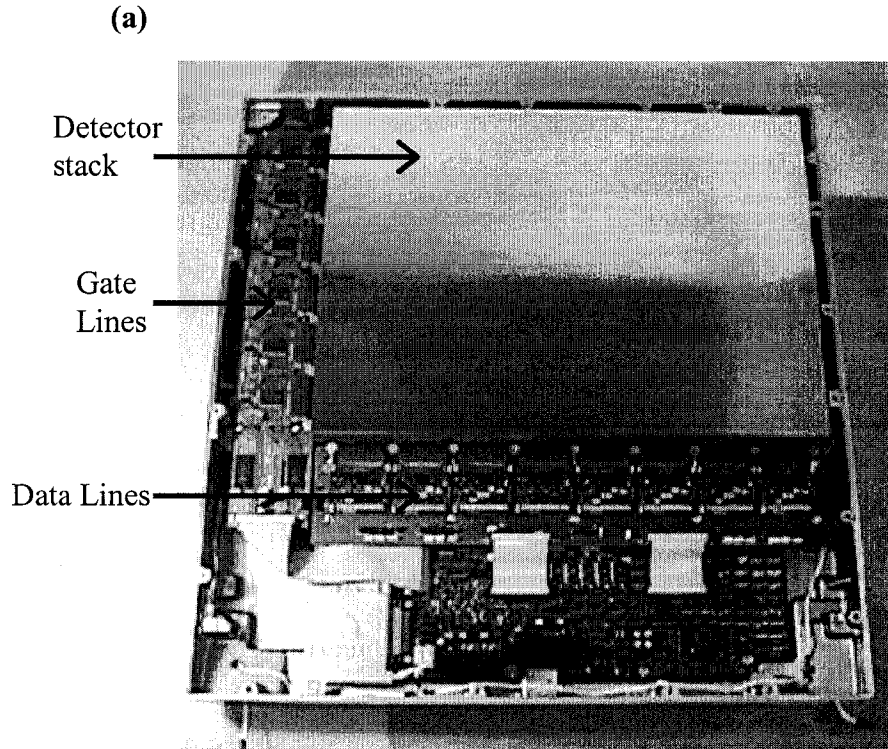
Figure 2.2: **(a)** The aS500 EPID Image Detection Unit with the protective covering removed, showing the detector stack and electronics inside [Ve, 2004]. **(b)** The four main parts of the detector (not drawn to scale).

64
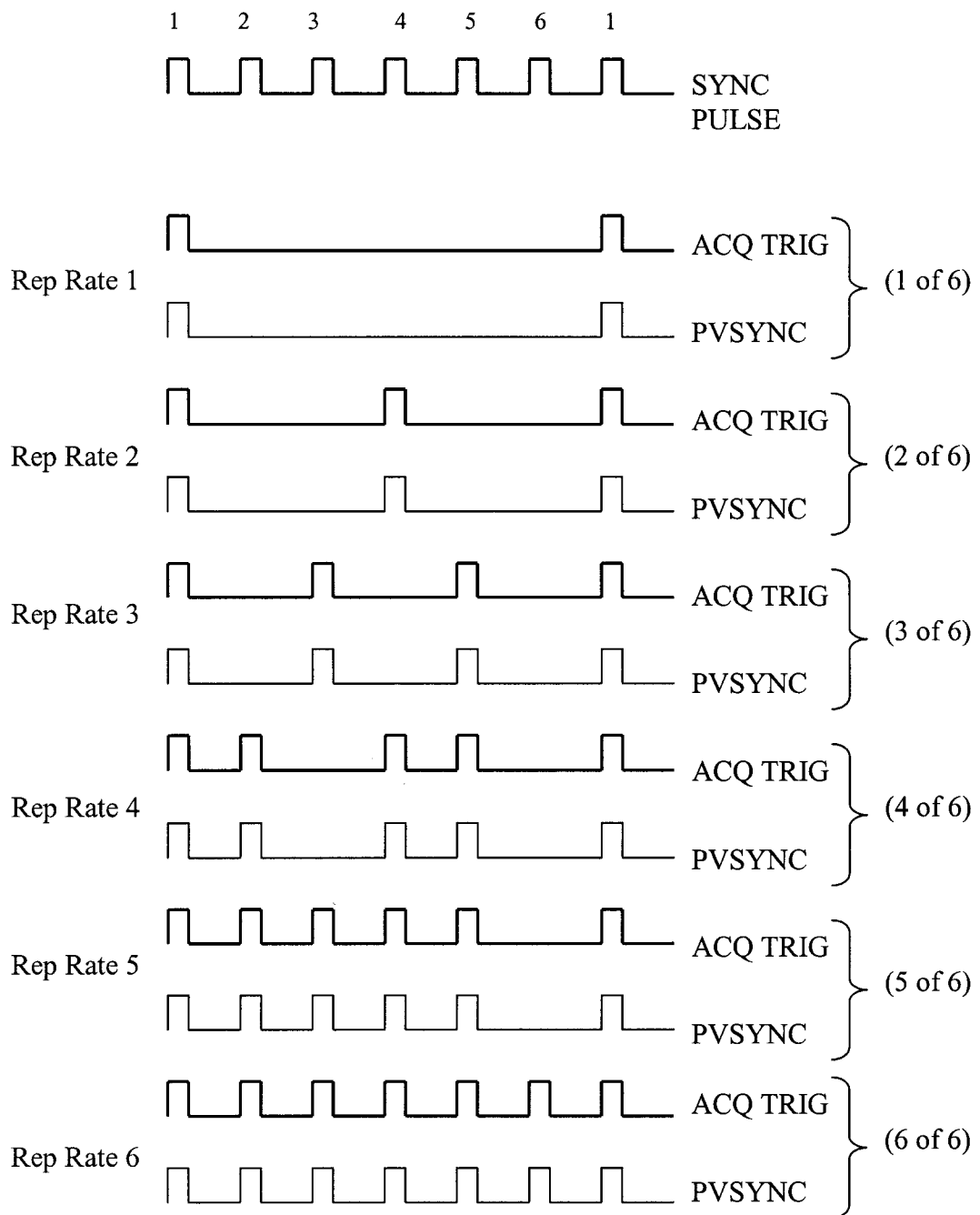
Figure 2.3: 2300 CD linac radiation pulse patterns ACQ TRIG [Po, 2000a]. The 6 different EPID synchronization pulse sets PVSYNC represent the six repetition rates of the linac from 100 to 600 MU/min.
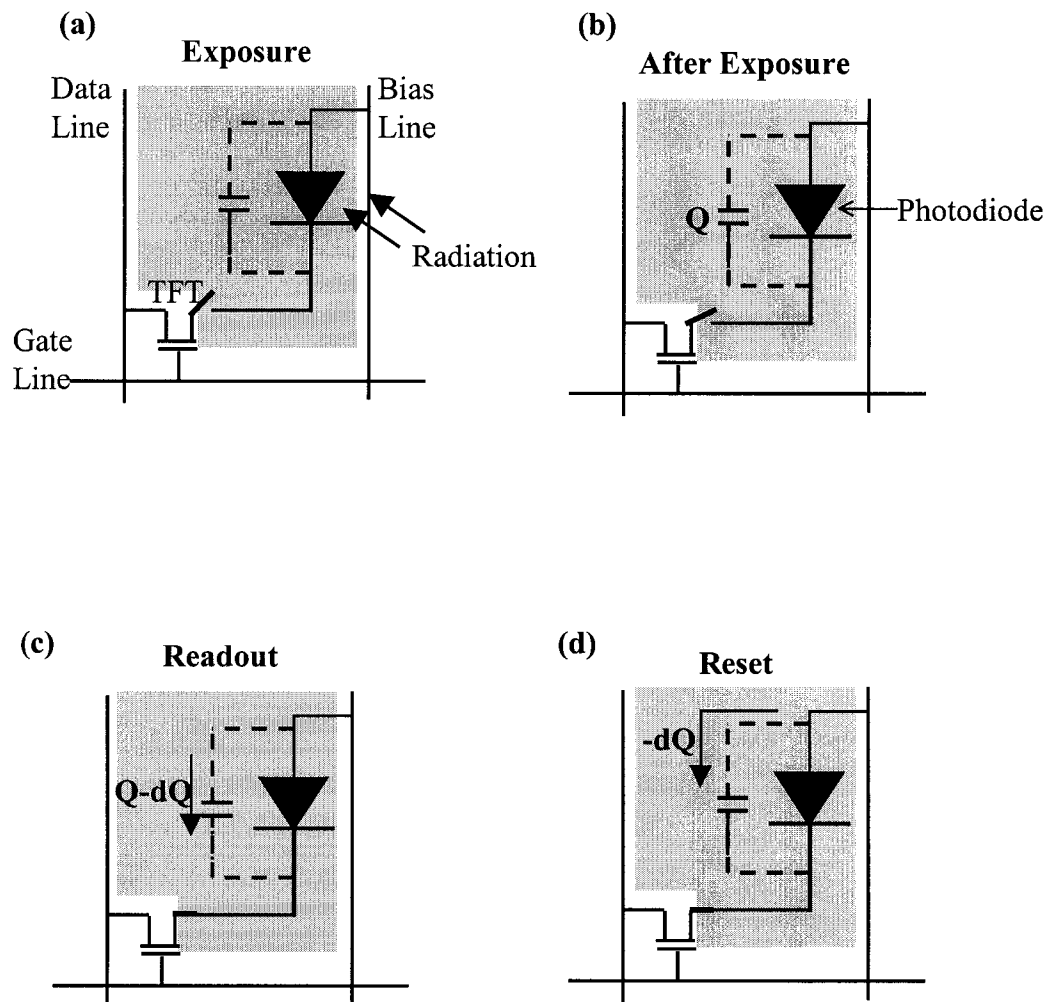
Figure 2.4: Readout concept for a single a-Si pixel. **(a)** Irradiation of the pixel; **(b)** Charge (Q) accumulation in the photodiode capacitance; **(c)** Charge readout through the closed gate terminal of the TFT; and **(d)** Resetting of the pixel to remove the residual charge dQ.

66

GANTRY
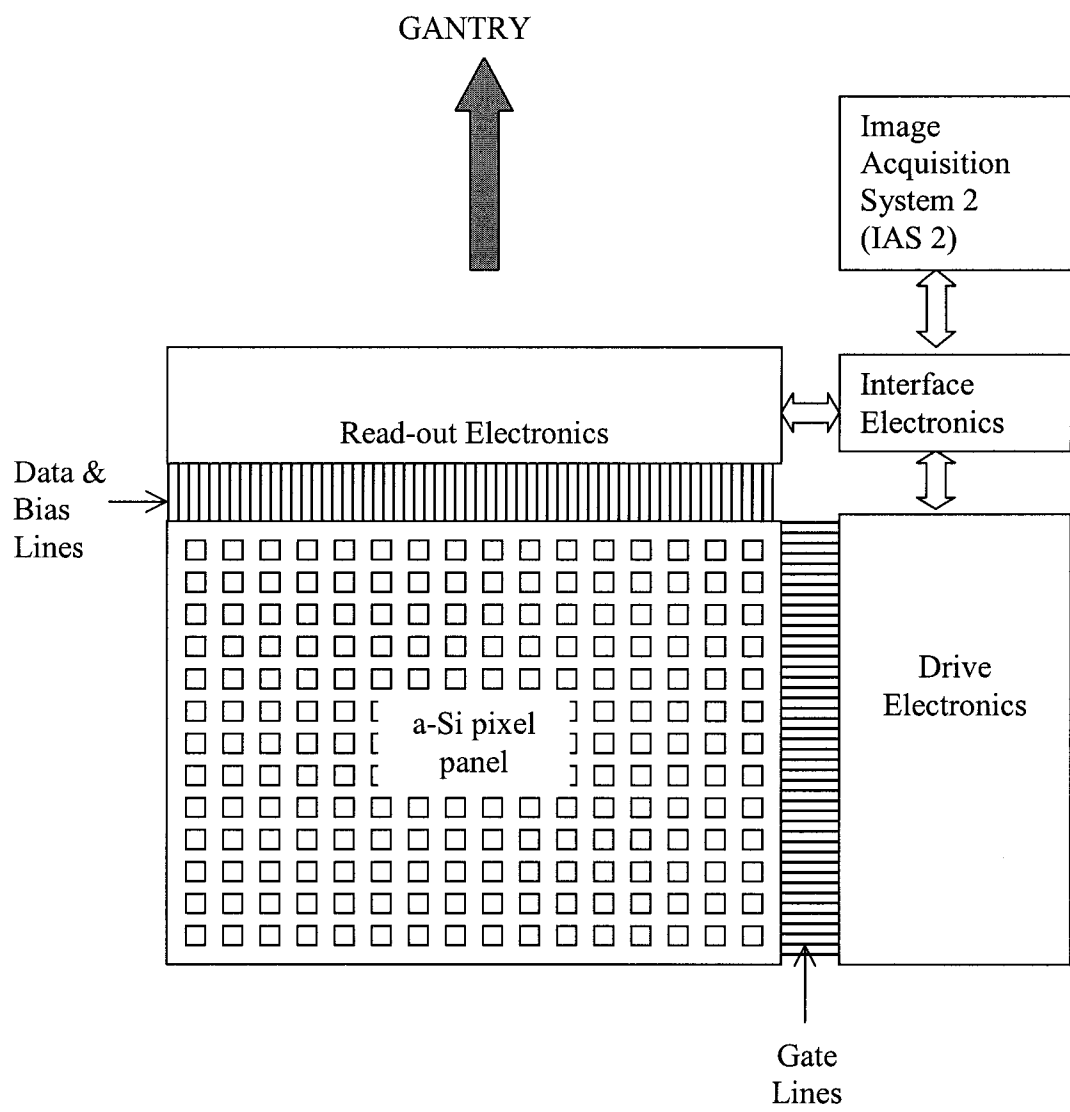
Figure 2.5: Schematic drawing of the Image Detection Unit in the aS500 EPID [Po, 2000a].
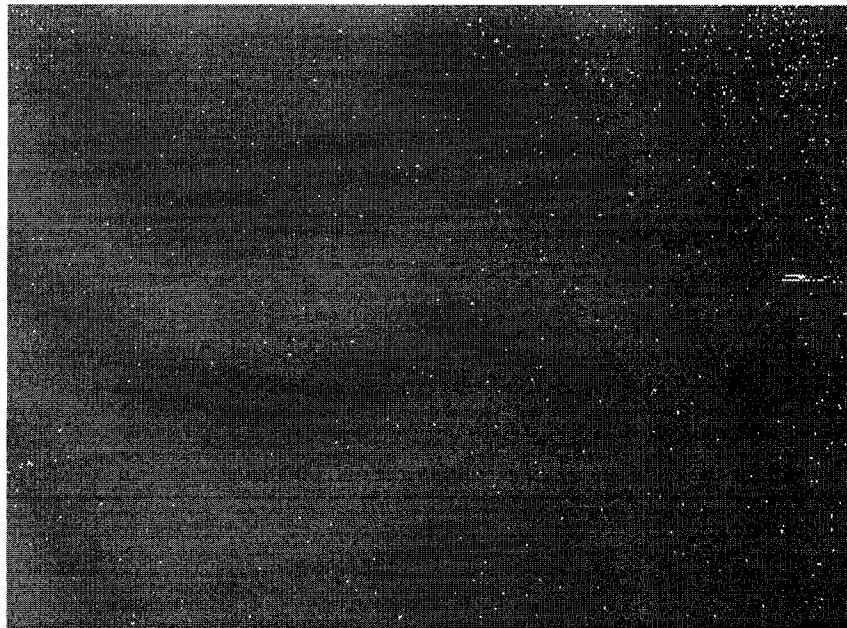
Figure 2.6: The pixel defect map for our aS500 EPID showing the 880 pixel defects identified at the time of transfer onto the Clinac 2300CD linac.
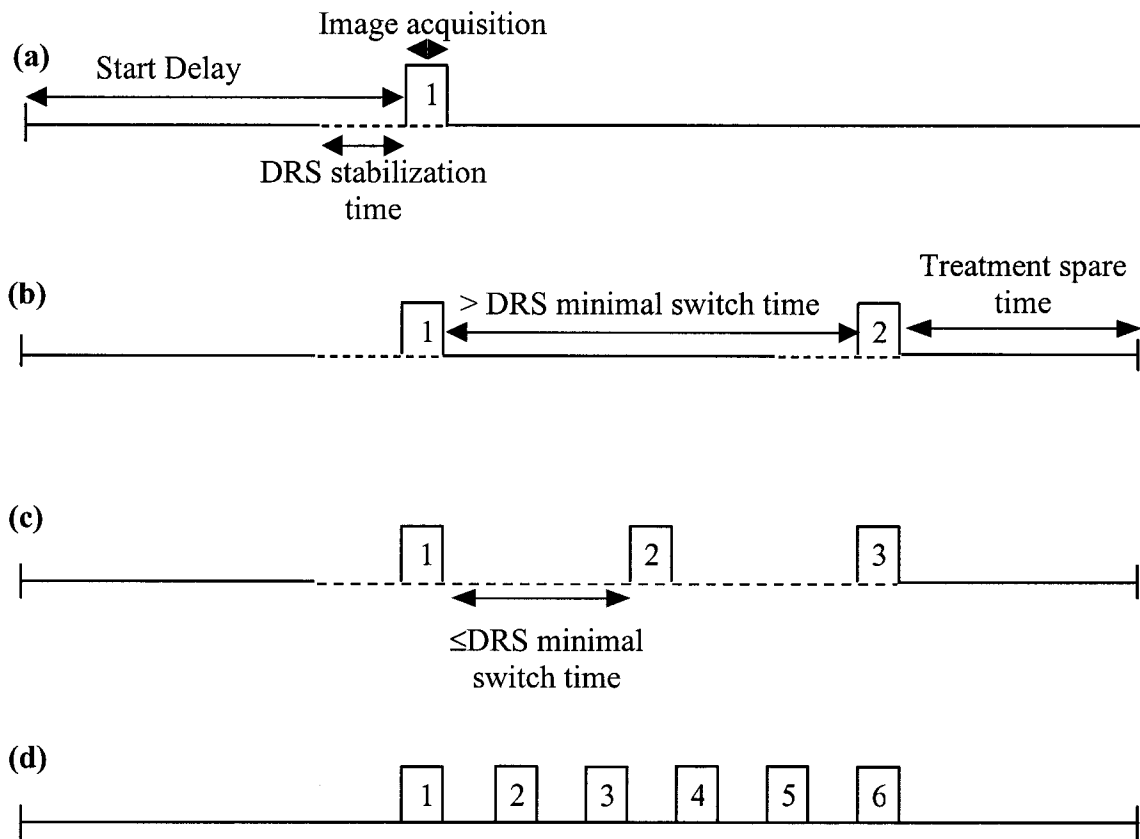
Figure 2.7: The figure shows different imaging sequences and the DRS operation. The solid and dashed lines represent time intervals when the DRS is regulating and not regulating, respectively. Refer to the text for further details. **(a)** Single image acquisition, **(b)** Double image acquisition where DRS can switch on between the two acquisitions, **(c)** Sequential image acquisition where DRS cannot switch to regulating mode, and **(d)** Flood field acquisition where DRS remains in regulating mode.

69

(a)

1 FRAME
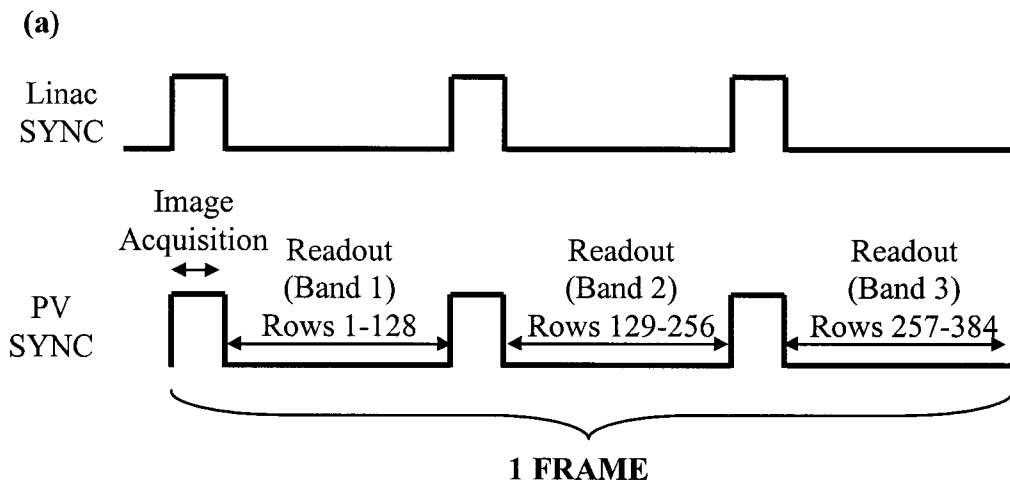
(b)
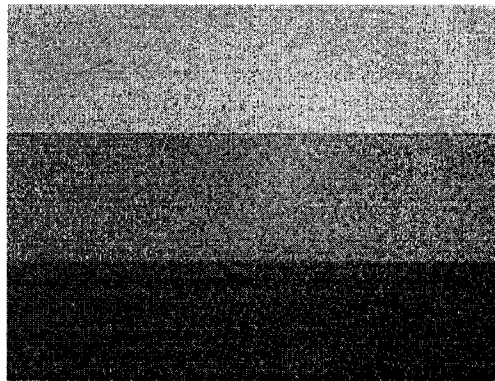
Figure 2.8: (a) Image acquisition and readout protocol for a [15 MV, 100 MU/min, Standard scan] acquisition. (b) Open field image obtained using this protocol. The average pixel values in a 20x20 pixel ROI in the center of each band are 1266.6, 1272.1, and 1283.2 respectively.

| (a) | (b) | (c) |
| Min: 425, Max: 1119 | Min: 729, Max: 3079 | Min: 2551, Max: 2619 |
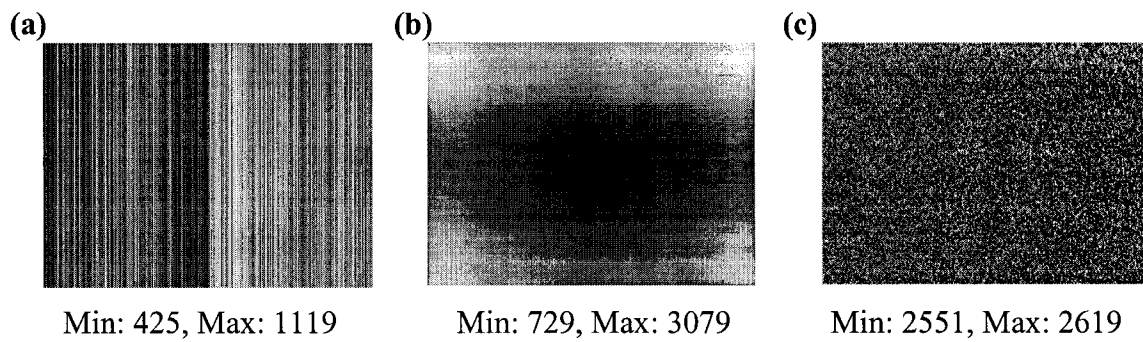
Figure 2.9: Images of a **(a)** dark field, **(b)** flood field, and **(c)** test image taken using the [6 MV, 300 MU/min, standard scan] acquisition mode. The minimum and maximum pixel values in each image are reported.

71
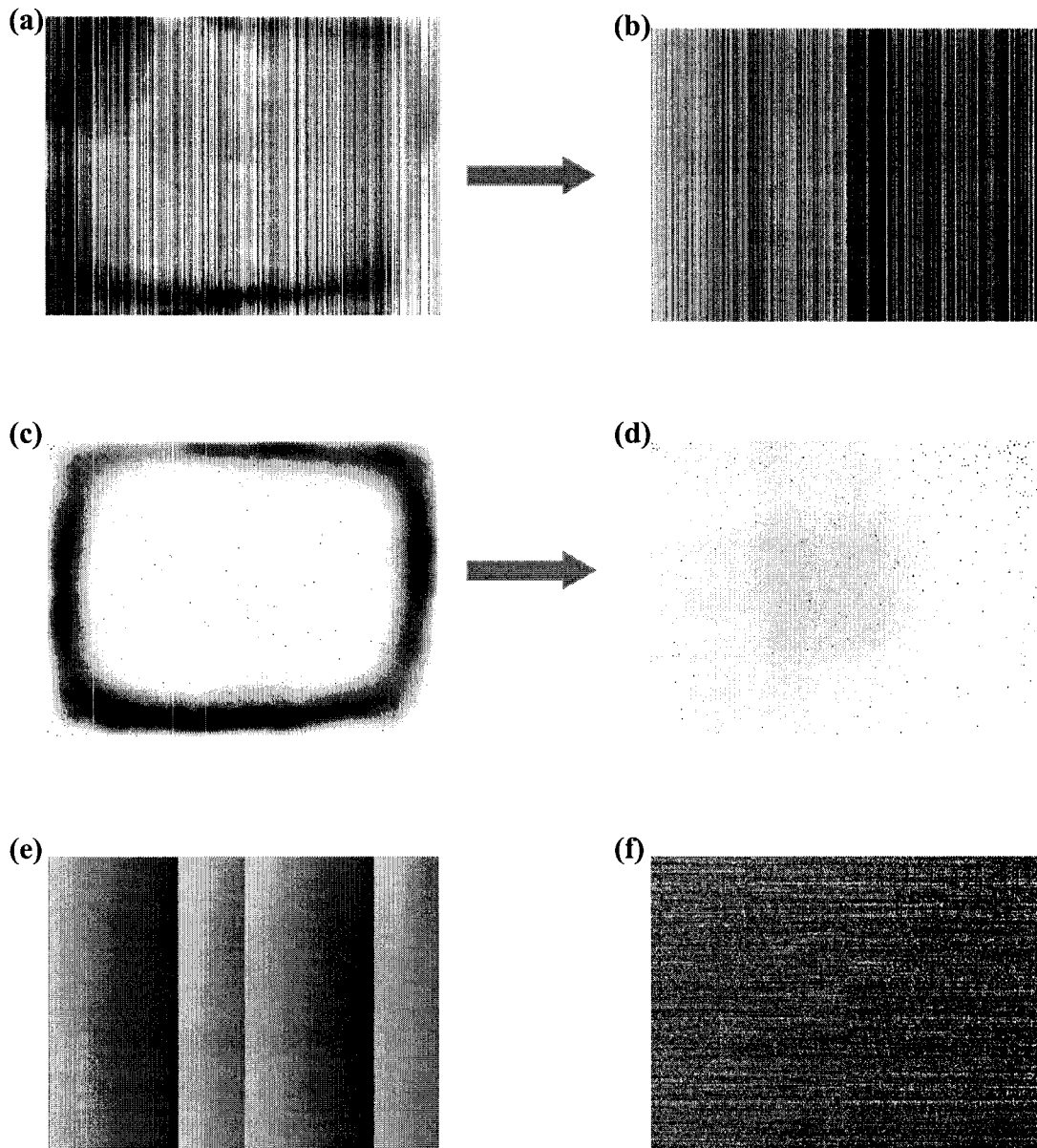
Figure 2.10: **(a)** IDU Test image (with old IDU); **(b)** IDU Test image (with new IDU); **(c)** IDU Drift image (with old IDU); **(d)** IDU Drift image (with new IDU); **(e)** Saw-tooth image (with new IDU); and **(f)** IDU Noise image (with new IDU).

72

(a) **(b)**
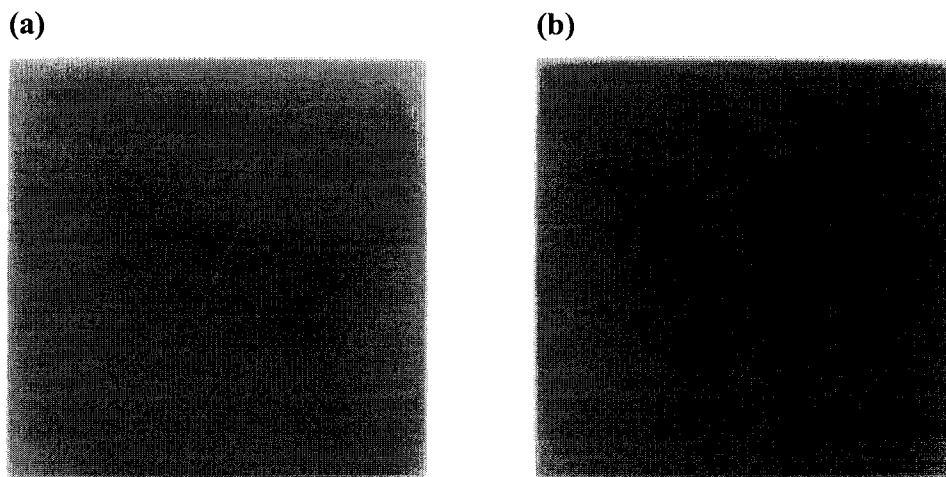
Figure 2.11: Acceptance test images for spatial resolution using a 1 mm diameter stainless steel wire taken using **(a)** 6 MV and **(b)** 15 MV photon beams.
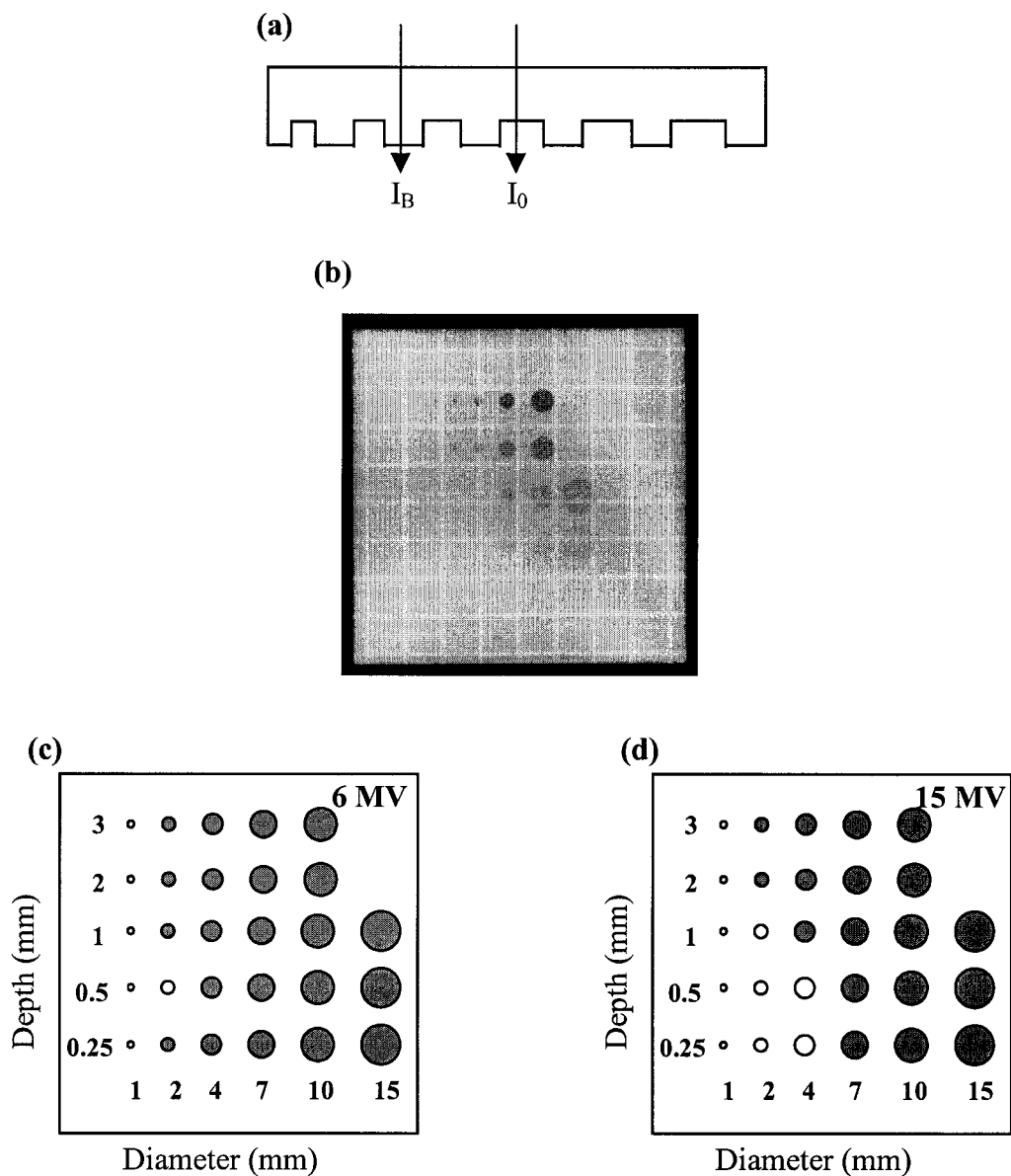
Figure 2.12: **(a)** A slab object showing the transmitted intensity through the background (I_B) and the object within the slab (I_0). **(b)** Portal image of the contrast-detail phantom [6 MV, 300 MU/min, standard scan]. The tennis racket insert on the couch causes the grid pattern seen in the image. The shaded circles represent the holes visible at the time of acceptance for **(c)** 6 MV, and **(d)** 15 MV photon beams.
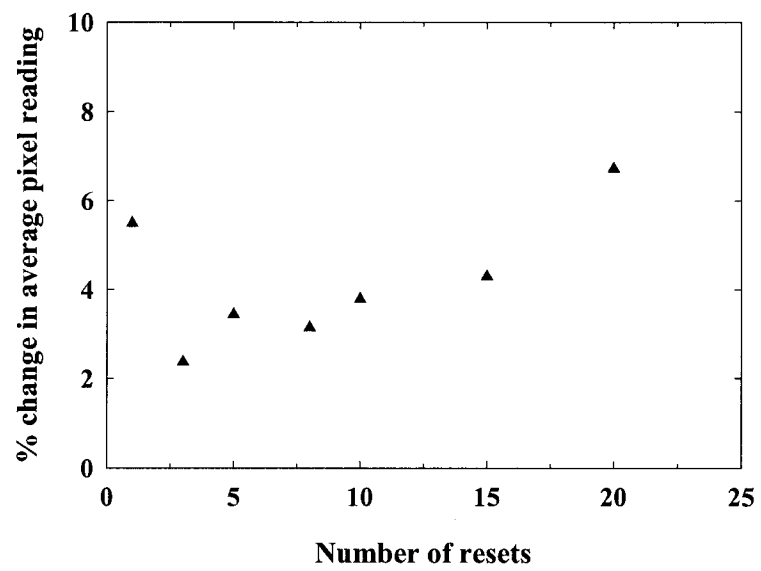
Figure 2.13: Change in ROI$_{CAX}$ average pixel values for increasing number of resets.

75
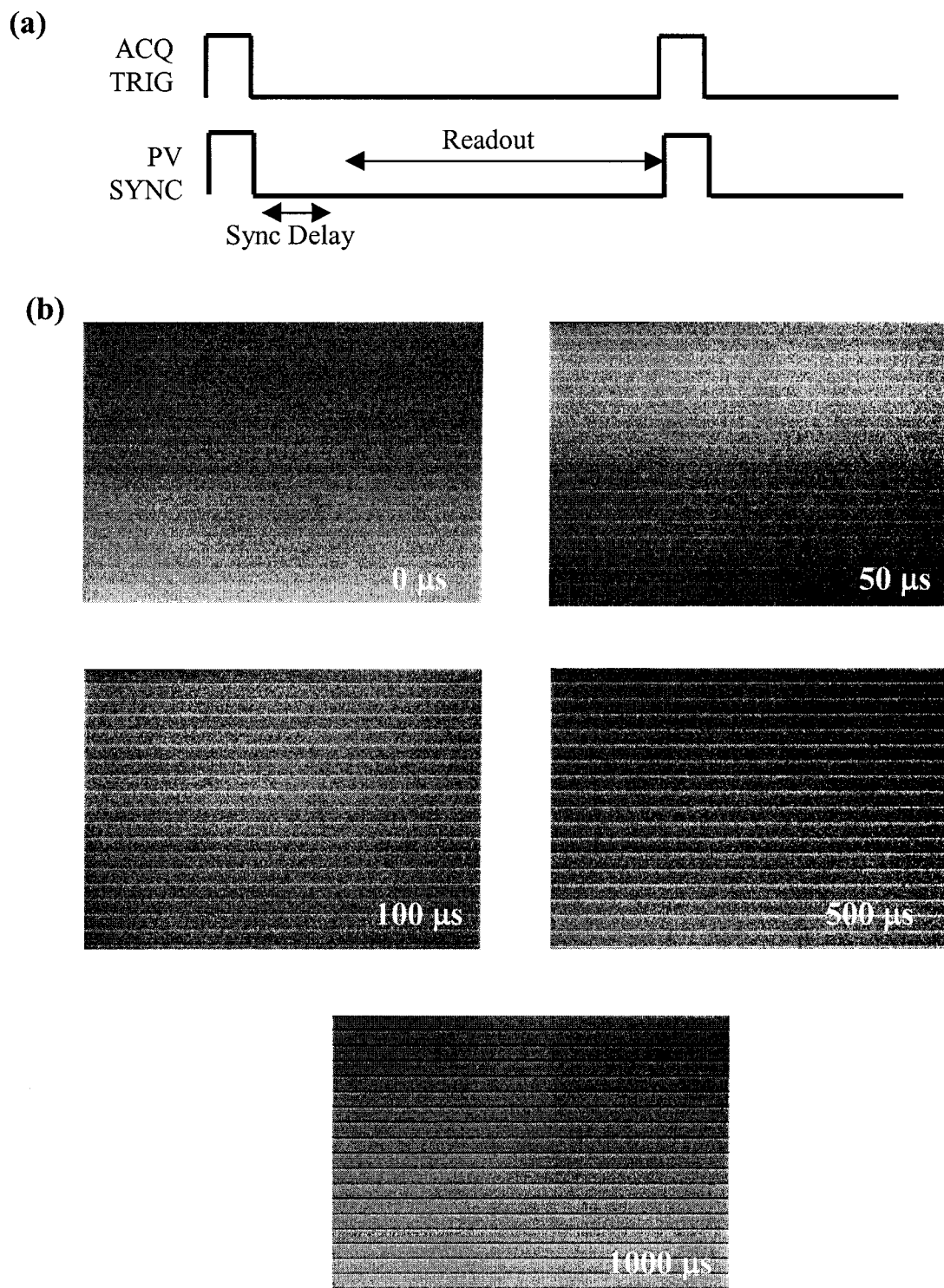
Figure 2.14: **(a)** Image acquisition timing showing the sync delay, and **(b)** open field images with increasing sync delays.
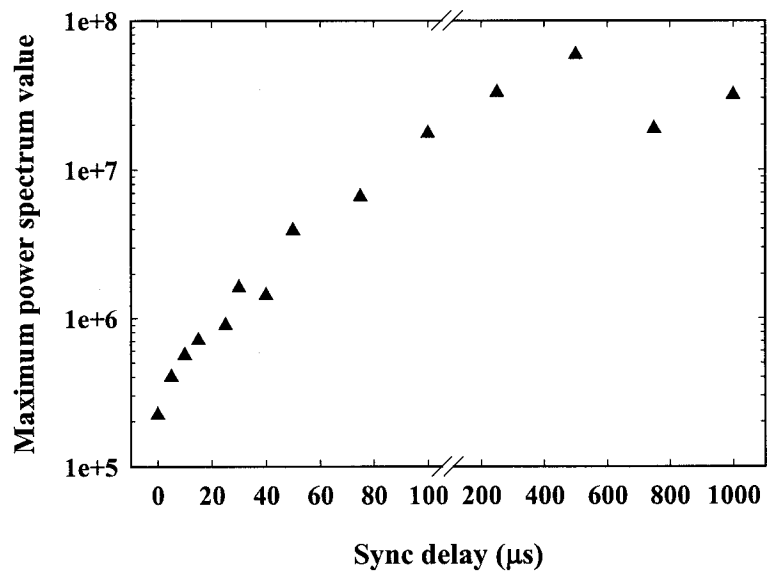
Figure 2.15: Variation with increasing sync delay in the maximum power spectral value for a signal comprised of the sum of all columns in an image.
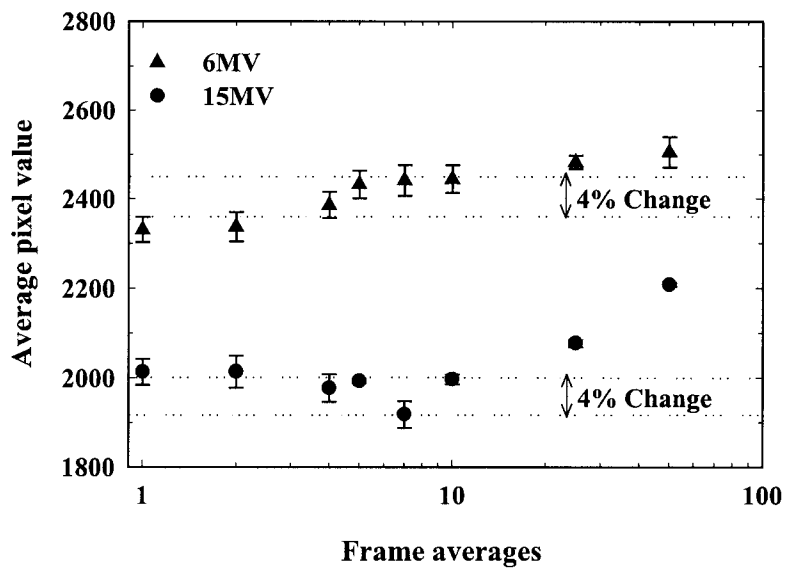
Figure 2.16: Change in ROI_{CAX} average pixel values with increasing number of frame averages. This data was acquired on a later date with respect to that shown in Table 2.3. The error bars represent a 1 S.D. variation, estimated from a set of four images.

78
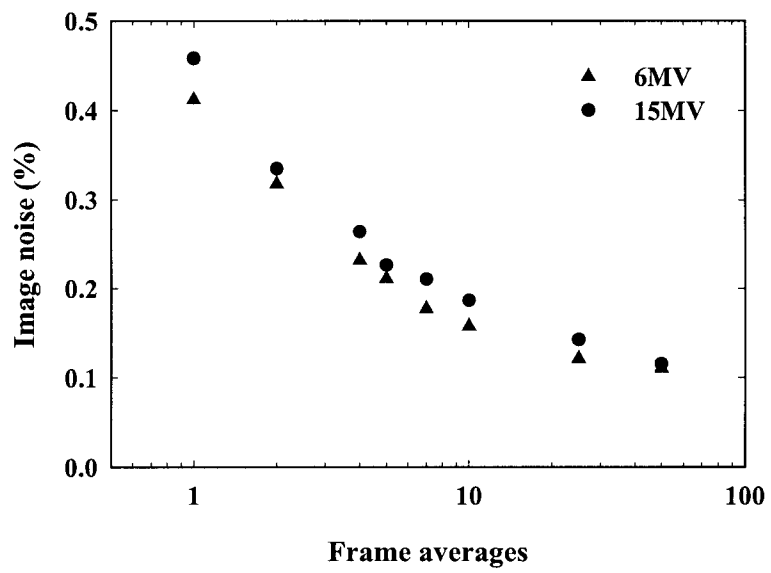
Figure 2.17: Reduction in image noise with increasing number of frame averages.
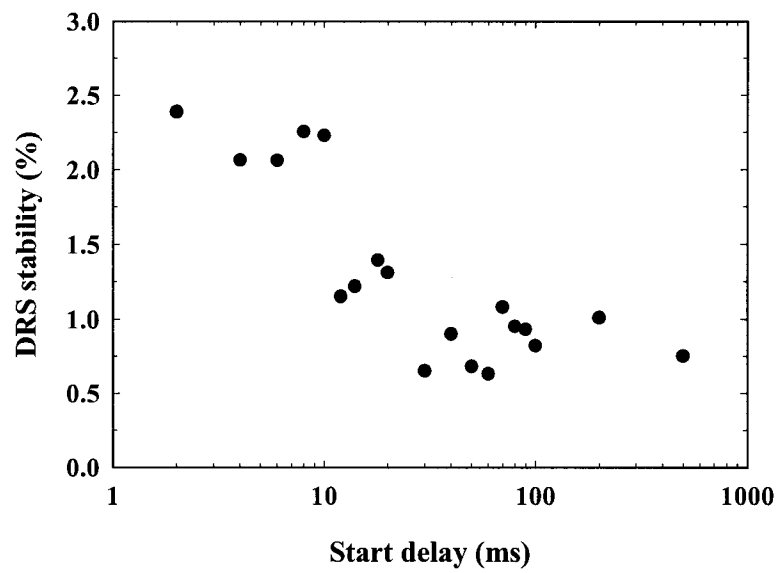
Figure 2.18: Variation in DRS stability with increasing start delay.

80
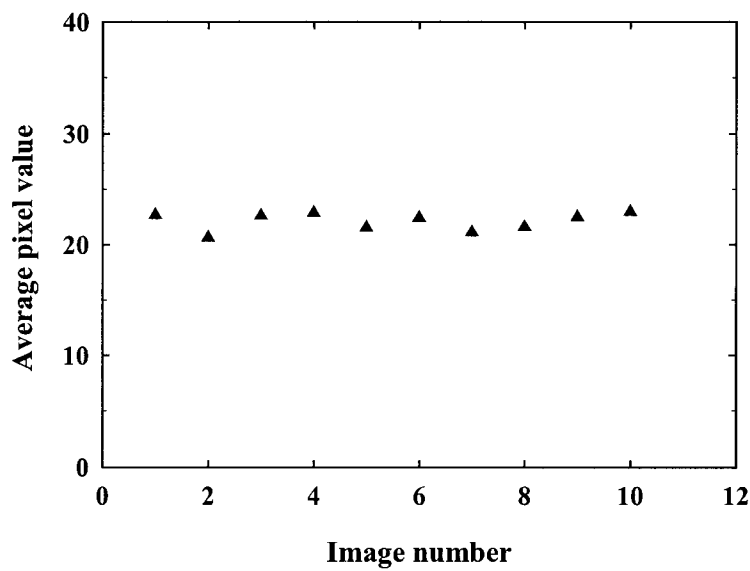
Figure 2.19: Average pixel value in the ROI_{CAX} for sequentially acquired dark field images. The time interval between acquisitions was 5 seconds.

81
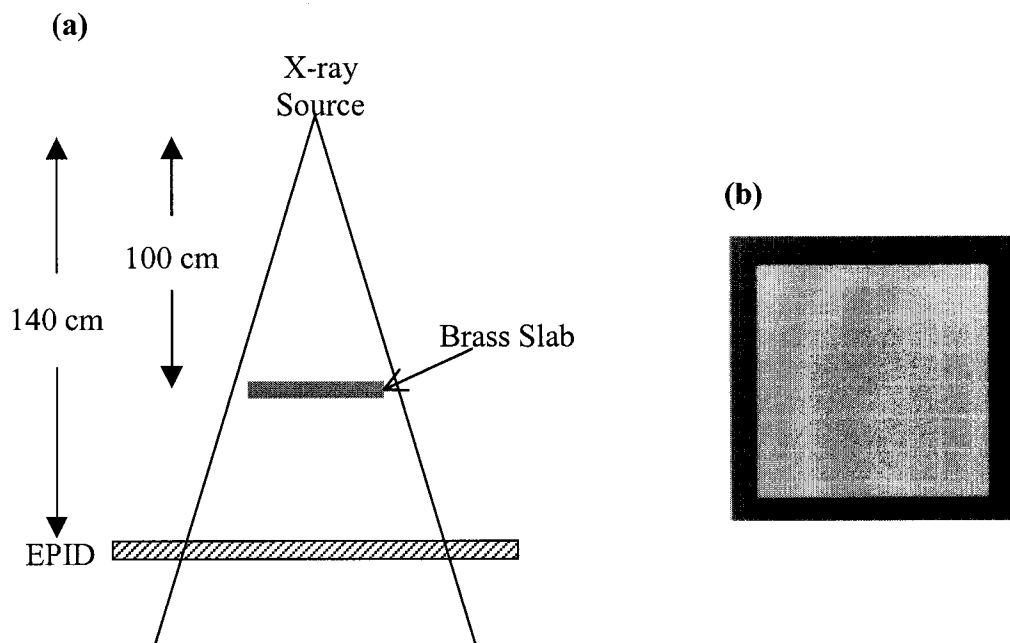
Figure 2.20: (a) Setup for pixel pitch determination with the brass slab. (b) The image on the right shows the brass slab in the radiation field. The grid lines on the image are caused by the tennis racket insert of the couch.

82
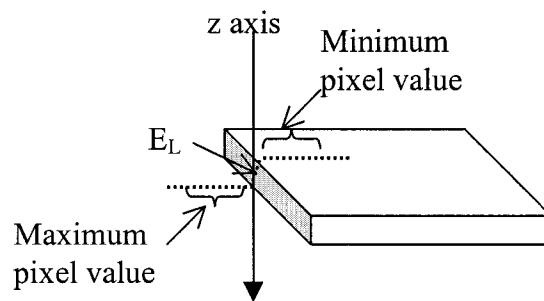
Figure 2.21: The figure shows the location of the maximum and the minimum pixel values for the calculation of pixel pitch. E_L is the calculated position of the left edge of the slab.

83
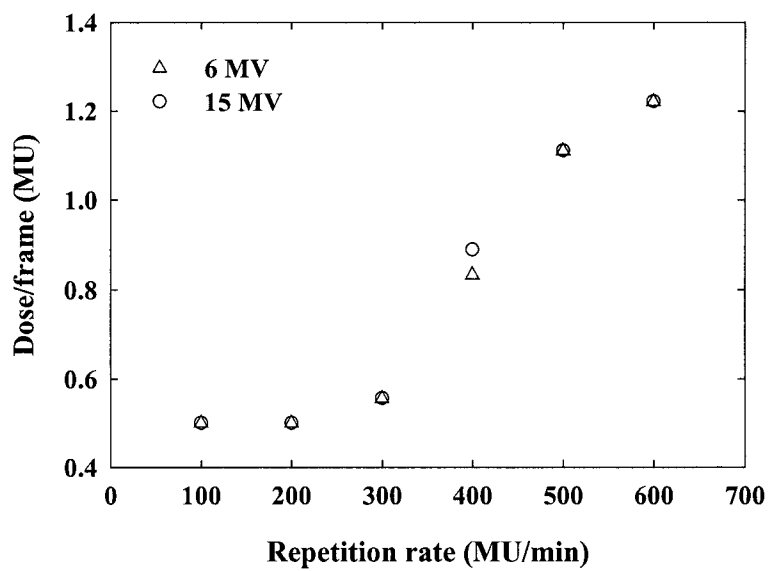
Figure 2.22: Monitor units needed to acquire a single frame image vs. linac repetition rate for the aS500 EPID [Po, 2001].
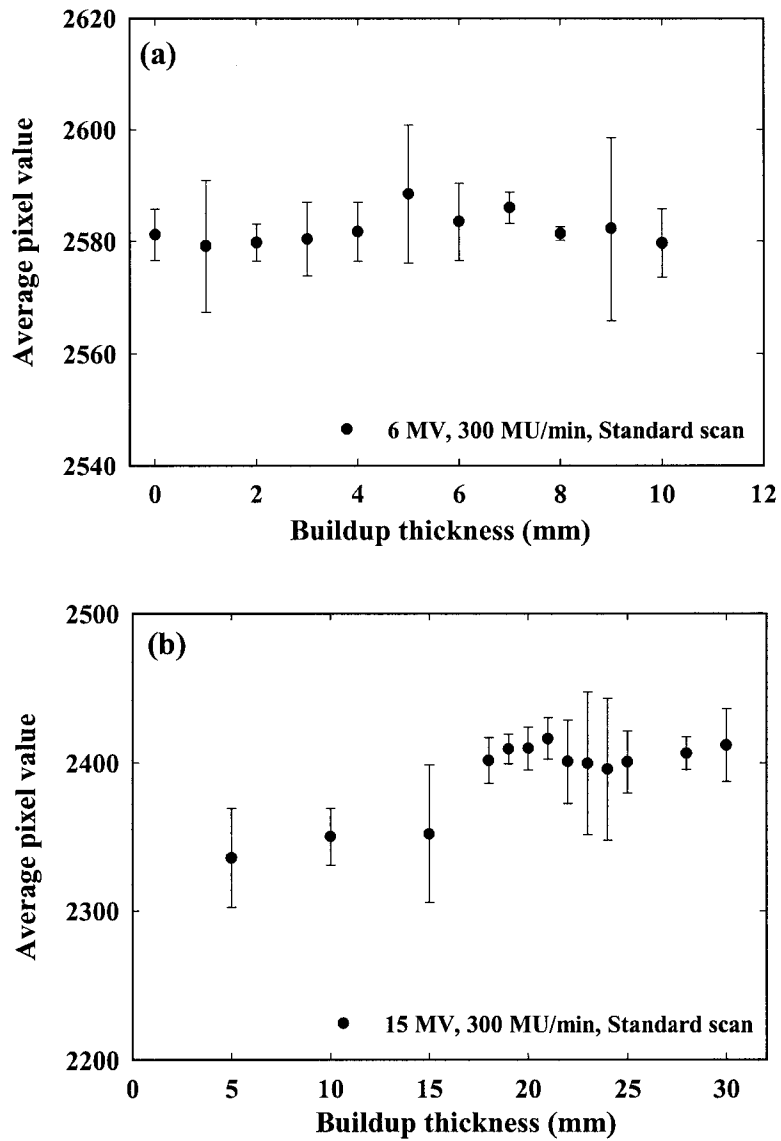
Figure 2.23: ROI$_{CAX}$ average pixel value vs. additional buildup thickness of solid water for **(a)** 6 MV and **(b)** 15 MV photon beams.

85
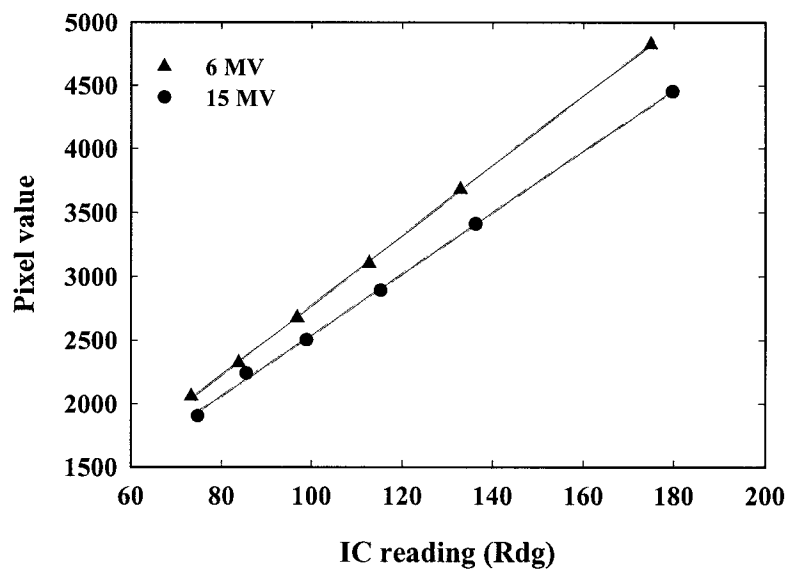
Figure 2.24: Average pixel value in a 20x20 pixel region of interest along the central axis versus energy fluence measured with a Farmer ion chamber. The data was obtained by varying the source to detector distance while maintaining a fixed field size of 20 x 20 cm^2 at the detector and have been given linear fits.

86
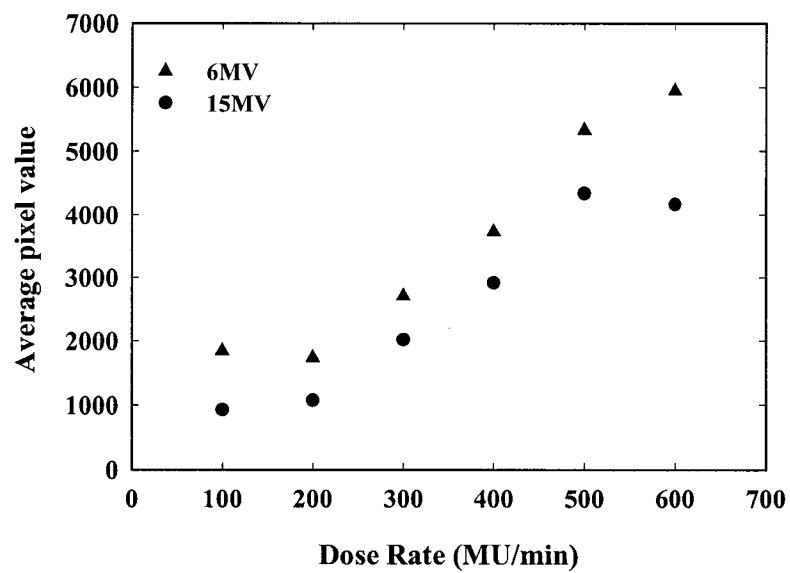
Figure 2.25: Central axis dose-rate response of the aS500 EPID obtained using different beam pulse repetition rates.
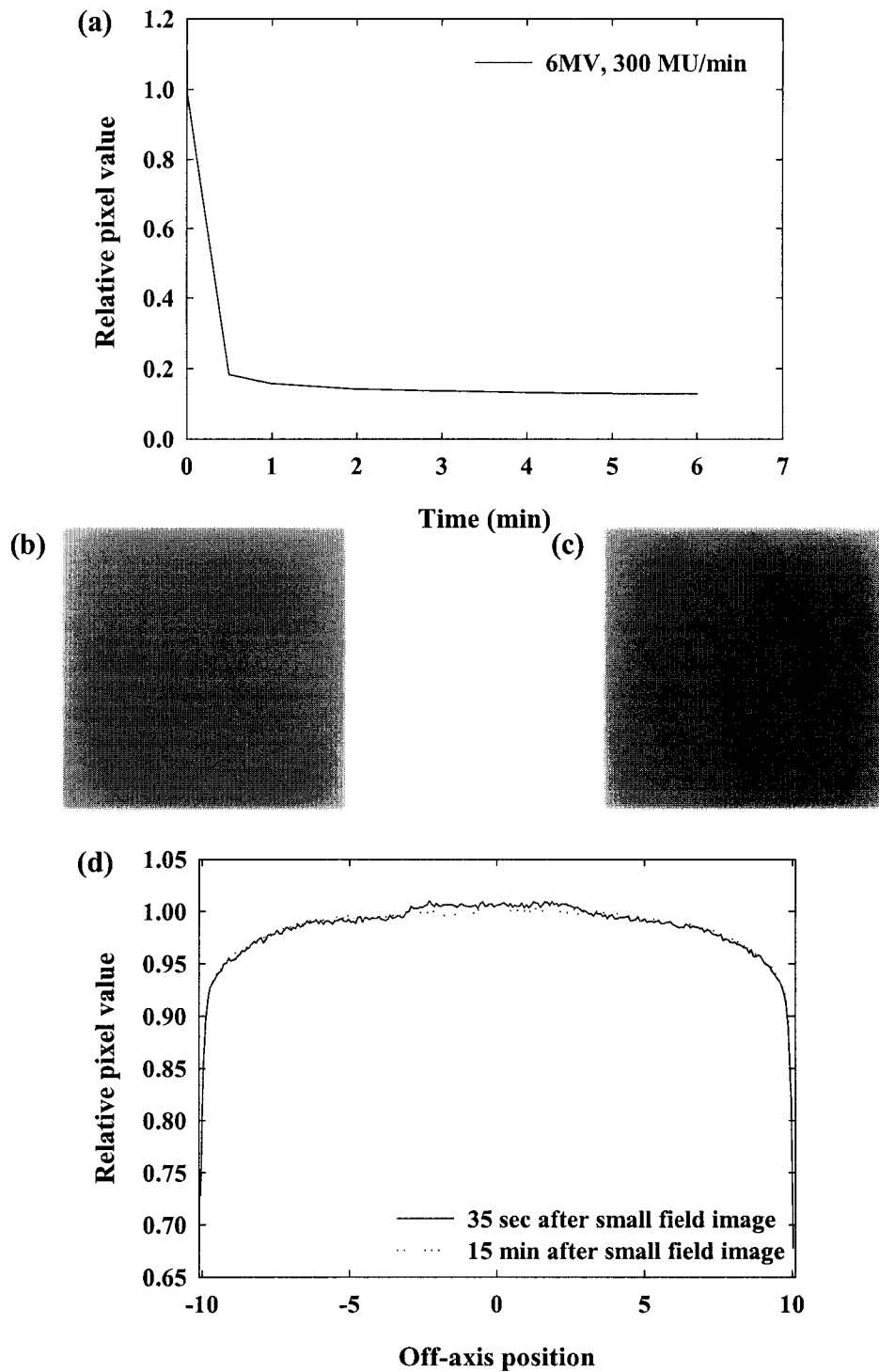
Figure 2.26: (a) Fall-off of drift image mean pixel values with respect to that for an open field image (normalized to 1 for open image). 20 x 20 cm² field images taken (b) 35 sec and (c) 15 min after imaging a 6 x 6 cm² field. (d) Profiles across the images in (b) and (c) (pixel values normalized to mean value in the interval (-5,5) cm).

88

2.7 REFERENCES

[An, 1997]   L. E. Antonuk, Y. El-Mohri, J. H. Siewerdsen, J. Yorkston, W. Huang, and V. E. Scarpine, "Empirical investigation of the signal performance of a high-resolution, indirect detection, active matrix flat-panel imager (AMFPI) for fluoroscopic and radiographic operation," Medical Physics. **24**, 51-70 (1997).

[El, 1999]   Y. El-Mohri, L. E. Antonuk, J. Yorkston, K. –W. Jee, M. Maolinbay, K. L. Lam, and J. H. Siewerdsen, "Relative dosimetry using active matrix flat panel imager (AMFPI) technology," Medical Physics. **26**, 1530-1541 (1999).

[Es, 2001]   A. V. Esch, B. Vanstraelen, J. Verstraete, G. Kutcher, and D. Huyskens, "Pre-treatment dosimetric verification by means of a liquid-filled electronic portal imaging device during dynamic delivery of intensity modulated treatment fields," Radiotherapy and Oncology. **60**, 181-190 (2001).

[In, 1996]   International Electrotechnical Commission, ''Radiotherapy equipment: Coordinates, movements and scales,'' IEC 1217 (1996).

[Ku, 1999]   H. D. Kubo, E. G. Shapiro, and E. J. Seppi, "Potential and role of a prototype amorphous silicon array electronic portal imaging device in breathing synchronized radiotherapy," Medical Physics. **26**, 2410-2414 (1999).

[Mc, 2001]   B. M. C. McCurdy, K. Luchka, and S. Pistorius, "Dosimetric investigation and portal dose image prediction using an amorphous silicon electronic portal imaging device," Medical Physics. **28**, 911-924 (2001).

[Mc, 2004]   L. N. McDermott, R. J. W. Louwe, J.-J. Sonke, M. B. van Herk, and B. J. Mijnheer, "Dose-response and ghosting effects of an amorphous silicon electronic portal imaging device," Medical Physics. **31**, 285-295 (2004).

[Pa, 2002]   M. Partridge, B.-M. Hesse, and L. Muller, "A performance comparison of direct- and indirect-detection flat-panel imagers," Nuclear Instruments and Methods in Physics Research A. **484**, 351–363 (2002).

[Po, 2000a]   PortalVision™ aS500 Rel.6. Reference Manual, Varian Medical Systems Inc., June 2000.

[Po, 2000b]   PortalVision™ aS500 Rel.6. Customer Acceptance Procedure (CAP), Varian Medical Systems Inc., June 2000.

[Po, 2000c]   PortalVision™ aS500 Rel.6. System Verification Summary (SVS), Varian Medical Systems Inc., June 2000.

[Po, 2001]   PortalVision™ aS500 Rel.6. Software Installation Manual, Varian Medical Systems Inc., June 2001.

[Th, 1998]   C. L. Thomason, *Implementation and clinical use of portal imaging,* In: B. B. Mittal, J. A. Purdy, and K. K. Ang, editors. *Advances in Radiation Therapy.* 1st ed. Norwell, MA: Kluwer Academic Publishers; p: 66-99 (1998).

[Ve, 2004]   D. Vetterli, H. Riem, D. M. Aebersold, R. H. Greiner, P. Manser, P. Cossmann, L. Kemmerling, E. J. Born, and R. Mini, "Introduction of a novel dose saving acquisition mode for the PortalVision™ aS500 EPID to facilitate on-line patient setup verification," Medical Physics. **31**, 828-831 (2004).

CHAPTER 3: QUALITY ASSURANCE MEASUREMENTS OF AMORPHOUS SILICON EPID PERFORMANCE

3.1 INTRODUCTION

Routine quality assurance (QA) tests of electronic portal imaging devices are performed periodically to verify the consistency of portal imager operation with time, and to ensure compliance with performance specification limits for key parameters (e.g. mechanical movement, image contrast) established during acceptance testing. Recently, the use of EPIDs has been extended for dosimetry purposes that warrant the need for stability in detector response [An, 2002]. Since the main goal of our research was to employ the a-Si EPID as a dosimetric tool for compensator QC (Chapters 4 and 5), the need for an ongoing study of the operation and stability of the EPID was deemed necessary. To study imaging and dose response stability, we have made use here of a variety of established methods. Dosimetry measurements made with this portal imager are performed by relating measured pixel values to dose as shown in Fig. 2.24. The significance of our QC study is therefore to track the constancy of detector response, both in terms of image quality and dose measurement capability, to ensure reproducible results. This chapter presents the results of monthly QA measurements performed for the Varian aS500 EPID described in Chapter 2 over a period of 18 months, during which time the EPID was deployed on two Varian dual energy linacs to accommodate changing clinical priorities.

3.2 SETUP FOR QA TESTS

The Varian aS500 EPID was attached initially for a period of 11 months to a Varian 23EX linac and then moved to a Varian 2300 CD linac, both of which are dual energy machines delivering 6 and 15 MV photon beams (Varian Medical Systems, Palo Alto, CA). For this study we have used both the 6 and 15 MV photon beams at repetition rates of 100 (allows for maximum read-out time between beam pulses), 300

(well-synchronized with the linac pulses), and 400 (used for our clinical treatments) MU/min, scanned in standard mode where two frames were averaged. For QA purposes, images were obtained at an SED of 140 cm with the gantry positioned at an angle of 0° according to IEC 1217 [In, 1996]. Calibration of all of the available acquisition modes was performed during EPID acceptance testing, and has continued on a monthly basis for the modes selected for study. Each calibration was performed immediately prior to making the QA measurements described in the following section. Since the flood images during the entire period of study showed a variation of only a few percent, the results are not expected to be significantly different for QA measurements performed within one month after flood calibration.

3.3 QA TESTS

The QA tests consisted of measurements of (a) contrast resolution, (b) image quality, specifically modulation transfer, critical frequency, and contrast-to-noise ratio (CNR), and (c) dosimetric quality, specifically DRS stability and central axis pixel response.

3.3.1 Contrast Resolution

Contrast resolution was measured using the procedure described in Section 2.3.2.2.4 using the PV phantom. The average number of holes detected during the course of the study for the six acquisition modes is shown in Table 3.1. The number of holes detected is seen to increase for repetition rates of 300 and 400 MU/min. The counts in a ~1 cm^2 region of interest along the central beam axis were observed to vary approximately in the ratio 1:1.5:2.0 for 6 MV and 1:1.9:2.7 for 15 MV for repetition rates of 100, 300 and 400 MU/min respectively. The increased counts/pixel/frame for the higher repetition rates result in improved contrast. Contrast resolution is observed to decrease with beam energy largely because the total coefficient for Compton interaction in copper decreases from about 4.2×10^{-28} m^2/atom at 2 MeV to 2.4×10^{-28}

92

m^2/atom at 5 MeV [Jo, 1983]. Our results are superior to those reported by Low *et al.* for a liquid ion chamber EPID, where the number of holes detected at a linac repetition rate of 240 MU/min were 12.3 ± 1.2 for 6 MV and 9.0 ± 1.2 for 18 MV [Lo, 1996a]. The main drawback in measuring contrast resolution with the PV phantom is a reliance on subjective visualization of image features.

3.3.2 Image Quality

Image quality was assessed quantitatively using a QC-3V phantom (Department of Physics, Manitoba Cancer Treatment and Research Foundation, Manitoba, Canada) [Ra, 1996]. The rectangular phantom has dimensions of 13.5 x 11.3 x 3.6 cm^3 and incorporates an aluminum and an acrylic slab, each of thickness 1.8 cm, bonded together. The aluminum slab contains five sets of high contrast rectangular bars made of lead and Delrin plastic having spatial frequencies of 0.1, 0.2, 0.25, 0.4, and 0.75 line pairs per mm (lp/mm). The central three bar patterns are surrounded by six uniform regions of lead, aluminum and plastic of different thicknesses (Fig. 3.1(a)). For imaging, the phantom was placed at linac isocenter at an angle of 45° with respect to the long axis of the treatment couch to prevent spatial aliasing. Two images were acquired in succession for each acquisition mode and imported for analysis into the PIPS software (PIPSpro 3.2, Masthead Imaging Corporation, Nanaimo, Canada) that determined the relative modulation transfer function, contrast-to-noise ratio, and noise level [Ra, 1996].

3.3.2.1 Relative modulation transfer function (RMTF)

Modulation transfer function (MTF) is the ratio of output to input modulation at different spatial frequencies for an imaging system. RMTF is a renormalized version of MTF obtained by taking the ratio of the modulation transfer for a particular spatial frequency, MTF(f), to that of the lowest frequency measured, MTF(f_1), where $f_1 = 0.1$ lp/mm for the QC-3V phantom.

93

$$RMTF(f) = \frac{MTF(f)}{MTF(f_1)}.$$ (3.1)

For a bar pattern, since the output modulation is sinusoidal, the modulation transfer is proportional to the variance measured in a region of interest placed within the image of the bar pattern (Fig. 3.1(b)), as described by Droege and Rajapakshe [Dr, 1983; Ra, 1996]. The RMTF data was used to determine the critical frequency.

3.3.2.2 Critical frequency (f_{50})

The critical frequency is a measure of spatial resolution corresponding to 50% relative modulation transfer. The value of the critical frequency for a particular acquisition mode is obtained by piecewise linear interpolation of the RMTF data to locate the 50% relative frequency response (Fig. 3.2). f_{50} values were found not to depend on linac repetition rates; averages obtained over the three repetition rates studied were 0.435 ± 0.005 lp/mm for 6 MV and 0.382 ± 0.003 lp/mm for 15 MV. Spatial resolution is reduced for the 15 MV beam because of increased lateral spreading of the higher energy primary electrons which broadens the beam penumbra [Mu, 1990b] and increased transmission of the high energy photons through the bar patterns [Ra, 1996].

Our f_{50} values are slightly better in comparison to those reported by Luchka for an aS500 EPID: 0.391 lp/mm for 6 MV and 0.338 lp/mm for 18 MV [Lu, 2001]. The difference at 6 MV may be attributable to a difference in phosphor thickness. Our EPID incorporates a gadolinium oxysulfide screen that is 133 mg/cm^2 thick while Luchka's is 70 mg/cm^2 thick [Gr, 2002]. Bissonnette *et al.* have shown that for an a-Si imager, the thicker screen (Lanex Fast) improves the x-ray detection probability and optical gain and therefore the image quality at low spatial frequencies [Bi, 1997]. By comparison, previously reported SLIC EPID data from our institution yielded f_{50} = 0.33 ± 0.04 lp/mm for 6 MV and $f_{50} = 0.28 \pm 0.01$ lp/mm for 15 MV [Ki, 1998]. This is a considerable reduction in resolution in comparison to the a-Si EPID. The extent of the difference can be seen in Fig. 3.3, which depicts images of the head of a Rando

phantom taken with both types of EPID. The f_{50} values for our aS500 EPID remained quite steady over the measurement period (Fig. 3.4).

3.3.2.3 Contrast-to-noise ratio (CNR)

Image quality becomes poorer with decreasing contrast and increasing noise. To quantify this behavior, we make use of the contrast-to-noise ratio,

$$CNR = \frac{P_b - P_d}{\sigma},$$ (3.2)

where P_b and P_d are average pixel values in the brightest (least irradiated) and darkest (most irradiated) regions of interest (ROIs) obtained from the uniform regions of the QC-3V phantom [Ra, 1996]. σ is the random image noise calculated as the average of pixel value standard deviations from the six uniform regions.

Figure 3.5 shows the trend of the CNR data; average values for the entire study period are shown in Table 3.2. The CNR is seen to increase with repetition rate and to decrease with beam energy. With increasing repetition rate, the difference in pixel values of the brightest and darkest regions increased (the random noise remained approximately constant), thereby increasing the CNR value. This increased difference arises because of a corresponding increase in counts/pixel/frame with repetition rate for both beam energies. Our previously reported SLIC EPID data for CNR obtained at 400 MU/min were 131.6 ± 11.2 and 93.7 ± 14.6 for 6 and 15 MV, respectively [Ki, 1998]. The amorphous silicon EPID thus has a significantly better CNR than the SLIC EPID.

3.3.3 Dosimetric Quality

3.3.3.1 Dose rate servo (DRS) stability

The DRS stability test is intended to assess MU/beam pulse constancy for sequential beam pulses forming an image frame (Sec. 2.3.2.2.1). DRS stability was determined for test images obtained during the calibration process. According to the

manufacturer, during the time taken for image acquisition the DRS stability should not exceed 3% [Po, 2002c]. Table 3.3 displays the DRS stability determined for the various acquisition modes, averaged over the study period. At both beam energies the results are within specification. Our data reveal greater instability for the higher energy beam, which may be due to greater beam pulse variability at the lower linac base frequency of 180 Hz (15 MV beam) relative to the higher base frequency of 360 Hz (6 MV beam).

3.3.3.2 Central axis pixel response

Pixel response is measured to determine how reproducible pixel values are for identical beam deliveries over an extended time period. Any variation in EPID operation for fixed parameter settings could result in changes in image pixel values. The detector response was monitored using calibration test images obtained over the 7-month period when the EPID was attached to a Clinac 2300CD linac. Since this measurement is influenced by output fluctuations of the linac, a reference reading was taken at the time of calibration using a PR-06 Farmer ion chamber (Capintec Instruments Inc, Pittsburg, PA) connected to a Capintec electrometer (Model # 192). The chamber was placed in a QA jig that fit into the linac block tray and irradiated using a collimator setting of 10 x 10 cm^2 to 50 MU. The pixel response was then calculated as the ratio of the average pixel value in a 13 x 13 pixel ROI (~1 cm^2) in the center of the image to the temperature and pressure corrected ion chamber reading.

A 1% change in the CAX pixel response was observed for the 6 MV beam during the period of investigation, and a 4% change for the 15 MV beam (Fig. 3.6). There appears to be a relatively modest downward trend in the data at both energies, which bears further observation. This finding points to the need for regular dose response calibration of the EPID when used in dosimetry applications.

3.4 CONCLUSIONS

This chapter reports the results of a longitudinal QA study performed on a Varian aS500 EPID. Measurements included the contrast resolution (qualitative), image quality (quantitative), DRS stability and central axis pixel response. The contrast resolution studies were performed by observing the number of holes visible in a contrast-detail phantom. We did not observe any dramatic change with time in contrast resolution, which was superior to that reported earlier by our center for a SLIC EPID. The QC-3V phantom was used to determine the critical frequency and contrast-to-noise ratio for six different image acquisition modes. It was observed that the critical frequencies were independent of linac repetition rate and remained constant at 0.435 ± 0.005 lp/mm at 6 MV and 0.382 ± 0.003 lp/mm at 15 MV, values which are significantly better than those obtained for our SLIC EPID. The CNR measurements yielded better contrast values with increasing repetition rates because of the increase in counts/pixel/frame. The f_{50} and CNR values were found to be better when imaging with the 6 MV beam because of the enhanced response of the detector to lower energy photons. At 15 MV, the electrons created by Compton interactions travel a greater distance laterally, causing a greater spread of light photons in the phosphor screen and thereby reducing image quality. The DRS stability of the EPID was found to be better for the 6 MV beam. The central axis pixel response remained within 1% for the 6 MV beam over a 7-month period, suggesting that when the EPID is used in dosimetry applications, dose-to-pixel response calibration curves can be verified at extended intervals. For the 15 MV beam, for which we observed a 4% variation over the same period, calibration curves may need to be checked more frequently.

Our set of QA measurements confirms the overall performance superiority of the amorphous silicon EPID in comparison to the SLIC EPID. Performing the measurements using different image acquisition modes provides insight into the appropriate selection of EPID operating parameters for imaging and dosimetry applications.

97

Table 3.1

Average number of holes detected with the contrast detail phantom for the different acquisition modes over the period of QA measurement.

Energy (MV)	Number of holes detected (±SD)		
	100 MU/min	300 MU/min	400 MU/min
6	13.7 ± 1.9	16.9 ± 0.9	15.7 ± 1.1
15	10.1 ± 1.5	13.6 ± 1.5	13.5 ± 1.5

Table 3.2

The contrast-to-noise ratio for our aS500 EPID, averaged for each acquisition mode over the period of QA measurement.

	Mean CNR (±SD)		
	100 MU/min	300 MU/min	400 MU/min
6	80.4 ± 8.0	165.2 ± 13.8	201.9 ± 18.0
15	57.6 ± 6.5	136.8 ± 10.7	164.1 ± 13.1

Table 3.3

The dose rate servo stability for each acquisition mode, averaged over the period of QA measurement.

	DRS Stability (%)		
	100 MU/min	300 MU/min	400 MU/min
6	0.9 ± 0.3	0.7 ± 0.4	0.9 ± 0.3
15	1.8 ± 0.9	1.3 ± 0.7	1.3 ± 0.8
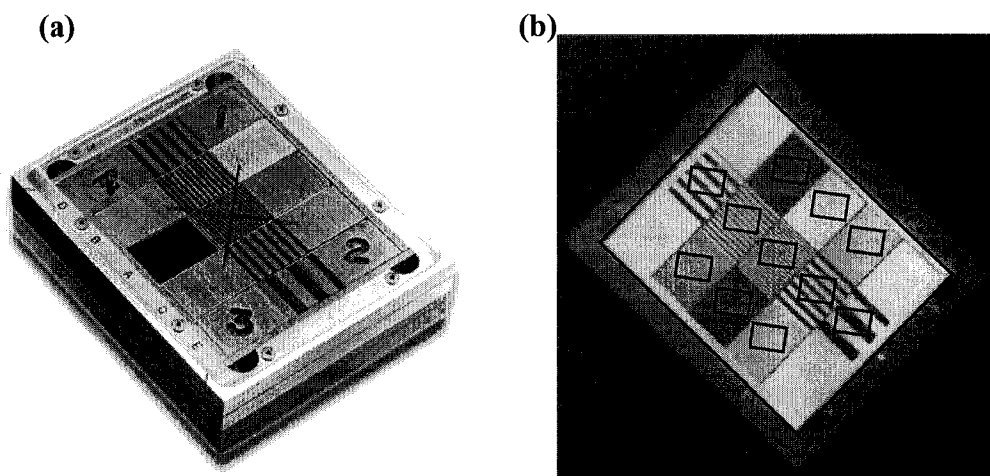
Figure 3.1: **(a)** The QC-3V phantom. **(b)** Portal image of the QC-3V phantom [6 MV, 300 MU/min, standard scan] showing the analysis regions of interest for the bar pattern and uniform insert areas.
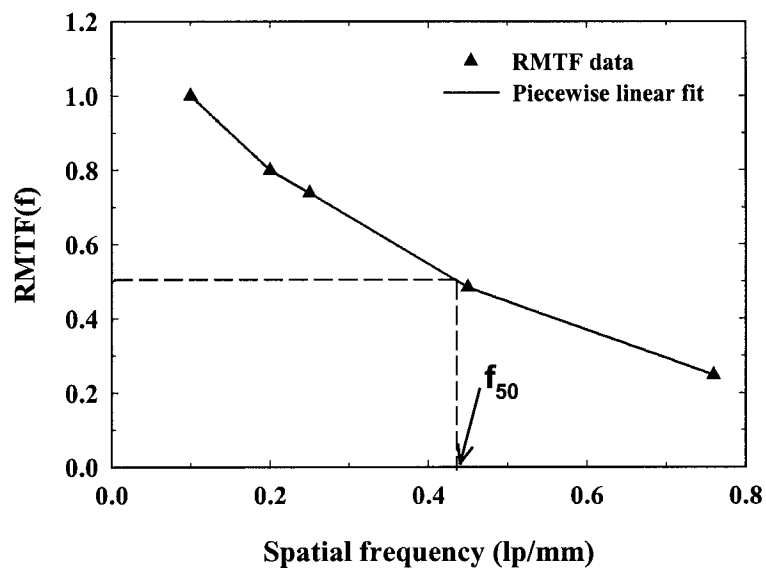
Figure 3.2: RMTF curve for a [6 MV, 300 MU/min, standard scan] acquisition showing the critical frequency, f_{50}. A piecewise linear fit is given to the RMTF data.

100

(a) (b)
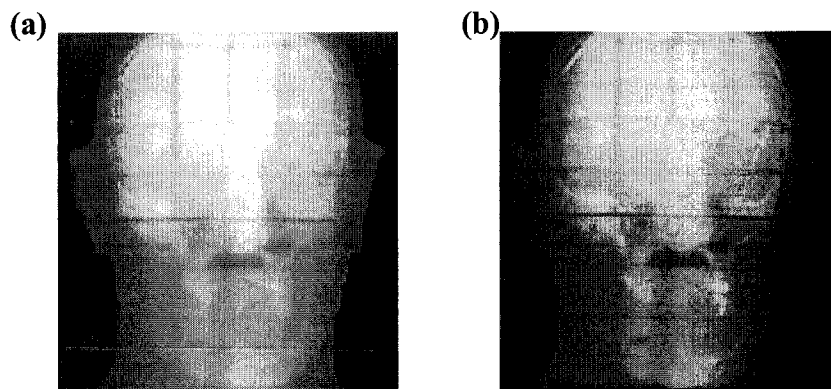
Figure 3.3: Images of the head of a Rando phantom taken with our **(a)** SLIC and **(b)** a-Si EPID using a [6 MV, 300 MU/min, standard scan] acquisition mode, after histogram equalization. The horizontal lines are boundaries between the slabs making up the phantom.

101
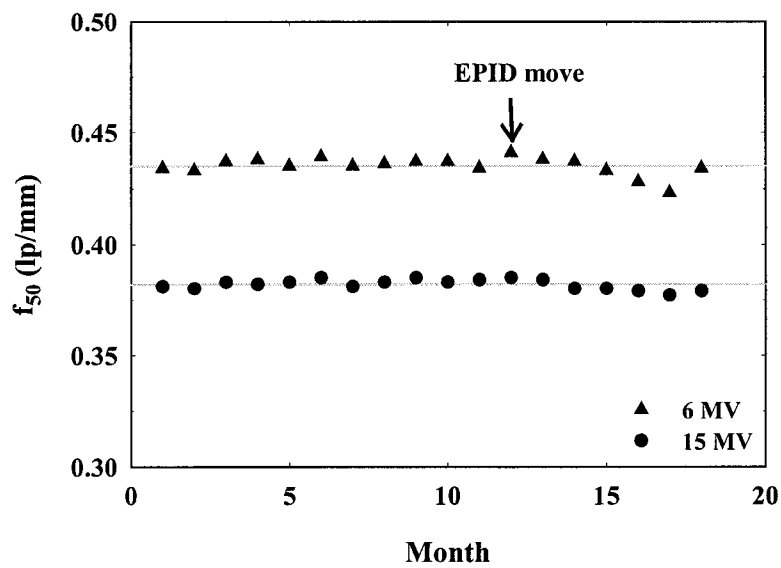
Figure 3.4: Measured values (averaged over repetition rate) of critical frequency for both beam energies over the 18 month study period. The f_{50} values remained consistent even after the EPID move to another linac. The horizontal lines are drawn across the average values.

102
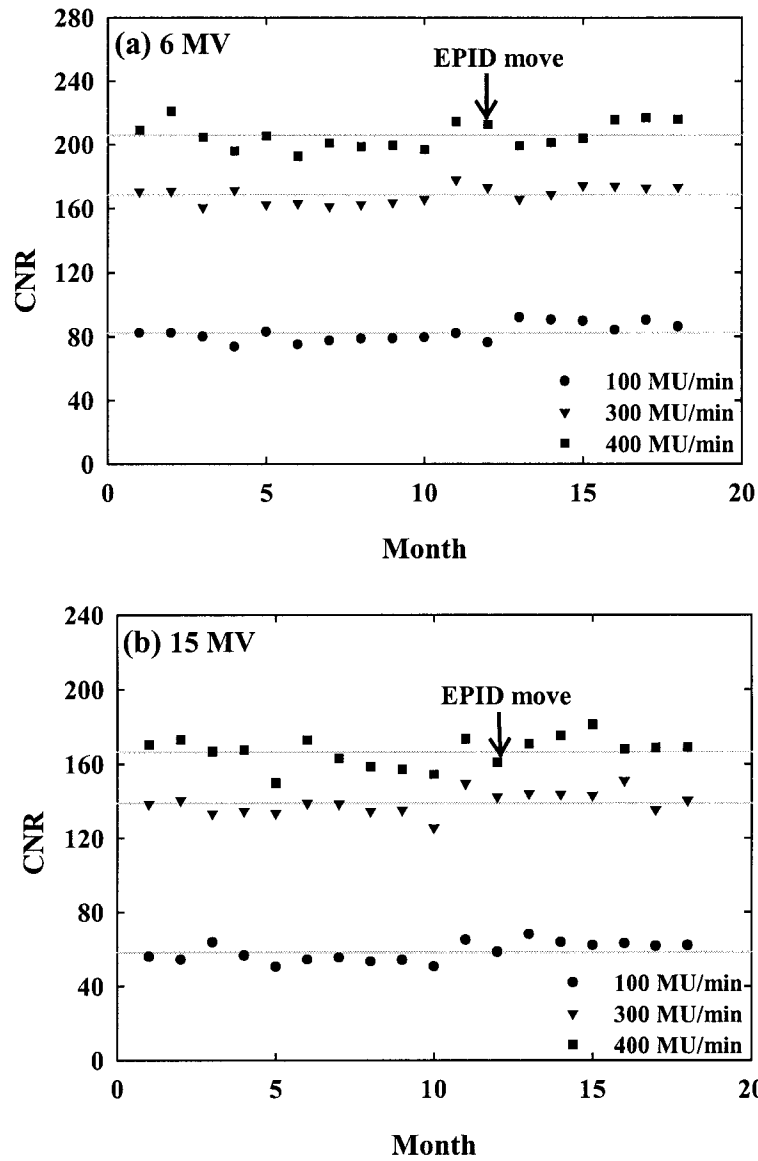
Figure 3.5: CNR values determined over the 18 month study period for **(a)** 6 MV and **(b)** 15 MV photon beams. The CNR values show very little change after the EPID move from one linac to another.

103
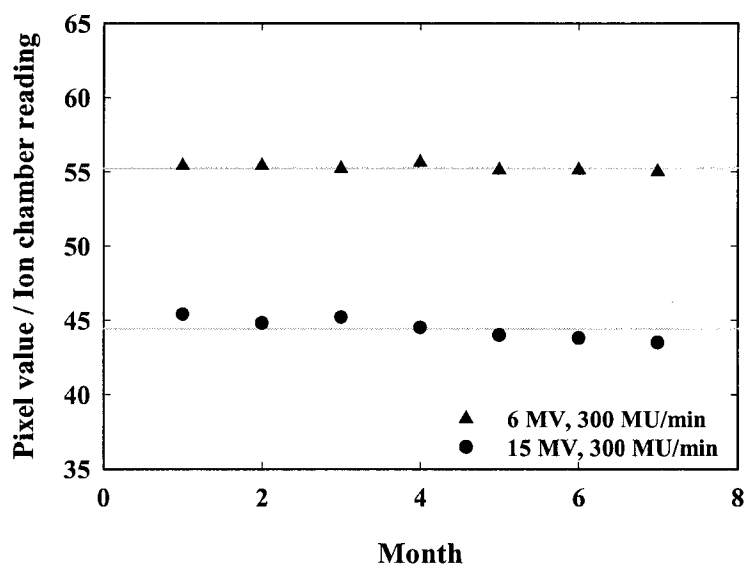
Figure 3.6: Plot shows the central axis pixel response of the EPID for 6 and 15 MV at 300 MU/min for the last 7 months of the study.

104

3.5 REFERENCES

[An, 2002] L. Antonuk, "Electronic portal imaging devices: a review and historical perspective of contemporary technologies and research," Physics in Medicine and Biology. **47**, R31-R65 (2002).

[Bi, 1997] J-P. Bissonnette, I. A. Cunningham, and P. Munro, "Optimal phosphor thickness for portal imaging," Medical Physics. **24**, 803-814 (1997).

[Dr, 1983] R. T Droege, "A practical method to routinely monitor resolution in digital images," Medical Physics. **10**, 37-43 (1983).

[Gr, 2002] E. E. Grein, R. Lee, and K. Luchka, "An investigation of a new amorphous silicon electronic portal imaging device for transit dosimetry," Medical Physics. **29**, 2262-2268 (2002).

[In, 1996] International Electrotechnical Commission, "Radiotherapy equipment: Coordinates, movements and scales," IEC 1217 (1996).

[Jo, 1983] H. E. Johns and J. R. Cunningham, *"The physics of radiology,"* 4th ed. Charles C Thomas Publisher, Springfield, Illinois (1983).

[Ki, 1998] H. J. Kim and R. S. Sloboda, "Image quality assurance for a Varian PortalVision™ EPID," 5th International Workshop on Electronic Portal Imaging, Phoenix, AZ. Proceedings p: 95-96, (1998).

[Lo, 1996a] D. A. Low, E. E. Klein, D. K. Maad, W. E. Umflet, and J. A. Purdy, "Commissioning and periodic quality assurance of a clinical electronic portal imaging device," International Journal of Radiation Oncology Biology Physics. **34**, 117-123 (1996).

[Lu, 2001] K. Luchka, Letter to the editor. PIPS News. **4**, 3 (2001).

[Mu, 1990b] P Munro, J. A. Rawlinson, and A. Fenster, "Therapy imaging: A signal-to-noise analysis of a fluoroscopic imaging system for radiotherapy localization," Medical Physics. **17**, 763-772 (1990).

[Po, 2000c] PortalVision™ aS500 Rel.6. System Verification Summary, Varian Medical Systems Inc., June 2000.

[Ra, 1996]   R. Rajapakshe, K. Luchka, and S. Shalev, "A quality control test tool for electronic portal imaging devices," Medical Physics. 23, 1237-1244 (1996).

CHAPTER 4: COMPENSATOR QUALITY CONTROL WITH AN AMORPHOUS SILICON EPID

4.1 INTRODUCTION

In conventional radiotherapy, beam modulation is achieved by means of wedges and custom compensators. Custom-made compensators are used in radiotherapy to compensate for missing tissue, to modify the dose distribution in the patient, and as a means for delivering intensity modulated radiotherapy (IMRT) by removing some of the incident photons from the externally applied treatment beam [El, 1959; Bo, 1982; Re, 2000]. They can be made using a variety of materials and fabrication methods [Va, 1995; We, 1988]. Because the compensators are custom-made, their beam-modifying properties must be verified before clinical use. It is therefore important to establish quality control (QC) procedures for all compensators [Fr, 1998; Ku, 1994; Ma, 1980; Ba, 1998]. Conventional methods of compensator QC involve ion chamber or film measurements of the energy fluence transmitted through the compensator. QC invariably includes a measurement of the compensator factor (CF), which is the ratio of energy fluences for a compensated to an open field on the central beam axis (CAX) [Jo, 1988]. The factor is commonly obtained from ion chamber (IC) measurements in a tissue equivalent phantom, which are easily obtained on the CAX. However the IC method can become onerous if several off-axis measurements are also desired. Likewise, the use of verification film in a phantom involves setup, processing, readout, and calibration. Several publications recommend the use of an EPID as a solution to this problem [Ro, 1995; Lo, 1996b; Pa, 1999]. The advantage of using an EPID for compensator QC is that once it has been calibrated for dosimetry, only two images are required – one with and one without the compensator in place – to determine the compensator factor and the relative energy fluence matrix at any number of off-axis points in the measurement plane. Therefore, EPID-based compensator QC should be more comprehensive and quicker to perform.

107

Roback *et al.* were among the first researchers to employ a SLIC EPID for the purpose of designing and verifying compensating filters [Ro, 1995]. After studying the EPID response, they measured attenuation curves for several phantom materials and used them to design, build, and test a number of missing tissue compensators. Their entire process was validated by ion chamber measurements, which confirmed that transmitted energy fluence with a compensator and patient phantom in place was spatially uniform to within 3%. Low *et al.* verified compensating filters by comparing the transmitted and scattered fluence measured using a SLIC EPID to the fluence calculated using the intended filter shape via convolution with a distributed source kernel [Lo, 1996b]. Agreement was found to be < 3%. Pasma *et al.* used a fluoroscopic EPID for compensator thickness verification by measuring transmission and relating the primary component of transmission to thickness, with an accuracy of about 0.5 mm [Pa, 1999].

The a-Si EPID described in Chapter 2 was used for the work reported here, the purpose of which was to investigate the feasibility of using this EPID as an ion chamber replacement in an existing compensator calibration and quality control protocol.

4.2   MATERIALS AND METHODS

4.2.1   Materials and Set-up

4.2.1.1 EPID set-up

The Varian PortalVision aS500 EPID [Po, 2000a] mounted on a well-tuned dual energy Varian 2300CD linac via a retractable arm was used for the measurements (Fig. 4.1), which were made exclusively with a 6 MV beam having a depth of dose maximum at 1.5 cm. A 0.5 cm slab of solid water was placed on the detector cover (Fig. 4.2) to provide electronic equilibrium (Sec. 2.5.3). Table 4.1 displays the parameter values chosen for this work after preliminary experimentation described in Chapter 2. As indicated, all experiments were performed with the linac operating at a

108

pulse repetition rate of 300 MU/min. The EPID was set up to acquire images in standard mode, which involved averaging two image frames.

The output of the linac used for our measurements is monitored daily and maintained within ± 1%. The symmetry of the beam is measured on a monthly basis and maintained within ± 2%. During the period of this study it was observed that the maximum asymmetry was ~1.5% (region Q4 of Fig. 4.3). Calibration of the EPID is performed on a monthly basis for each operating mode by acquiring dark and flood field images that are used to correct subsequent images (Sec. 2.2.3). Since the response of an a-Si detector can possibly drift over time, the central axis response of the aS500 was monitored at monthly intervals during the study. As a measure of stability, (Sec. 3.3.3.2, the average pixel value in a ~1 cm^2 area in the center of an open field image obtained with a collimator setting of 28.6 × 21.4 cm^2 at a detector distance of 140 cm (sensitive area fully irradiated) was divided by the corresponding linac output measurements made with an ion chamber. The central axis response of our aS500 was found to vary by < 0.4% (1 SD), indicating good system stability [Me, 2004].

4.2.1.2 Compensator design and manufacture

In our institution, compensator shape is determined either from patient contour data obtained using a Huestis digitizer (Huestis Machine Corporation, Bristol, RI) or from a modulation matrix produced by a Helax treatment planning system (Nucletron, Kanata, ON) using CT data. Intended thicknesses are subsequently calculated on a two-dimensional grid with an in-house Excel spreadsheet Visual Basic Application (VBA) program, taking into consideration the beam divergence. Compensators are then constructed from 5 cm thick Styrofoam slabs, milled using a TS-5000 Huestis Compu•former (Huestis Machine Corporation, Bristol, RI). The construction method is based on the design described by van Santvoort [Va, 1995]. The milled depths at 5 positions corresponding to the central axis (CAX = {x' = 0, y' = 0}) and four off-axis positions (OAX = {x' = ± 2.5 cm, y' = ± 2.5 cm} in the isocentric plane) are measured for comparison with intended depths using a caliper (Figs. 4.2 and 4.3). Figure 4.1 also

109

illustrates the coordinate conventions, adapted from IEC 1217 [In, 1996]. A 0.6 cm thick Lucite tray placed on either side contains the steel, provides rigidity, and enables placement in the linac accessory mount. The mould is closely packed with cast steel shot (#J-827, Ervin Industries, Butler, PA) of diameter ranging from 0.5 to 0.9 mm. The steel shot density was calculated by determining the weight of different amounts of the material using a digital balance and the corresponding volume using a graduated beaker (Table 4.2). From three such measurements, the density was determined to be 4.69 ± 0.05 g/cc.

4.2.2 Clinical Compensator QC Method

In our center, compensator QC involves ion chamber measurements made at isocenter at a depth of 5 cm in a polystyrene phantom of: (i) the CF on the CAX {x′,y′ = 0, 0}, and (ii) four off-axis fluence ratios (OFRs) at {x′,y′ = ±2.5, ±2.5 cm}, with and without the compensator in place (Fig. 4.4). The required measurements are currently performed with a PR-06C Farmer chamber (Capintec Instruments Inc, Pittsburg, PA) connected to a Capintec electrometer (Model # 192). The measured CF and OFRs are compared with values calculated by the VBA program. In the present work these measurements are referred to as the clinical QA method.

4.2.3 EPID Measurements: General Approach and Preliminary Work

A common approach to using an EPID as a dosimeter, which was adopted in this work, is to relate the EPID pixel response to the energy fluence measured by an ion chamber in air at the EPID location via a calibration curve. Because of the anticipated spectral dependence of the aS500 response arising from an integral high-Z phosphor screen, calibration curves were obtained for open and compensated fields separately. Since the EPID is not water equivalent, it is impractical to assume it to be a full or mini phantom as far as scattering properties are concerned. Chang *et al.* have shown that SLIC EPID scatter factors can be measured and related to those of standard phantoms [Ch, 2001]. Using Chang's approach, scatter factors for the aS500 EPID were

110

experimentally determined for a range of field sizes and incorporated in the energy fluence measurement formalism. The position of the central axis in the EPID image was located each time the EPID was deployed using a radiation field edge analysis technique to minimize geometric uncertainty stemming from detector set-up variability.

To evaluate the technique, compensator measurements performed with the a-Si EPID were compared to ion chamber readings taken in air, and to the clinical QA method. Comparative measurements were performed using a Farmer ion chamber. For in-air measurements, a water-equivalent buildup cap of 1.5 cm thickness was placed around the Farmer chamber. EPID image processing and associated calculations were done using Matlab 5.3 (The Mathworks Inc, Nattick, MA).

The geometrical configuration for compensator measurements is shown schematically in Figure 4.2. The distance from the x-ray source to the top of the EPID detector stack, designated the source-to-EPID distance (SED), is the distance displayed on the hand-held controller when the EPID is deployed. SEDs of both 105 cm and 140 cm were studied because although most of the clinical compensators can be measured at 140 cm, occasionally a larger one may require a smaller SED. The source to detector distance (SDD) is defined here as the distance from the x-ray source to the image-forming layer of the EPID. Since the latter is located approximately 1.3 cm below the top of the detector stack, SDD = SED + 1.3 cm (see Sec 2.2.1). By convention, all field sizes are defined at linac isocenter, i.e. at a source to axis distance (SAD) of 100 cm, unless otherwise indicated.

According to the manufacturer, the aS500 can be deployed to a specified working position with an accuracy of $\pm$ 0.3 cm (~4 pixels) in the imaging plane. For compensator QC, the location of the CAX on an EPID image needs to be determined with better accuracy. To do so, field edges corresponding to positions where pixel values fall to 50% of their maximum value were identified (Fig. 4.5), and then the CAX was located. In a series of six measurements made on consecutive days, a maximum difference in CAX position of 0.4 cm was observed along the Y direction, and 0.2 cm along the X direction. For compensator measurements, a CAX localization

111

image was taken after each EPID deployment. The CAX position was translated to the nearest pixel corner, and a symmetric 10 × 10-pixel measurement region of interest ($ROI_{CAX} \approx 0.8 \times 0.8$ cm^2) defined around it (Fig. 4.6). Off-axis 10 × 10 pixel measurement ROIs were then defined with respect to the CAX. EPID pixel values were averaged over these ROIs to reduce measurement fluctuations.

Image pixel values were observed to depend, in a discrete way, on the time of image acquisition. For unknown reasons there were occasional, random instances when images were acquired 2 sec prior to the midpoint of an irradiation (a 0-50%-0 imaging sequence was used, see Table 4.1). These premature images yielded pixel values that were ~4% lower than those in correctly timed images taken with the same setup parameters. Consequently, the premature images were identified on the basis of their recorded acquisition time and discarded.

To verify consistency in placement of a compensator in the accessory mount, measurements were made with a fiducial tray having a cross wire at its center. The shadow of the cross wire was compared with the light field center at isocenter when the tray was repeatedly inserted in the accessory mount. An average shift of < 0.5 mm was observed. To eliminate the effect of such shifts, portal images were taken immediately following the corresponding ion chamber readings without moving the compensator.

Furthermore to determine the effect of any backscatter from the floor when positioning the detector at the extended distance of 140 cm, ion chamber measurements were made for various field sizes with the gantry at 0° (vertical) and 270° (horizontal). It was observed that the readings in both positions agreed to < 0.1%, suggesting that backscatter from the floor to the detector is not significant at 140 cm.

4.2.4   EPID Compensator QC Method

4.2.4.1 Compensator measurements

The compensator factor can be written as

$$CF = \frac{R^{comp}(AxB, x_0, y_0)}{R^{open}(AxB, x_0, y_0)},$$ (4.1)

where $R^{comp}(AxB, x_0, y_0)$ and $R^{open}(AxB, x_0, y_0)$ are energy fluence readings at SDD along the CAX for a collimator setting A x B measured using an ion chamber (or EPID) in the presence and absence of the compensator, respectively.

In clinical dosimetry, the reading in a phantom can be related to the reading in air on the CAX at the same location [Kh, 1994] by

$$R(phantom, AxB, x_0, y_0, d) = R(air, AxB, x_0, y_0) \times S_p(AxB, x_0, y_0, d),$$ (4.2)

where $S_p(AxB, x_0, y_0, d)$ is the phantom scatter factor for collimator setting A x B for measurements done at SDD at a depth d. Applying Eq. 4.2 to our work, we can relate the average EPID pixel reading in a region of interest at the depth of dose maximum, d_{max}, to an ion chamber reading in air as

$$R(EPID, AxB, x_0, y_0) = f(P(x_0, y_0)) \times S_{EPID}(AxB, x_0, y_0),$$ (4.3)

where $R(EPID, AxB, x_0, y_0)$ is the inferred EPID fluence reading at d_{max} along the CAX at SDD for a collimator setting A x B and $f(P(x_0, y_0))$ is a calibration curve relating the mean pixel value P from the ROI to the ion chamber reading in air at the same SDD for a fixed calibration field size. $S_{EPID}(AxB, x_0, y_0)$ is the EPID scatter factor for depth d_{max} that takes into account how the scatter varies with field size. Hence we can infer the reading that would be measured by an ion chamber at SDD if we know the mean EPID pixel value P, by using Eq. 4.3. Determination of the EPID calibration curve and the EPID scatter factor are described in the following two sections.

4.2.4.2 EPID calibration curve

The response of an a-Si EPID is linear with energy fluence for open fields [El, 1999 and Fig. 2.24], in contrast to the square root response of a SLIC EPID [Pa, 1998a]. The calibration curve relates the EPID pixel response to the energy fluence measured by an ion chamber in air. Calibration measurements were performed for a reference field size of 20 x 20 cm^2 at the detector for open fields at SEDs from 105 to

160 cm, and also for attenuated fields at SEDs of 105 and 140 cm. The two sets of calibration curves were made because of the observed sensitivity of the aS500 EPID to the incident photon spectrum, which is altered by material in the beam path. The calibration curve for the attenuated beam was originally made with sheets of lead (thicknesses ranging between 0.165 and 4.795 cm) and then also with different thicknesses of steel shot granules. For the latter, attenuators were made by filling Styrofoam slabs with steel shot to depths of 0.5 to 4 cm in steps of 0.5 cm, and by combining the 3 and 4 cm thick slabs to obtain a maximum thickness of 7 cm. Measurement with the 7 cm thickness was made to determine the behavior of the calibration curve at smaller energy fluences. Customarily in the clinic the maximum CAX thickness encountered is 4.5 cm. EPID pixel values were averaged over the ROI_{CAX} encompassing the central beam axis for three sequentially acquired images. Corresponding fluence measurements were made with the ion chamber in the buildup cap positioned at the same SDD (Fig. 4.7). To minimize the effect of linac output variations on subsequent measurements, the ion chamber reading is expressed in terms of a ratio of readings, in relative units (RU) [Ch, 2001],

$$\Re\left(air,(20x20)_{SDD}\right)= \frac{R\left(air,(20x20)_{SDD}\right)}{R\left(air,(10x10)_{SAD}\right)} \text{ [RU]}, \tag{4.4}$$

where $R(air,(20x20)_{SDD})$ and $R(air,(10x10)_{SAD})$ are ion chamber readings for a fixed calibration field size of 20 x 20 cm^2 at the EPID SDD and a reference field size of 10 x 10 cm^2 at SAD, respectively, obtained at the time of calibration.

A graph relating the mean pixel value in the ROI_{CAX} to $\Re\left(air,(20x20)_{SDD}\right)$ obtained at different SEDs, or with different amounts of attenuating material in the beam path constitutes a raw calibration curve. The formula for calculating the energy fluence reading at the EPID is the same for the open field and attenuated field calibration curves. As $\Re\left(air,(20x20)_{SDD}\right)$ is a fluence ratio, the energy fluence reading at the EPID is obtained by multiplying it by the temperature- and pressure-corrected reference ion chamber reading $R^D\left(10x10,SAD\right)$ obtained on the day of the compensator measurement,

114

$$R\left(EPID, (20x20)_{SDD}\right) = \Re\left(air, (20x20)_{SDD}\right) \times R^{D}\left(air, (10x10)_{SAD}\right). \qquad \textbf{(4.5)}$$

To use the calibration curves for field sizes other than 20 x 20 cm^2, they have to be corrected using the EPID scatter factor.

4.2.4.3 EPID scatter factors

Determination of the scatter factor for a tissue equivalent phantom as defined in Eq. 4.2 is straightforward, but is more complicated for an EPID comprised of non-tissue equivalent materials. A method to determine scatter factors for a SLIC EPID was described by Chang *et al.* using an iterative algorithm [Ch, 2001]. This same algorithm has been applied to the a-Si EPID. Accordingly, the EPID scatter factor is represented as a ratio of the EPID energy fluence for an arbitrary radiation field of interest to that for a 10 x 10 cm^2 reference field at SDD, divided by a ratio of collimator scatter factors (S_c) for the same collimator settings. From Eq. 4.2

$$S_{EPID}\left(AxB, x_0, y_0\right) = \frac{R\left(EPID, AxB, x_0, y_0\right)/S_c\left(AxB, x_0, y_0\right)}{R\left(EPID, 10x10, x_0, y_0\right)/S_c\left(10x10, x_0, y_0\right)}. \qquad \textbf{(4.6)}$$

The inputs for the iterative process are the raw calibration curve and the mean EPID pixel values from ROI$_{CAX}$ for different field sizes. The EPID scatter factor is initially assigned a value of unity as shown in the flow chart in Fig. 4.8. The raw calibration curve is updated using Eq. 4.3 and fit with an appropriate polynomial form. Using the fitted function, the mean pixel values for the different field sizes are converted to energy fluence values at the EPID. A new set of EPID scatter factors is then determined using Eq. 4.6 and normalized to 1 for a 10 x 10 cm^2 field at the EPID. If the difference between the old and new scatter factors is within a set tolerance for the largest field size, the iteration is terminated (a tolerance of 0.1% was used for this work). Otherwise the new scatter factors are used to update the calibration curve, and the iterative process continues until tolerance is achieved. The outputs of the iterative procedure are a calibration curve for a 10 x 10 cm^2 field at the EPID, and a consistent set of scatter factors for other field sizes.

115

EPID scatter factors for the aS500 were measured separately for open and attenuated fields (Fig. 4.9), for collimator settings ranging from 5.6 x 5.6 to 23.5 x 23.5 cm^2 at an SED of 105 cm, and from 4.2 x 4.2 to 17.7 x 17.7 cm^2 at an SED of 140 cm. As the EPID response is altered in the presence of an attenuator, scatter factors were measured separately for each different thickness of steel shot used to make the calibration curve. All EPID scatter factors were stored in a database for use in clinical QA measurements. For each absorber thickness, the change in the calibration curve due to the change in EPID scatter was also tabulated.

For clinical dosimetry purposes, measurements of the collimator scatter factor are normally performed at linac isocenter. It is understood that scatter from the flattening filter and primary collimator, and backscatter to the monitor chamber, are major causes of collimator scatter factor variation with field size [Ch, 1994; Yu, 1996]. However the values of the collimator scatter factor can change as the detector is moved away from isocenter. For instance, the contribution from flattening filter scatter will decrease as the source to detector distance increases because the portion of the filter visible from the measurement point is decreased. Since EPID scatter factor measurements were made at SEDs of 105 and 140 cm, corresponding collimator scatter factors were measured at SDDs of 106.3 and 141.3 cm, respectively, using an ion chamber.

4.2.4.4 Compensator factor and off-axis energy fluence ratios

Using Eqs. 4.3 – 4.6 to determine the energy fluence at the EPID with and without attenuators in the beam path, CAX compensator measurements were performed and compensator factors calculated using Eq. 4.1. The measurements were then extended to the four off-axis locations. Energy fluence ratios were defined as the energy fluence at an off-axis location divided by that at the CAX, with the compensator in the beam path.

$$OFR = \frac{R^{comp}(AxB, x, y)}{R^{comp}(AxB, x_0, y_0)}, \tag{4.7}$$

116

where $R^{comp}(AxB, x, y)$ is the energy fluence at SDD for a collimator setting A x B at location (x,y). Day's method [Da, 1950] was used to calculate the energy fluence needed for OFR calculation using the EPID (Fig. 4.3). EPID scatter factors for each of the four field sections were obtained from on-axis data for the appropriate field size for the section and the thickness of the compensator along the primary ray path from the x-ray source to the measurement point. The energy fluence at a particular off-axis point was calculated as

$$R^{comp}(AxB, x, y) = \frac{R(EPID, AxB, x, y)}{S_{EPID}(AxB, x, y)} \times OAR(x, y),$$
(4.8)

where $S_{EPID}(AxB, x, y)$ is the EPID scatter factor and OAR(x,y) is an off-axis fluence correction. The latter is required because the EPID flood field calibration process suppresses variations in the beam energy fluence profile, and was obtained by making ion chamber measurements in a 20×20 cm^2 open field at SED = 140 cm, the flood field calibration distance. For the aS500, the maximum permissible field size at the detector is 40 x 30 cm^2. For some clinical compensators, the use of Day's method at an SED of 140 cm required an EPID scatter factor for a larger field size. In such cases the scatter factor was obtained by extrapolation based on a quadratic fit to the measured scatter factors.

4.2.4.5 Compensators used for measurements

To test the validity of the approach, three test compensators were designed as shown in Figure 4.10 – (i) wedge, (ii) hemisphere, and (iii) frustum of pyramid. For these compensators the collimators were set at 14.2 x 14.2 cm^2. Compensator factors and off-axis fluence ratios were measured using the EPID, and compared with results obtained using the clinical QA technique and ion chamber measurements in air. In addition, twenty clinical compensators for different treatment sites including head and neck, larynx, tongue, hypopharynx, brain and sinus were similarly studied. For clinical compensators the planned collimator settings were used. In all of our measurement protocols, values from three consecutive trials were averaged.

117

4.3 RESULTS AND DISCUSSION

4.3.1 EPID Calibration Curve

Figure 4.11 shows the average pixel values from ROI_{CAX} as a function of relative ion chamber readings for open and attenuated fields (both lead and steel shot). These are the raw calibration curves. The maximum variation between average pixel values for the three images used to obtain each data point was $< 1\%$. As seen in the figure, the response of the EPID is different with and without an attenuator in the beam path, and also changes with SED. An over-response of the phosphor to lower energy photons results in the open field curve lying above the attenuated field curve, as low energy photons are preferentially absorbed by the steel shot. The open field data was given a linear fit. The response of the EPID with attenuators in the beam also shows a linear relationship below 0.4 RU, but overall the latter curves were better fit with a quadratic. Table 4.3 presents the regression parameters from fits given to the raw calibration curves. The EPID response for both types of attenuator has a similar quadratic behavior although the regression parameters are different and henceforth only the steel shot attenuators will be discussed. Figure 4.12 shows the EPID response in RU at both SEDs for increasing steel shot absorber thickness. The data have been fit to an exponential form. Under the same measurement conditions, we expect the attenuation coefficient to be smaller if measured at a shorter SED because of the increased contribution from scatter originating in the filter.

4.3.2 EPID Scatter Factors

EPID scatter factors for different thicknesses of steel shot are shown in Figure 4.13. The curves follow a trend of having increasing slopes with increasing thicknesses. The difference between scatter factors for a particular collimator setting is greatest for the largest collimator settings, being about 11.5% at an SED of 105 cm and 2.5% at 140 cm. A 25 x 25 cm^2 field at 140 cm has the same collimator setting as an 18.8 x 18.8 cm^2 field at 105 cm. Hence the increasing differences in the scatter factors

118

with increasing field size at 105 cm appear to be associated with larger collimator openings.

The EPID scatter factors are used to correct the raw calibration curves for open and absorber fields. The effect of this correction is illustrated in Figure 4.14. The raw calibration curve is shifted to increasing values of RU, reflecting the fact that a given pixel value for a 10 x 10 cm^2 field at the EPID corresponds to a greater energy fluence than the same pixel value for the 20 x 20 cm^2 calibration field. This shift was about 8% for SED = 105 cm and 5% for SED = 140 cm. For compensator QC calculations, EPID scatter factors were selected according to central axis compensator thickness and treatment field size by double interpolation (and occasionally, extrapolation) in our measured data set.

After analyzing the calibration curve and scatter factor data, we decided to make compensator QC measurements at the standard EPID working distance of 140 cm, though measurements at 105 cm have been presented for comparison. The choice of 140 cm was made based on the minimal compensator thickness dependence of the scatter factor data, and because the great majority of our clinical compensators can be measured at this distance. The largest field size for a clinical compensator used in our study was 15 x 20 cm^2.

4.3.3 Compensator Factor and Off-axis Energy Fluence Ratios

Differences in measured compensator factors for the test compensators are given in Table 4.4. For the wedge compensator, agreement between the clinical and EPID methods is within 2% at both SEDs. In this case the ion chamber was oriented with its axis perpendicular to the wedge direction. At SED = 105 cm, the ~2% difference between the EPID and ion chamber in air methods may stem from our simplifying assumption that a compensator be characterized by its central axis thickness (2 cm for the wedge) for the purpose of scatter factor determination. At SED = 140 cm, a similar difference between the clinical and ion chamber in air methods likely reflects a combination of the presence of scattering medium ($\leq$1% difference), a

119

greater solid angle from the x-ray source subtended by the active volume of the detector, and a smaller detector positioning uncertainty for the former method. For the hemispherical compensator overall agreement between measurement methods is poorest, with the agreement between the clinical and EPID methods being within 1.5% at SED = 105 cm and 3.5% at SED = 140 cm. This compensator has a central axis thickness of 4 cm, which decreases by 6.3% at a radius of 0.5 cm. A 1 cm diameter circle at the exit surface of the compensator projects to ~1.5 cm and ~2.0 cm diameter circles at the two SEDs; the active length of the ion chamber is 2.1 cm. Consequently at SED = 140 cm, agreement between the EPID and ion chamber in air methods is better, and between the clinical and ion chamber in air methods worse, than at SED = 105 cm. To confirm this explanation of ion chamber volume effect, additional measurements of the compensator factor were performed using a small volume IC-10 ion chamber (V = 0.125 mm^3). It was observed that the difference between clinical and ion chamber in air measurements was reduced to 2.7%, and between EPID and ion chamber in air to 1.4% at an SED of 140 cm. Thus the Farmer chamber volume does affect comparisons, and can cause a discrepancy for compensators with non-linear dose gradients across the central axis. Furthermore, to determine whether spectral effects come into play when comparing an ion chamber measurement at a depth of 5 cm in a full phantom to that in air, fluence measurements were made for the hemispherical compensator with 2 − 10 cm of buildup on a full phantom with the IC-10 chamber located at isocenter. It was observed that there was essentially no change in the compensator factor for depths of 2 - 6 cm, thus ruling out any spectral effects. As noted for the wedge compensator, part of the difference between the EPID and ion chamber in air methods at both SEDs likely arises from our simplistic approach to determining an EPID scatter factor. We tested this hypothesis by alternatively obtaining an EPID scatter factor for the thickness of a slab of equivalent volume, and found that the difference between the EPID and ion chamber in air methods fell to 3.6% from 5.9% at SED = 105 cm, but remained essentially unchanged at SED = 140 cm. This behavior is consistent with the data in Fig. 4.13, which show that EPID scatter factors vary less with compensator thickness at the longer SED. The difference between the clinical and

120

ion chamber in air method at SED = 105 cm, and between the EPID and ion chamber in air method at SED = 140 cm, may reflect an increased sensitivity to ion chamber positioning uncertainties for the hemispherical compensator. For the frustum of pyramid compensator, agreement between the clinical and EPID methods is < 1% at SED = 105 cm, but ~5% at SED = 140 cm. As with the hemispherical compensator, the Farmer chamber volume is the major cause of the observed difference. Difference trends for all three methods follow those for the hemispherical compensator, however the agreement between the clinical and ion chamber in air methods at SED = 105 cm, and between the EPID and ion chamber in air methods at SED = 140 cm, is better, likely because of a reduced sensitivity to ion chamber positioning uncertainties.

Differences in off-axis fluence ratios for the test compensators measured using different methods are shown in Figure 4.15. For all three compensators, agreement between the clinical and EPID methods is within 2% at both SEDs for measurement points Q1 - Q3. However for measurement point Q4, a difference of ~3% is seen for the hemisphere and frustum of pyramid, respectively, which may be related to the ~1.5% beam asymmetry observed in this quadrant (Section 4.2.1.1). Comparison of the clinical and EPID methods with the ion chamber in air method reveals trends similar to those for the compensator factor measurements.

For the clinical compensators, differences in compensator factors determined by the various methods are illustrated in Figure 4.16. Comparing EPID vs. clinical methods, the average difference is 1.4 ± 1.0% at SED = 105 cm and -0.9 ± 1.3% at SED = 140 cm. Comparing EPID vs. ion chamber in air methods, the average difference is 1.7 ± 0.9% at SED = 105 cm and 0.2 ± 0.7% at SED = 140 cm. The better agreement at the longer SED likely reflects the smaller angle subtended by the active length of the Farmer chamber at the x-ray source.

Figure 4.17 shows the distribution of differences in OFRs measured using the various methods for the 20 clinical compensators. Comparing EPID vs. clinical methods, the average difference is 0.9 ± 1.5% at SED = 105 cm and 1.0 ± 1.8% at SED = 140 cm. Comparing EPID vs. ion chamber in air methods, the average difference is

121

0.1 ± 1.4% at SED = 105 cm and -0.1 ± 1.7% at SED = 140 cm. For our clinical QC procedure the EPID OFR depends on OAR (Eq. 4.8), hence it is important that we determine the latter at each off-axis measurement point, as photon beam asymmetries of up to 2% are tolerated in clinical practice [Ku, 1994]. This explicit dependence on OAR could be eliminated by calibrating the EPID for dosimetry purposes without flood field correction. However, since this is not a user-selectable option for the aS500 EPID, this latter approach was not possible for our measurements.

Although working at an SED of 140 cm appears to yield slightly more consistent results for compensator factors, the maximum permissible collimator setting at this SED is 28.6 x 21.4 cm^2. This may become a limitation in clinical practice. However, an advantage of working at this distance is that EPID scatter factors do not vary much with compensator thickness (Fig. 4.13(b)); hence it may be possible to use average thickness values to simplify the compensator QC procedure.

4.4 SUMMARY AND CONCLUSION

Of the various methods reported to perform EPID-based compensator QC, those that yield a two-dimensional thickness distribution [Pa, 1999] for comparison with an intended distribution appear to be the most practical. Other methods looking at the uniformity of transmitted fluence through a patient phantom [Ro, 1995] or comparing fluence measurements with theoretical calculations [Lo, 1996b] are also feasible but involve interpreting fluence differences. The objective here was to adapt an a-Si EPID as an ion chamber replacement to make compensator factor and off-axis ratio measurements in an existing QC procedure. The benefits of doing so include elimination of ion chamber set-up and ease of extension to other off-axis measurement points. Chapter 5 details the investigation of two-dimensional compensator thickness measurement with the a-Si EPID.

The central idea of our method is to relate the average EPID pixel value in a region of interest to the reading obtained with an ion chamber in air at the same measurement position. To do so, we measured calibration curves relating image pixel

122

values to incident energy fluence for a fixed field size at the EPID, and scatter factors accounting for field size effects, at SEDs of 105 and 140 cm. Because of the beam modifying properties of the steel shot and the spectral sensitivity of the detector, we observed a response that is highly linear for open fields, exhibits a distinct quadratic component for attenuated fields, and depends on SDD. Consequently, we obtained separate calibration curves for open and attenuated fields and for each SDD. We also obtained EPID scatter factors for the full range of compensator thicknesses encountered in clinical practice. For the purpose of EPID scatter factor determination for an arbitrarily shaped compensator, we took the thickness to be equal to the pathlength through the compensator along the primary ray from the x-ray source to the energy fluence measurement point.

In implementing the EPID method, we identified two technical issues that merit attention. The first was a lack of correspondence between the EPID position reported by the hand controller (as the top of the detector stack), and the image-forming plane of the detector, which is 1.3 cm downstream of the reported position. The second was the occasional, apparently random occurrence of prematurely acquired images in 0-50%-0 acquisition mode, characterized by a ~4% reduction in pixel values. These images were identified by their recorded acquisition time and discarded.

The accuracy of our method was assessed by comparing measured compensator factors and off-axis energy fluence ratios for three test compensators and twenty clinical compensators at SEDs of 105 and 140 cm against those obtained with a Farmer chamber in a polystyrene phantom and in air. For the hemisphere and frustum of pyramid test compensators, compensator factors for the EPID and clinical methods differed by > 2% because of steep dose gradients across the central beam axis in conjunction with the sensitive length of the Farmer chamber. For the wedge compensator, agreement was < 2%. Similar levels of agreement were observed for the off-axis ratios. For the clinical compensators at the selected SED of 140 cm, compensator factors for the EPID and clinical methods agreed on average to within 0.9%, and off-axis ratios agreed on average to within 1.0%.

123

Consequently, we conclude that the aS500 is suitable as an ion chamber replacement for compensator QC, and that a-Si EPIDs as a class can provide a basis for the development of faster, more comprehensive QC protocols for compensators.

TABLE 4.1

aS500 EPID operating parameter values selected for this work. Complete parameter descriptions can be found in Chapter 2.

EPID Operating Parameters	
Beam energy	6 MV
Repetition rate	300 MU/min
Sync delay	0 ms
Number of resets	5
Rows/PV sync	20
Number of frame averages	2
Scanning mode	Standard
Imaging sequence	0-50%-0

TABLE 4.2

Measurement of steel shot density.

Trial	Mass (± 0.01 g)	Volume (± 0.5 cc)	Density ρ (g/cc)	$\delta\rho$ (g/cc)
1	231.95	49.5	4.69	0.05
2	235.62	50.2	4.69	0.05
3	229.04	48.9	4.68	0.05

TABLE 4.3

Regression results for fits to the raw EPID calibration curves. The form of the fit for the open field is $y = a_0 + a_1x$ and for the attenuator field is $y = a_0 + a_1x + a_2x^2$, where y is pixel value and x is energy fluence expressed in relative units.

Absorber	SED (cm)	a_0	a_1	a_2	R^2
None	varies	-13.3	5176.5	-	0.9998
Lead	105	93.1	3697.1	1371.2	0.9998
Lead	140	7.9	4048.4	1658.0	0.9999
Steel Shot	105	1.0	4436.7	703.2	0.9999
Steel Shot	140	34.7	4211.4	1570.3	0.9997

126

TABLE 4.4

Relative differences in compensator factors for test compensators obtained using the clinical method, and the EPID method, with respect to an ion chamber in air at SED = 140 cm. Measurements from three consecutive trials were averaged for each method.

	Difference in compensator factor with respect to IC in air (%)			
	SED=105 cm		SED=140 cm	
Compensator	Clinical	EPID	Clinical	EPID
Wedge	0.00±0.00	1.98±0.05	2.35±0.00	0.54±0.01
Hemisphere	4.41±0.04	5.90±0.10	7.00±0.30	3.65±0.09
Frustum of pyramid	2.05±0.00	2.84±0.07	5.85±0.01	0.80±0.02

127
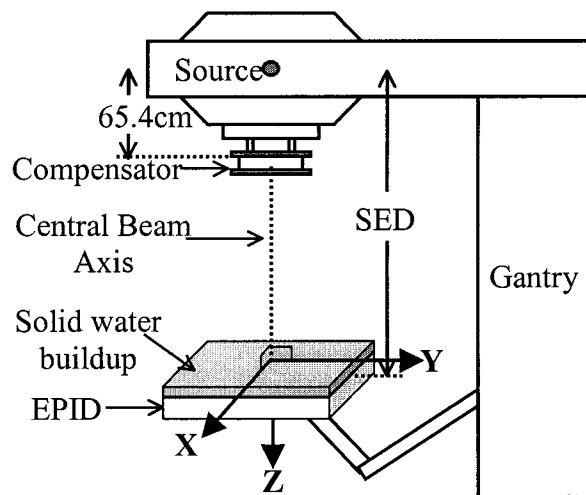
Figure 4.1: Experimental setup for compensator measurements illustrating the coordinate convention used. The gantry angle was set at 0° for all measurements.

128
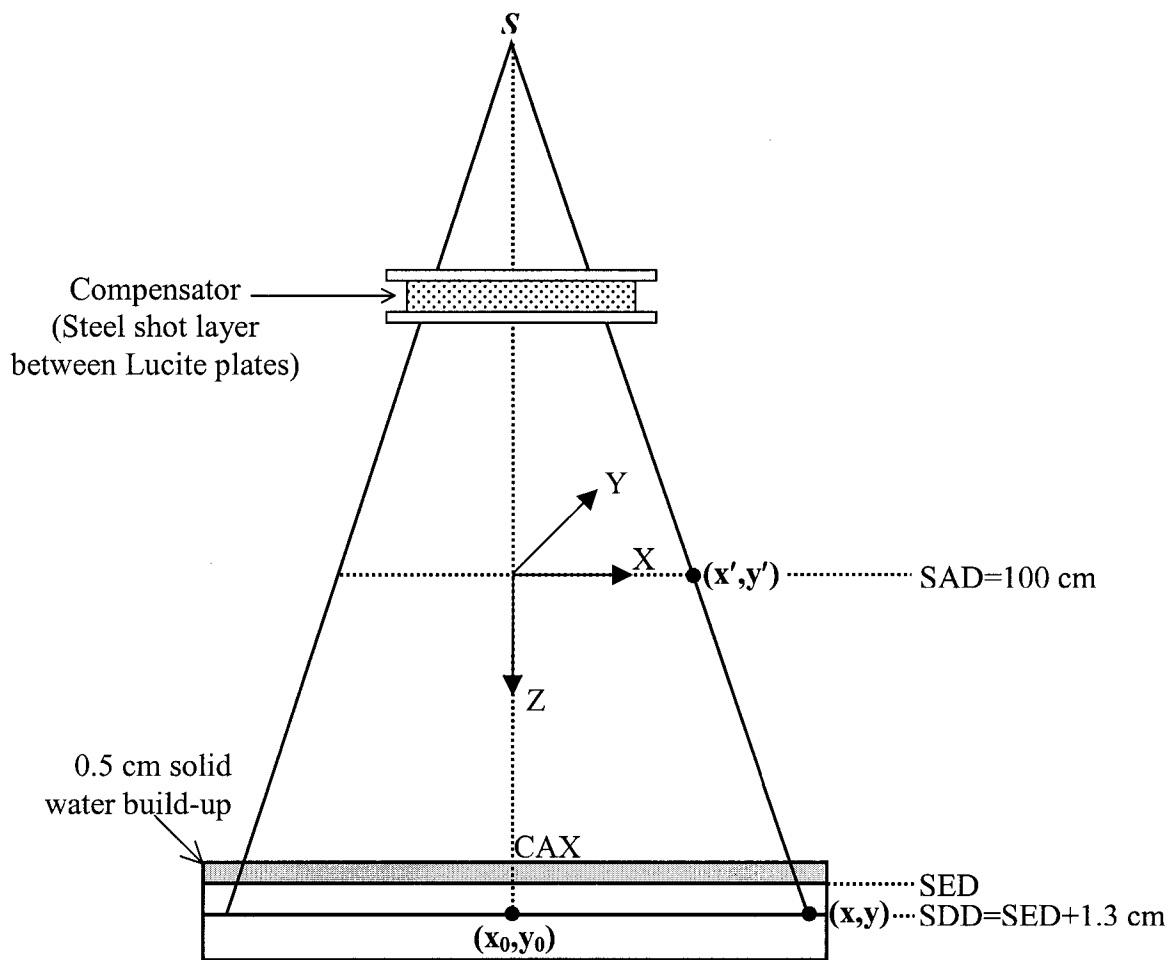
Figure 4.2: Schematic representation of the geometry used for describing compensator measurements.

129
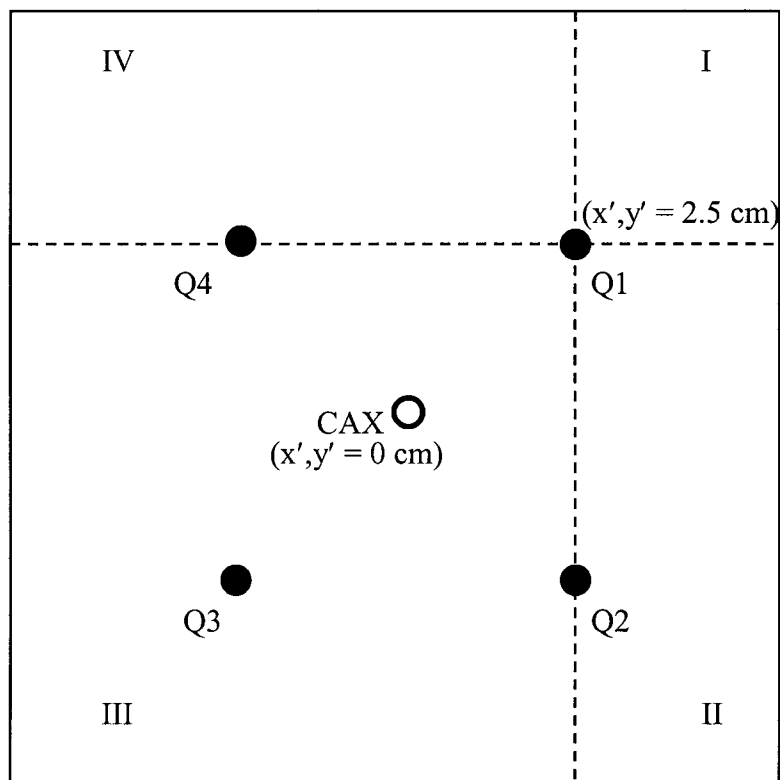
Figure 4.3: Division of the radiation field into sections (I – IV) for a Day's method calculation to determine the EPID scatter factor for the off-axis position at {x' = + 2.5 cm, y' = + 2.5 cm} labeled as Q1. The open and solid circles represent the CAX and OAR measurement positions, respectively.

130
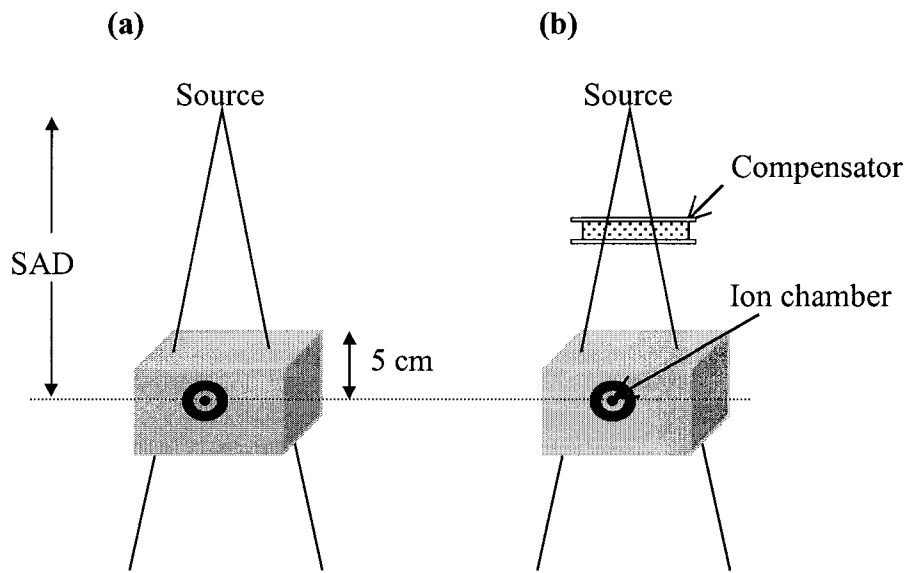
Figure 4.4: Setup for clinical compensator QC to measure compensator factor (not to scale): **(a)** open field, and **(b)** attenuated field.
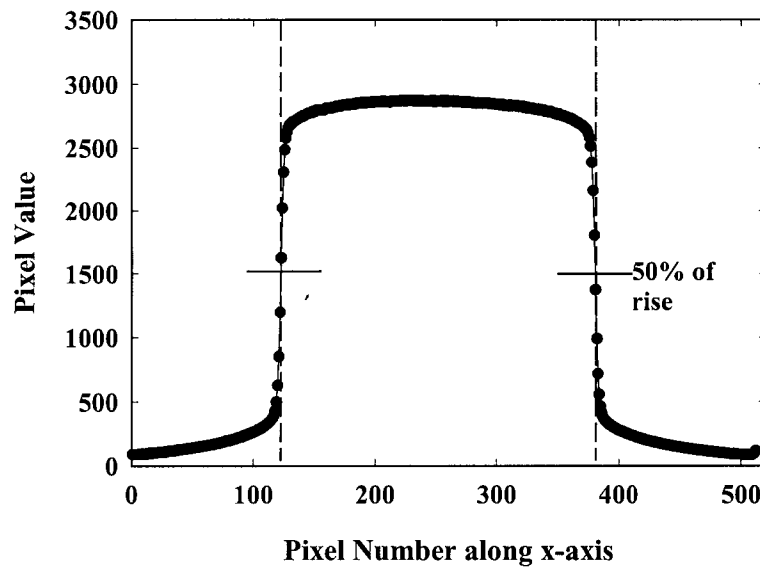
Figure 4.5: Illustration of field edge determination for the aS500 EPID. Because the pixel values are roughly proportional to ion chamber readings for an open field, field edges can be determined as the locations where pixel values drop to 50% of their maximum value.
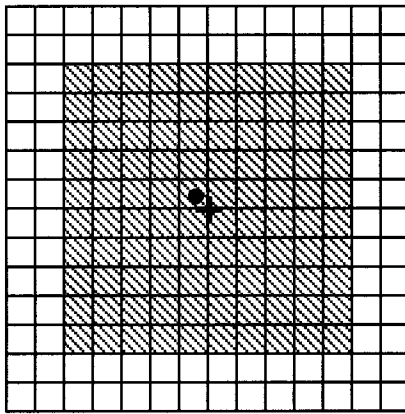
Figure 4.6: Relationship between the central axis position (circle), the nearest pixel corner (cross) and the 10x10 pixel region of interest used for the central axis EPID measurements (shaded).

133
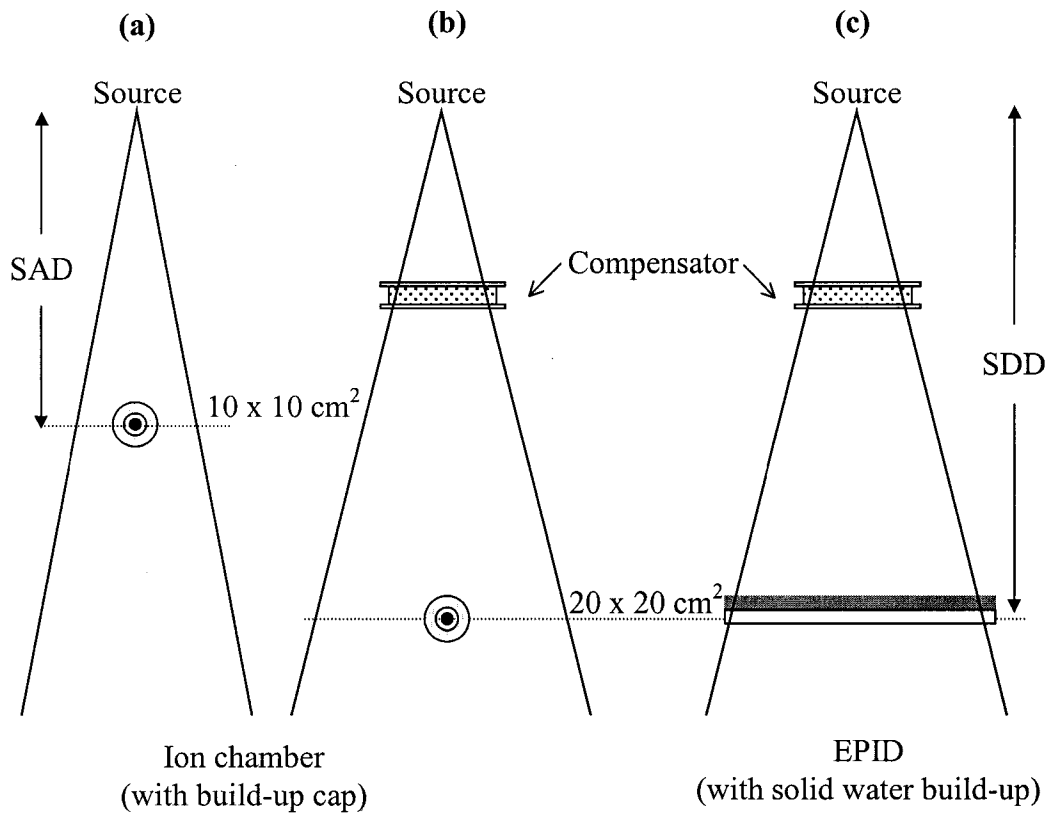
Figure 4.7: Experimental set-up for measuring the calibration curve. Ion chamber readings for **(b)** a 20 x 20 cm^2 field at SDD are normalized to **(a)** a 10 x 10 cm^2 field at SAD. EPID measurements are made **(c)** at SDD with the solid water build-up.

134

1. Set, $S_{EPID}^{set} = 1$

2. Inferred EPID fluence,

$$R_{ref}(EPID,20x20) = R(EPID,20x20) \times S_{EPID}^{set}$$

3. Determine fit parameters for open and attenuated calibration curves,

$$f_{open}(P(20x20)) = y_0 + a \cdot R_{ref}(EPID,20x20)$$

$$f_{comp}(P(20x20)) = y_0' + a' \cdot R_{ref}(EPID,20x20) + b' \cdot R_{ref}(EPID,20x20)^2$$

4. Update R(EPID,(AxB)) for different field sizes using,

$$f_{open}(P(AxB)) = y_0 + a \cdot R(EPID,AxB)$$

$$f_{comp}(P(AxB)) = y_0' + a' \cdot R(EPID,AxB) + b' \cdot R(EPID,AxB)^2$$

5. Calculate S_{EPID}^{new} for each field size,

$$S_{EPID}^{new}(AxB) = \frac{R(EPID,AxB)/S_C(AxB)}{R(EPID,10x10)/S_C(10x10)}$$

6. $\left| S_{EPID}^{new} - S_{EPID}^{set} \right| < 0.1\%$

No → Set, $S_{EPID}^{set} = S_{EPID}^{new}$

Yes

7. Print S_{EPID}^{new}

Figure 4.8: The flow chart shows the iterative algorithm used to determine EPID scatter factors for the a-Si EPID.

135
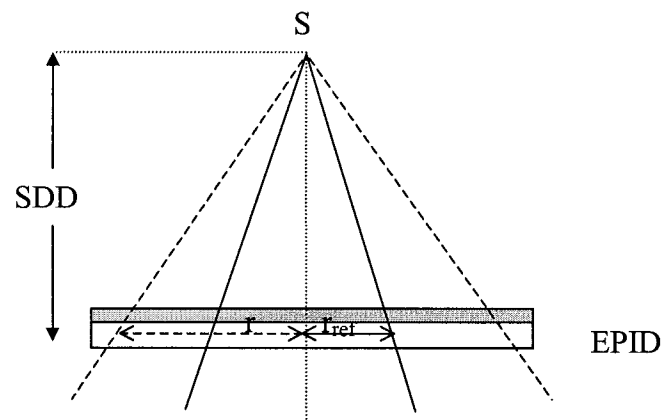
Figure 4.9: Experimental setup for measuring the EPID scatter factor at SDD, where r and r_{ref} are the sides of any square field and the reference 10 x 10 cm^2 field, respectively.

Side View   Top View

(a)

(b)

(c)
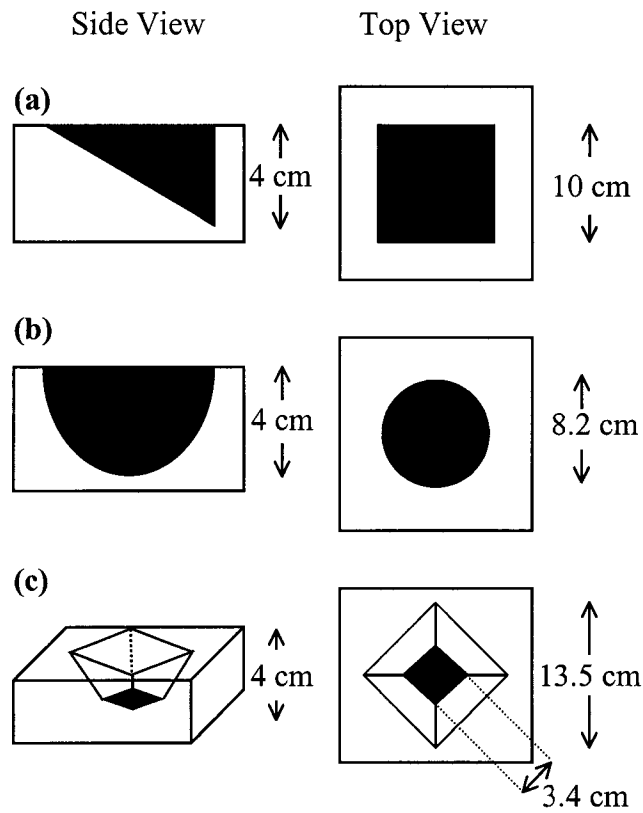
Figure 4.10: Compensators fabricated for testing our EPID-based QC method. The compensators in the shapes of: **(a)** wedge, **(b)** hemisphere, and **(c)** frustum of pyramid, have physical dimensions as indicated in the figure.

137
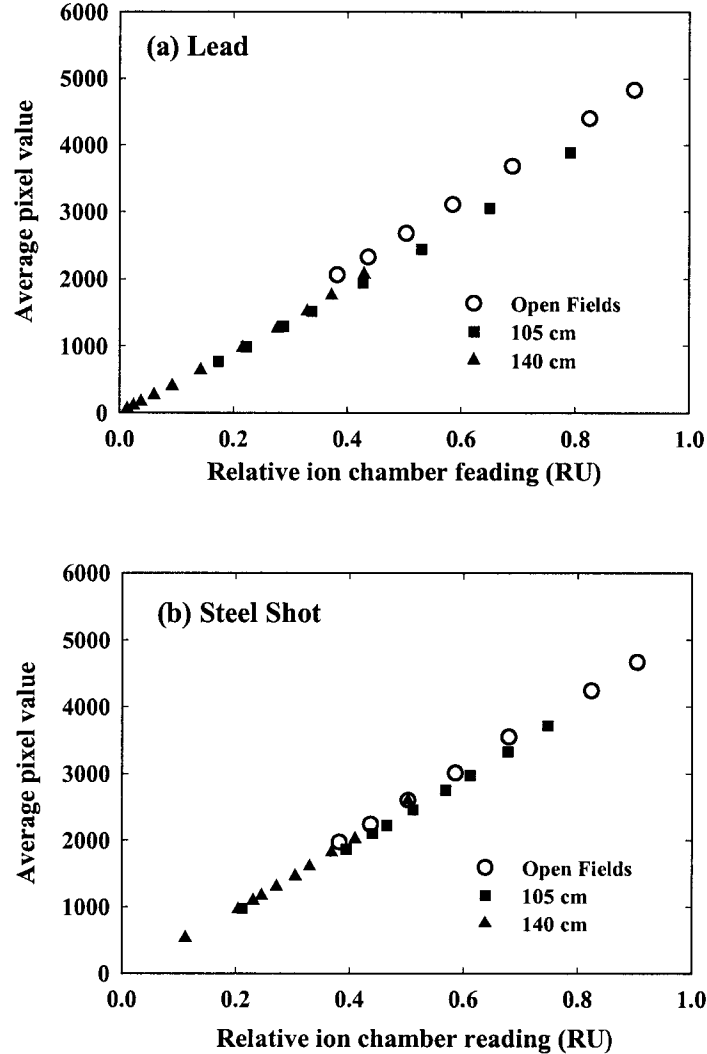
Figure 4.11: Raw calibration curves for the Varian aS500 EPID for a 6 MV photon beam obtained using open fields and with **(a)** lead and **(b)** steel shot attenuators at SEDs of 105 and 140 cm. Open field measurements were made at SEDs of 105, 110, 120, 130, 140, 150, and 160 cm. The steel shot measurements were performed using the same EPID on a different accelerator than the lead measurements (the EPID was moved after the lead measurements were completed), hence the slight change in pixel response for open fields (<3%) in (a) and (b). Error bars are not shown, as they are smaller than the plotted symbols. Similarly the 95% confidence interval plots are not shown as they passed through the symbols.

138
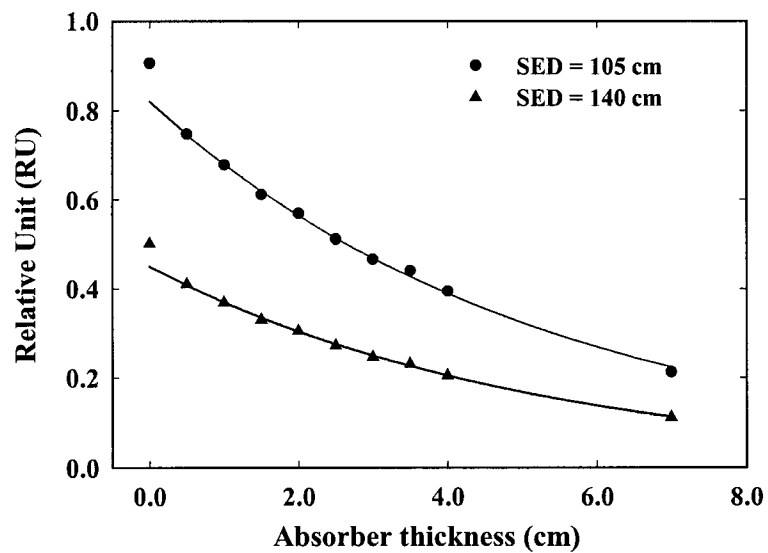
Figure 4.12: Variation of the EPID response in the presence of steel shot attenuators in the beam path for a field size of 20x20 cm^2 at the detector. An exponential fit of the form y = a·exp(-bx) was given to each curve. For SED = 105 cm, a = 0.8583 and b = 0.2033; for SED = 140 cm, a = 0.4749 and b = 0.2180. Data for the 0 cm thickness are presented to show the different response for open fields (not used in the fits).

139
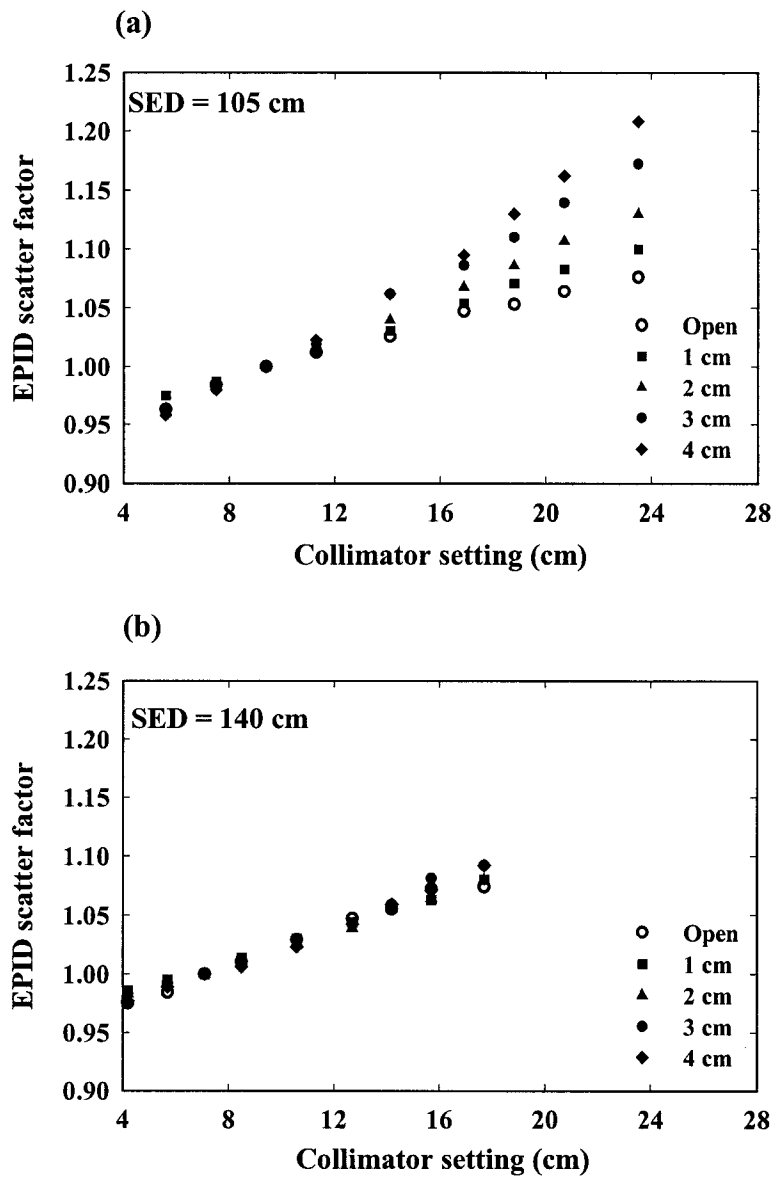
Figure 4.13: EPID scatter factors for square fields measured with the detector at SEDs of **(a)** 105 and **(b)** 140 cm for open and steel shot attenuated beams.
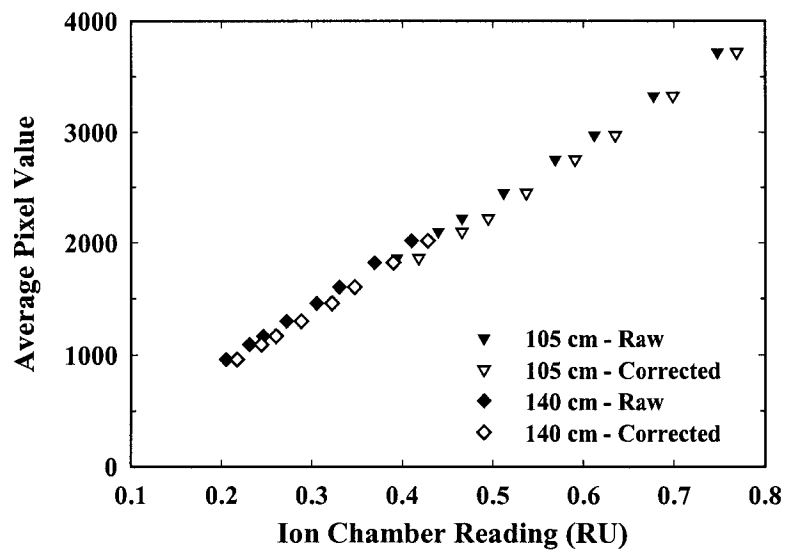
Figure 4.14: Shifts in the raw calibration curves for steel shot absorbers brought about by correcting for the calibration field size using the EPID scatter factor.

141
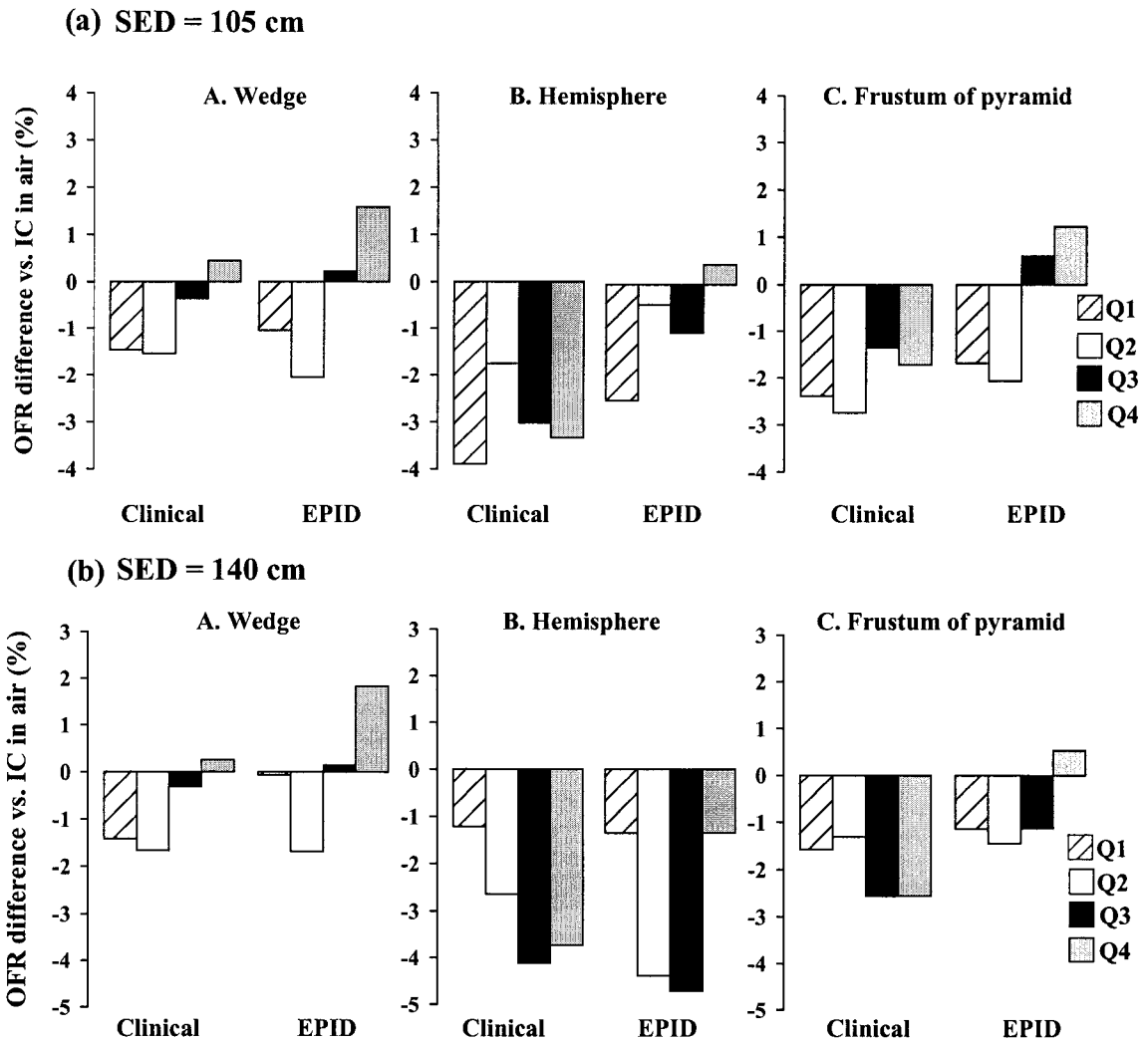
Figure 4.15: Differences in OFR values for test compensators for the clinical and EPID methods with respect to the ion chamber in air method, measured at off-axis points Q1 - Q4 (see Fig. 4.3) at SEDs of **(a)** 105 cm and **(b)** 140 cm.

142
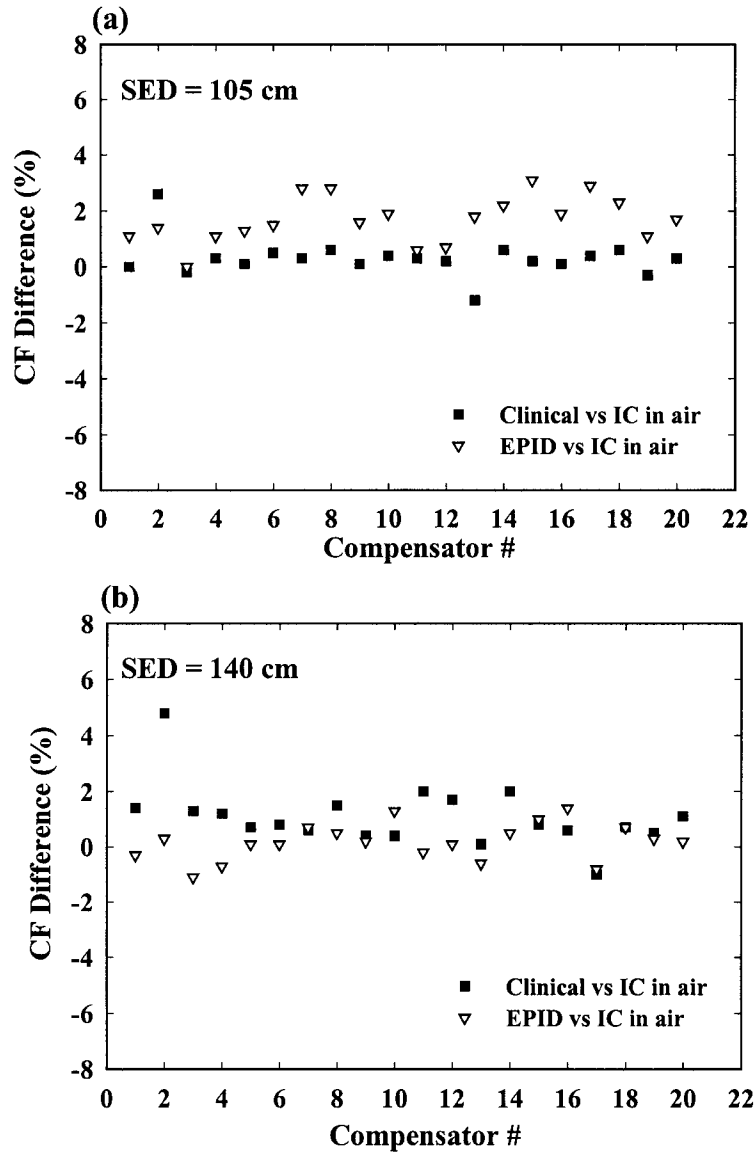
Figure 4.16: Differences in compensator factor values for the clinical vs. ion chamber in air methods, and for the EPID vs. ion chamber in air methods, at SEDs of **(a)** 105 cm and **(b)** 140 cm.

143
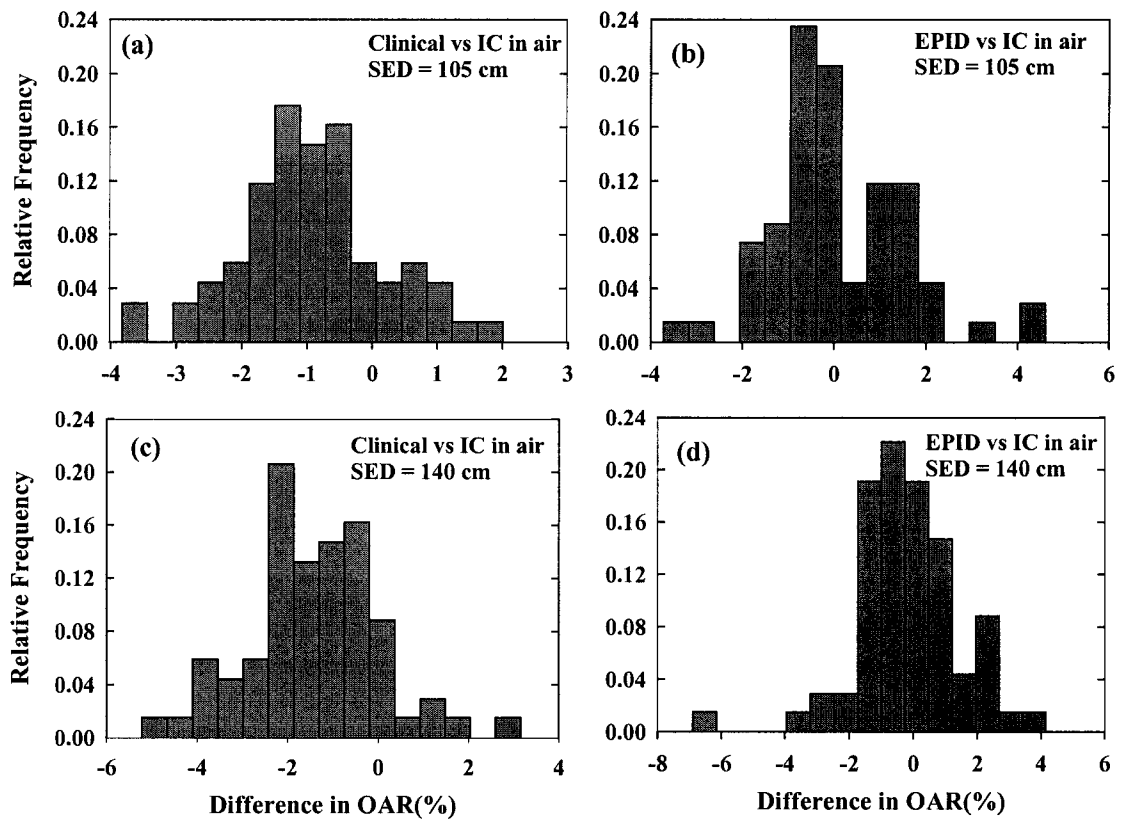
Figure 4.17: Frequency distribution of differences in OFR values for clinical compensators at SEDs of 105 and 140 cm for **(a,c)** clinical vs. ion chamber in air methods and **(b,d)** EPID vs. ion chamber in air methods.

144

4.5 REFERENCES

[Ba, 1998]   P. S. Basran, W. Ansbacher, G. C. Field, B. R. Murray, "Evaluation of optimized compensators on a 3D planning system," Medical Physics. **25**, 1837-1844 (1998).

[Bo, 1982]   A. L. Boyer, "Compensating filters for high energy X rays," Medical Physics. **9**, 429-433 (1982).

[Ch, 1994]   E. L. Chaney, T. J. Cullip, and T. A. Gabriel, "A Monte Carlo study of accelerator head scatter," Medical Physics. **21**, 1383-1390 (1994).

[Ch, 2001]   J. Chang, G. S. Mageras, C. C. Ling, and W. Lutz, "An iterative EPID calibration procedure for dosimetric verification that considers the EPID scattering factor," Medical Physics. **28**, 2247-2257 (2001).

[Da, 1950]   M. J. Day, "A note on the calculation of dose in x-ray fields," British Journal of Radiology. **23**, 368-369 (1950).

[El, 1959]   F. Ellis, E. J. Hall, and R. Oliver, "A compensator for variations in tissue thickness for high energy beams," British Journal of Radiology. **32**, 421-422 (1959).

[El, 1999]   Y. El-Mohri, L. E. Antonuk, J. Yorkston, K. -W. Jee, M. Maolinbay, K.L. Lam, J.H. Siewerdsen, "Relative dosimetry using active matrix flat panel imager (AMFPI) technology," Medical Physics. **26**, 1530-1541 (1999).

[Fr, 1998]   B. Fraass, K. Doppke, M. Hunt, G. Kutcher, G. Starkschall, and J. Van Dyke, "American Association of Physicists in Medicine Radiation Therapy Committee Task Group 53: Quality assurance for clinical radiotherapy treatment planning," Medical Physics. **25**, 1773-1836 (1998).

[In, 1996]   International Electrotechnical Commission, "Radiotherapy equipment: Coordinates, movements and scales," IEC 1217 (1996).

[Jo, 1988]   J. M. Johnson, M. M. Ali, and F. M. Khan, "Quality control of custom made compensators," Medical Dosimetry. **13**, 109-111 (1988).

[Kh, 1994]   F. M. Khan, *"The Physics of Radiation Therapy,"* 2nd Edition, Williams & Wilkins, Baltimore, MA (1994).

[Ku, 1994]   G. J. Kutcher, L. Coia, M. Gillin, W. F. Hanson, S. Leibel, R. J. Morton, J. R. Palta, J. A. Purdy, L. E. Reinstein, G. K. Svensson, M. Weller, and L. Wingfield, ''Comprehensive QA for radiation oncology: Report of AAPM Radiation Therapy Committee Task Group 40,'' Medical Physics. **21**, 581-618 (1994).

[Lo, 1996b]   D. A. Low, Z. Li, and E. E. Klein, "Verification of milled two-dimensional photon compensating filters using an electronic portal imaging device," Medical Physics. **23**, 929-938 (1998).

[Ma, 1980]   K. P. Mandal, D. H. Baxter, and P. Ray, "Thin lead sheets as tissue compensators for larger field irradiation," International Journal of Radiation Oncology Biology Physics. **6**, 513-517 (1980).

[Me, 2004]   G. V. Menon and R. S. Sloboda, "Quality assurance measurements of a-Si EPID performance," Medical Dosimetry. **29**, 11-17 (2004).

[Pa, 1998a]   H. Parsaei, E. El-Khatib, and R. Rajapakshe, "The use of electronic portal imaging system to measure portal dose and portal dose profiles," Medical Physics. **25**, 1903-1909 (1998).

[Pa, 1999]   K. L. Pasma, M. Kroonwijk, E. B. van Dieren, A. G. Visser, and B. J. M. Heijmen, "Verification of compensator thicknesses using a fluoroscopic electronic portal imaging device," Medical Physics. **26**, 1524-1529 (1999).

[Po, 2000a]   PortalVision^{TM} aS500 Rel.6 Reference Manual, Varian Medical Systems Inc., June 2000.

[Re, 2000]   S. Reise, N. Bleackley, E. M. Donovan, P. M. Evans, V. N. Hansen, M. Partridge, and J. R. Yarnold, "IMRT for breast radiotherapy using physical compensators and MLC," International Journal of Radiation Oncology Biology Physics. **46**, 748 (2000).

[Ro, 1995]   D. M. Roback and B. J. Gerbi, "Evaluation of electronic portal imaging device for missing tissue compensator design and verification," Medical Physics. **22**, 2029-2034 (1995).

[Va, 1995]   J. P. C. van Santvoort, D. Binnekamp, B. J. M. Heijmen, and P.C. Levendag, "Granulate of stainless steel as compensator material," Radiotherapy and Oncology. **34**, 78-80 (1995).

[We, 1988]   K. J. Weeks, B.A. Fraass, and K. M. Hutchkins, "Gypsum mixtures for compensator construction," Medical Physics. **15**, 410-414 (1988).

[Yu, 1996]   M. K. Yu and R. Sloboda, "Analytical representation of head scatter factors for shaped photon beams using a two-component x-ray source model," Medical Physics. **23**, 973-983 (1996).

CHAPTER 5: COMPENSATOR THICKNESS VERIFICATION USING AN AMORPHOUS SILICON EPID

5.1 INTRODUCTION

In Chapter 4, the suitability of an amorphous silicon EPID to serve as an ion chamber replacement in the clinical QC protocol was described. This investigation yielded compensator factors and off-axis fluence ratios that agreed with ion chamber measurements to within 2%. However, a more comprehensive form of compensator QC involves the determination of compensator thickness. Accordingly, the objective of the work presented in this chapter is to investigate the use of an a-Si EPID to measure a 2-D compensator thickness distribution, for comparison with an intended distribution, in order to verify the accuracy of compensator fabrication and mounting. Although thickness profiles have been measured using video-based EPIDs to an accuracy of ~0.5 mm [Pa, 1999], this capability has not yet been demonstrated for a-Si EPIDs. As mentioned earlier, the latter devices are currently replacing the other types in the clinic and have a different radiation response. The thickness measurement methodology described here consists of a 3-stage process: (i) measuring the total transmission through the compensator, (ii) extracting the primary transmission by subtracting an estimated scatter component, and (iii) calculating the thickness using a model for primary transmission.

5.2 MATERIALS AND METHODS

5.2.1 Equipment and Software

Compensator thickness measurements were performed with a newer but functionally similar Varian aS500 EPID to the one used for earlier work. This EPID was mounted on a dual energy Varian 21EX linac (Varian Oncology Systems, Palo Alto, CA). Measurements were performed using 6 MV photons delivered at 300 MU/min with the EPID positioned at a SED of 140 cm with a 0.5 cm slab of solid

water on top of the imaging cassette to ensure electronic equilibrium. The operating parameters were the same as shown in Table 4.1.

Compensators are manufactured using the procedure described in Section 4.2.1.2. The intended thicknesses for milling are calculated on a 2-D grid, specified in the perpendicular direction to the top surface of the compensator at a source-to-axis distance (SAD) of 100 cm (i.e. thickness location coordinates are geometrically magnified), and stored in a "cut file" for subsequent use. An offset of 0.3 cm is added to each compensator to avoid minimum thicknesses smaller than this value, which are difficult to fill uniformly. Compensators can be cut from Styrofoam slabs using our milling device (TS-5000 Huestis Compu•former) to a quoted milling accuracy of better than ± 1 mm and a slab positioning uncertainty of ± 0.5 mm. The distance from the linac x-ray source to the top of the steel shot layer for a mounted compensator (SCD) is 65.4 cm. All field sizes used in this work are specified at the source to detector distance (SDD = SED + 1.3 cm (Sec 2.2.1)) unless otherwise indicated.

Ion chamber measurements were made using Wellhöfer CC-13 and IC-10 ion chambers (Scanditronix Wellhöfer, Bartlett, TN) having active volumes of 0.130 and 0.125 cm^3, respectively. Data analysis and analytical model calculations were performed using Matlab 6.5 software (The Mathworks Inc., Nattick, MA).

5.2.2 Thickness Measurement Methodology

Our methodology for radiographic thickness determination is based on EPID transmission measurements, and is summarized in the following three steps.

(1) The measured total transmission, T_T, obtained from a ratio of EPID energy fluence readings with and without the compensator in place is decomposed into a primary component, T_P (primary photon attenuation by the compensator), and a scatter component, T_S (scattered photon production in the compensator),

$$T_T(AxB,x,y) = T_P(AxB,x,y) + T_S(AxB,x,y), \qquad (5.1)$$

149

where A x B is the field size and (x,y) are measurement position co-ordinates at SDD (Fig. 5.1). The raw EPID pixel values are corrected for the non-linearity in EPID response and field size effects to yield energy fluence readings.

(2) The primary component is obtained from the total transmission by subtracting an estimate of the scatter component calculated using an analytical model.

(3) Compensator thicknesses are then determined from an exponential attenuation model of the primary component of transmission,

$$T_P(AxB, x, y) = \alpha \times \exp\{-\mu_{ss}(A \times B, x, y) \cdot t_P(x, y)\}, \tag{5.2}$$

where t_P is the attenuation path length of a primary ray passing through the compensator and intersecting the EPID imaging plane at (x,y) (Fig. 5.1), α is the amplitude and a constant, and $\mu_{ss}(AxB,x,y)$ is the effective linear attenuation coefficient for steel shot as a function of field size and position. To effectively model changes in the attenuation coefficient with attenuator thickness, we employed the empirical form for μ_{ss} recommended by Yu et al. [Yu, 1997],

$$\mu_{ss}(A \times B, x, y) = \frac{\mu_0(A \times B, x, y)}{1 + \kappa \cdot t_P(x, y)}. \tag{5.3}$$

In this relation, $\mu_0(x,y)$ describes the initial attenuation of the incident beam and κ is a positive parameter termed the hardening coefficient which accounts for spectral changes in the beam as it progresses through a material.

Finally, the component of path length normal to the top surface of the compensator, t, is calculated for comparison with the intended thickness obtained from the cut file,

$$t = \cos(\theta) \cdot t_P, \tag{5.4}$$

where θ is the angle between the beam CAX and the primary ray path. The intended normal thickness required for comparison with EPID measurement corresponds to the point where the primary ray intersects the bottom of the compensator at (x″,y″) (see Appendix 5.1).

150

The first step is thus to determine the total transmission as measured by the EPID.

5.2.2.1 Measurement of total transmission

Thickness determination commenced with the acquisition of two images – one with the compensator in place and one for an open field – for the clinically prescribed field size. After defining the field edges using the edge analysis technique, the location of the CAX on both images was determined to the nearest pixel corner [Sec 4.2.3] and the image area was divided into 4 x 4 pixel regions of interest (ROIs $\approx$ 3.1 x 3.1 mm^2) around this point for subsequent analysis. Average pixel values from these ROIs were used to determine total transmission, defined as the ratio of the inferred EPID energy fluence reading with the compensator in place, R^{comp}, to the reading at the same location in an open field, R^{open},

$$T_T(EPID, AxB, x, y) = \frac{R^{comp}(EPID, AxB, x, y)}{R^{open}(EPID, AxB, x, y)}.$$

(5.5)

The inferred energy fluence readings R were obtained as,

$$R(EPID, AxB, x, y) = f(P(x, y)) \times S_{EPID}(AxB, x, y),$$

(5.6)

where $f(P(x, y))$ is a calibration curve relating the mean pixel value P from a ROI at (x,y) to the ion chamber reading in air at the same SDD for a fixed calibration field size, and $S_{EPID}(AxB, x, y)$ is the EPID scatter factor for depth d_{max} that takes into account how detector scatter varies with field size and detector location (Sec. 4.2.4.1). Full details of the determination of the calibration curve and EPID scatter factors for the aS500 EPID can be found in Sections 4.2.4.2 and 4.2.4.3 respectively. The specific methodology for this project is described in overview in the following paragraphs. Measurement of a new set of calibration curves and EPID scatter factors was required because we used a different aS500 EPID and linac for this work than those described in previous chapters.

The open and attenuated field calibration curves were measured at a SED of 140 cm. This detector distance was chosen to reduce scatter to the detector from the

151

compensator, and also because it is the standard clinical imaging distance. A reference field size of 20 x 20 cm² at the detector was set for calibration measurements made for (a) open fields at varying SDDs from 105 - 160 cm, and (b) fields attenuated by steel shot slabs of increasing thickness, from 0.5 to 4.5 cm in increments of 0.5 cm, at a fixed SED of 140 cm. The EPID response was determined as the average pixel value in a 10 x 10 pixel ($\approx$ 8 x 8 mm²) region of interest located at the CAX (ROI$_{CAX}$). Corresponding energy fluence measurements for the calibration curve were made with a Wellhöfer CC-13 IC in air at the same SDD.

We characterized the phantom scatter of the EPID by applying the same iterative approach discussed in Section 4.2.4.3 [Ch, 2001]. Following this method, the calibration curve and a set of ROI$_{CAX}$ values for increasing field sizes (6 x 6 to 28 x 28 cm²) and attenuator thicknesses (0.5 to 4.5 cm) were used to obtain a calibration curve for a 10 x 10 cm² field and a self-consistent set of EPID scatter factors for other field sizes of interest. The EPID scatter factors, determined on the beam CAX, are a function of field size and compensator thickness (Eq. 4.6). To obtain values off the central axis, Day's method [Da, 1950] was employed. In subsequent calculations we used the primary ray path thickness, t_P, (Fig. 5.1) to look up appropriate values of S$_{EPID}$ corresponding to different locations (x,y) on the detector.

Having determined the calibration curve and EPID scatter factors, the total transmission in Eq. 5.1 can now be obtained as

$$T_T\left(EPID, AxB, x, y\right) = \frac{\Re^{comp}\left(EPID, AxB, x, y\right)}{\Re^{open}\left(EPID, AxB, x, y\right)}, \tag{5.8}$$

where

$$\Re^{comp/open}\left(EPID, AxB, x, y\right) = \frac{\Re^{comp/open}\left(EPID, 10x10\right)}{S^{comp/open}_{EPID}\left(AxB, x, y\right)} \times OAX\left(x, y\right). \tag{5.9}$$

Here OAX(x,y) is the off-axis fluence ratio introduced to correct for suppression of the beam fluence profile by EPID flood field calibration. To determine OAX, relative fluence values were obtained along the cross- and in-plane directions in a 40 x 40 cm² field, by scanning with an IC-10 ion chamber at a depth of 1.5 cm in a Wellhöfer water

152

tank at a source-to-surface distance (SSD) of 100 cm. The OAX values were scaled for their application at SDD. The validity of this approach to transmission measurement was tested by comparing total transmission values obtained with the IC and with the EPID for a 20 x 20 cm² field at SDD at selected locations in the cross- and in-plane directions for steel shot attenuators having thicknesses ranging from 0.5 to 4 cm.

5.2.2.2 Modeling of scatter transmission

Compton scattering is the dominant form of photon interaction at therapy energies, giving rise to secondary electrons and scattered photons. The electron part is mostly absorbed or deflected in the large air gap between the compensator and the detector. But the scattered photon component is not altogether negligible and its contribution has to be accounted for. In an exit dosimetry study by Boellaard *et al.*, it was demonstrated that for air gaps between the patient and detector of more than 50 cm the scattered dose component for an 8 MV beam is less than 5% [Bo, 1997b]. Swindell and Evans have further shown that for a 6 MV beam, the scatter dose component on the central axis for large air gaps increases linearly with field size and the distribution is fairly flat at the detector [Sw, 1996]. The fraction of incident energy fluence scattered from a steel shot compensator positioned at an SCD of 65 cm and striking an EPID at an SED of 140 cm is estimated to be < 5% [Pa, 1999]. For such geometries, it has been shown that the multiple scatter yield is small, and hence the single Compton scatter model of Spies *et al.* was adapted to describe the scatter component of transmission [Sp, 2000]. The model incorporates analytical expressions for Compton scatter, photoelectric absorption, and pair production coefficients (the latter two for beam attenuation calculation) and for the photon energy spectrum. It was originally developed to study scatter from a copper disk in a geometry where the scatterer is in close proximity to the detector and is irradiated by a narrow parallel beam. For our work, the a-Si EPID was considered to be a Compton detector, and the model was modified to reflect our clinical setup.

153

Specifically, the changes were as follows. We used a generic Varian 6 MV photon spectrum calculated using Monte Carlo methods by Sheik-Bagheri and Rogers [Sh, 2001] with minimum and maximum energy cutoff limits of 0.13 and 5.86 MeV, respectively. We also incorporated a radially symmetric beam profile obtained by fitting our ion chamber measurements of OAX. The cast steel shot (99% Fe) filling used in the compensators was taken to be pure iron with a k-shell binding energy of 7.1 keV [Na, 2004]. The composition of the scatterer is required to calculate the total attenuation coefficient, $\mu_{tot}(E)$, using the analytical expressions for photon interactions. A comparison of $\mu_{tot}(E)$ calculated for # J - 827 cast steel mixture and pure iron yielded maximum differences of -1.2% for E < 100 keV and ± 0.2% for E > 100 keV, thus validating this simplification. The $\mu_{tot}(E)$ values calculated analytically for pure iron differ from NIST data [Na, 2004] by -2.1% to 5.3% for 10 keV < E < 400 keV and by -0.8% to 0.6% for 400 keV < E < 6 MeV. Furthermore, as the photon beam entering the compensator is divergent, the primary ray paths are oblique with respect to the CAX, resulting in a reduction of fluence with off-axis distance. After Compton scattering, the deflection angle must be determined with respect to the incident primary ray path. The total scatter was obtained by numerically integrating a Compton scatter kernel over the 3-D shape of the compensator in Cartesian coordinates. The lateral limits of integration x'''_{min}, x'''_{max}, y'''_{min}, and y'''_{max} are the minimum and maximum values at the compensator of the jaw-defined rectangular aperture used for patient treatment (Fig. 5.1). In the beam direction, integration extends from the entrance surface of the steel shot (at z = 0) to the exit surface $t(x'',y'')$. To obtain the spatial distribution of scatter at the detector, we divided the sensitive area of the EPID into 40 x 30 square tiles, each having an area of 1 cm^2. A solid angle fluence correction was also introduced to account for the non-normal incidence of scattered radiation striking the detector.

With these changes, the scatter model was used to calculate a modified scatter to primary ratio for the steel shot compensators,

$$SPR^* = \frac{\phi_s^{comp}(x,y)}{\phi^{open}(CAX)},$$ (5.10)

where $\phi_s^{comp}(x,y)$ is the energy fluence of singly scattered photons at a point (x,y) in the detector plane and $\phi^{open}(CAX)$ is the energy fluence along the CAX for an open field. These quantities can be written as [Sp, 2000]

$$\phi_s^{comp}(x,y) = \phi_0 \cdot \xi_0 \int_{x_{min}^{\prime\prime}}^{x_{max}^{\prime\prime}} dx' \int_{y_{min}^{\prime\prime}}^{y_{max}^{\prime\prime}} dy' \int_0^{t(x',y')} dz' \cdot OAX(x',y') \cdot$$
$$\left\langle f_E(\gamma) \cdot e^{-\mu_{tot}(E) \cdot \ell_{en} -\mu_{tot}(E') \cdot \ell_{ex}} \cdot \frac{\gamma}{d^2} \cdot R(E') \right\rangle$$ (5.11)

and

$$\phi^{open}(CAX) = \phi_0 \cdot \langle R(E) \rangle.$$ (5.12)

Here ξ_0 is the product of electron density and classical electron radius squared (0.1044 cm^{-1} for Fe^{26}), $f_E(\gamma)$ is the Klein-Nishina scatter kernel, γ is the cosine of the photon deflection angle, $\mu_{tot}(E)$ is the total attenuation coefficient, ℓ_{en} is the path length of the incident photon in the attenuator upstream of the point of interaction, ℓ_{ex} is the path length of the scattered photon in the attenuator, d is the distance from the scattering site to the detector, R(E) is the energy response of a Compton detector, and E and E' are the energies of the photon before and after scattering, respectively. ϕ_0 is the incident photon fluence at the CAX. The angular brackets in Eqs. 5.11 and 5.12 denote an average over the normalized photon energy spectrum for 6 MV photons, χ_E, i.e.

$$\langle R(E) \rangle = \int_{E_{min}}^{E_{max}} R(E) \cdot \chi_E \cdot dE,$$ (5.13)

where E_{min} and E_{max} are the minimum and maximum cut-off energies for the spectrum.

The magnitude of scatter varies as a function of compensator thickness and collimator field size. Our initial calculations showed that the maximum scatter contribution to the total transmission at an SED of 140 cm was < 4% for the thickest compensator and largest field size used for measurements. Because of the significant

155

time involved in evaluating the four-dimensional integral in Eq. 5.11, we explored the possibility of modeling the compensator scatter as arising from a flat attenuator of the same volume. As a result of the large distance from compensator to EPID, the SPR^* value calculated with this simplification changed by only ~0.1%. Also, the SPR^* value calculated including the two Lucite plates on either side of the steel shot was found to be no more than 0.2% greater than that calculated when excluding the plates. Consequently, we elected to use the average compensator thickness for scatter calculations and to neglect the Lucite plates, thus saving computation time (decreased from > 30 mins to < 3 mins). The scatter part of transmission can now be written as

$$
\begin{aligned}
T_s(AxB, x, y) &= \frac{R_S^{comp}(AxB, x, y)}{R^{open}(AxB, x, y)} \\
&= \frac{R_S^{comp}(AxB, x, y)}{R^{open}(AxB, CAX)} \times \frac{R^{open}(AxB, CAX)}{R^{open}(AxB, x, y)} = SPR^* \times \frac{1}{OAX(x, y)}.
\end{aligned}
$$

(5.14)

5.2.2.3 Determination of steel shot attenuation coefficient

The remaining parameters required for thickness calculation (in Eqs. 5.2 & 5.3) are $\mu_0(x, y)$, α and κ, the coefficients characterizing primary transmission as a function of steel shot thickness and off-axis distance. Total transmission data was obtained from the set of images (of flat attenuators (0.5 – 4.5 cm thick)) acquired to determine the EPID scatter factors. The EPID readings, which were averaged from two consecutive images, were obtained for selected positions along the beam cross- and in-plane axes for field sizes of 6 x 6, 10 x 10, 20 x 20, and 28 x 28 cm^2 at SDD. The primary transmission component was extracted by subtracting the modeled scatter component from the total transmission, and fit to the exponential form in Eq. 5.2. Photon attenuation by the Lucite plates bounding the steel shot is implicitly included in parameter α. As transmission scanning was performed across the entire length and width of each field, adequate sampling of the off-axis behavior of the linear attenuation coefficient was obtained.

156

5.2.3 Compensators Selected for Measurements

To assess the effectiveness of our thickness measurement method we made radiographic measurements for three sets of attenuators: (i) five flat attenuators of thickness 1, 2, 3, 4, and 4.5 cm; (ii) three test compensators [Me, 2003] in the shape of a wedge, hemisphere, and frustum of pyramid; and (iii) twenty-three clinical compensators (including both digitized and Helax designed compensators) mainly used to treat head and neck sites such as sinus, hypopharynx, larynx, and tongue.

5.3 RESULTS AND DISCUSSION

5.3.1 Transmission Measurements

Figure 5.2 shows the calibration curves for open and steel shot-attenuated fields obtained for the aS500 EPID used in thickness measurement. Average pixel values from the ROI_{CAX} are plotted vs. relative ion chamber readings in RU. As illustrated in the figure, the response of the EPID is similar to that observed in section 4.3.1, i.e. a linear response for open fields and a second-order polynomial behavior for the attenuated fields, because of the spectral sensitivity of the EPID response.

The EPID scatter factors for the aS500 at a SED of 140 cm are shown in Figure 5.3(a). They were found to increase with both attenuator thickness and field size. The spread in scatter factors with thickness is about 5% for the largest field size (28 x 28 cm^2), and becomes smaller with decreasing field size. For this reason we have parameterized the scatter factors for each thickness separately, fitting them to straight lines. Scatter factors for square fields of arbitrary size were obtained from these fits. Figure 5.3(b) shows the scatter factors calculated for the hemispherical test compensator. The fall-off of phantom scatter towards the field edges is clearly visible in the figure.

The total transmission is obtained as a ratio of inferred EPID energy fluence readings for compensated and open fields, calculated using the calibration curves and EPID scatter factors. We found that the average percent difference in transmission as

157

determined by the EPID and IC at 10 locations in a 20 x 20 cm^2 field and for five attenuator thicknesses was 0.13 ± 0.66%.

5.3.2 Modeled Scatter

Employing the analytical scatter model, we determined compensator scatter transmission contributions for use in EPID primary transmission estimation. For a 20 x 20 cm^2 field and a 4 cm thick flat attenuator, the scatter transmission was calculated to be 3.2% of the total transmission on the CAX. At the field edges the scatter transmission dropped to ~70% of that at the CAX. For a 1 cm flat attenuator, the scatter transmission was only half as great. Again for the 4 cm flat attenuator, the scatter component at the CAX for a 5 x 5 cm^2 field was determined to be 7% of that for a 20 x 20 cm^2 field. Even though the contribution of scatter to the total transmission is quite small, the scatter component shows a definite increasing trend with compensator thickness and field size.

5.3.3 Steel Shot Attenuation Coefficient

To obtain the steel shot attenuation coefficient, primary transmission estimates for several field sizes were plotted against off-axis distance for flat attenuators and fit to exponential functions that incorporated beam hardening (Eq. 5.3). Figure 5.4 shows the fits for a 10 x 10 cm^2 field to data obtained at the CAX and at four off-axis positions. In examining the fitted parameters, we observed that the amplitude α and beam hardening coefficient κ were only weakly dependent on off-axis distance andfield size (Fig. 5.5), hence global average values of 0.909 ± 0.005 (1 SD) and 0.029 ± 0.005 cm^{-1} (1 SD), respectively were used. The primary transmission data were then refitted using the fixed α and κ values. Linear attenuation coefficients μ_0 obtained from these fits were found to depend slightly on field size and for larger fields, off-axis location. The data in Fig. 5.6 show that attenuation increases with increasing field size, and also towards the edges of the larger fields due to softening of the beam towards the

158

field edges. The variation in transmission due to obliquity of the beam is negligible, being < 0.4% for the thickest compensator and furthest off-axis position. As a slight change in the value of μ_0 can significantly alter compensator thickness estimates, separate μ_0 values were associated with each field size for which transmission measurements were made. Average values of μ_0 were used for the 6 x 6 and 10 x10 cm^2 fields, and linear fit values vs. OAX distance for the larger two fields. Since the linac beam is presumed to be radially symmetric, the linear attenuation coefficient also possesses radial symmetry.

5.3.4 Thickness Measurements

We have selected four compensators from the three different sets for detailed discussion as these illustrate many of the salient features of the technique. They include the 3 cm flat attenuator, the hemispherical test compensator, a digitized sinus compensator, and a Helax compensator designed to treat neck nodes. Results are presented in the form of plots displaying differences between radiographically determined and intended thicknesses. Thicknesses were calculated on a 4 x 4 pixel tile grid covering the irradiated area and smoothed using a 9-point median filter to reduce noise. A margin of 2 tiles (~6 mm) was removed from all field edges because the smoothing operation is not well defined there. This process also has the advantage that it removes most of the penumbral region, where EPID transmission measurement is less reliable because of spectral effects.

Figure 5.7 shows various plots of the difference between measured and intended thicknesses for the 3 cm flat attenuator irradiated by a 20 x 20 cm^2 field at SDD. An overall picture of the differences is provided in Fig. 5.7(a) in the form of a gray scale image and in Fig. 5.7(b) in the form of a contour plot. The profiles in Fig. 5.7 (c-e) indicate a slight variation in thickness in the center of the attenuator and a drop-off towards the edges, a feature observed for most of the thicker compensators. These features may arise in part because of non-uniform packing of steel shot within the compensator. To explore this, a 1 cm flat compensator was refilled four times in

159

succession and imaged (Table 5.1). Each time it was observed that the packing density was slightly different, leading to different average thicknesses having a variation of 0.6 mm. The fluctuations in the central part of the profiles in Figs. 5.7(c-e) are thought to be caused by a combination of local variations in steel shot density (the granules have a range of sizes), grooves at the bottom of the Styrofoam shell created by the milling bit (~3 mm dia), and image noise. Figure 5.7(f) shows a frequency distribution of differences between measured and intended thicknesses. The mean deviation between measured and intended thickness for this compensator was -0.03 ± 019 mm.

Differences in measured and intended thicknesses for a hemispherical compensator are shown in Figure 5.8. The compensator was irradiated in a 20 x 20 cm^2 field defined at SDD. The thickness of the hemisphere was intended to be 4 cm at the center, falling to 0.3 cm at a radius of 7.5 cm. However, the manually measured depth along the CAX was found to be 3.87 cm and the depths at the four OFR positions were found to be greater than intended by ~1 mm. The Styrofoam slab thickness for this compensator was measured to be 4.9 cm instead of the standard 5 cm for which the milling device was programmed, which partially accounts for the observed thickness reduction along the CAX. The increased thickness off-axis can be likely attributed in part to the ~3 mm diameter of the milling bit. The hole used for filling the mould can be seen at the lower right corner of Fig. 5.8(a) where maximum differences of ~4 mm occurred. The largest differences within the hemispherical shape were seen to be at the center (~-2 mm) and edges (~1.5 mm) of the well, resulting in an average thickness difference of 0.92 ± 1.53 mm (1 SD).

Figure 5.9 displays the differences between measured and intended thickness for a sinus compensator produced by digitizing the patient contour. The dark circular regions of disagreement are caused by holes drilled in the top Lucite plate to hold lead shielding blocks that were mounted on the compensator. These are visible as small glitches in the otherwise smooth profiles (see Fig. 5.9(d) and (e)). The mean deviation between measured and intended thickness for this compensator was 0.26 ± 0.42 mm.

Measured and intended thickness differences for a Helax compensator designed to treat neck nodes are shown in Fig. 5.10. For this compensator there is a very sharp

gradient at the edges of the neck contour where a maximum difference of 8 mm was found; inside the contour the difference was everywhere < 2 mm and mostly <1 mm. The large difference at the edge of the neck contour was investigated by making manual measurements, which confirmed that the milled depth was indeed greater than intended. As for the hemispherical compensator, this difference is thought to arise from the limitation of the finite mill bit size in milling steep gradients. Regions outside the contour had the largest thicknesses; here the Styrofoam was cut to the maximum permissible depth of 4.5 cm. The differences between measured and intended thickness profiles in Fig. 5.10(c)-(e) in areas outside the neck contour are similar in magnitude to those observed for the central region of the hemispherical test compensator. The mean deviation between measured and intended thickness for this compensator was -0.44 ± 1.03 mm.

Finally, Fig. 5.11 displays the mean value ± 1 standard deviation of differences between measured and intended thicknesses for all of the flat, test and clinical compensators studied. For all three groups of compensators, the greatest differences were observed to occur for maximum depths (4.5 cm), at field edges, and along steep thickness gradients. The overall mean thickness differences for the flat, test, and clinical groups were -0.22 ± 0.25 mm, -0.06 ± 0.94 mm, and -0.63 ± 0.74 mm, respectively. From the figure, it can be seen that thickness difference error bars are larger for some compensators than for others. These compensators have the largest thickness gradients and correspondingly, the greatest thicknesses. Lateral positioning inaccuracies in compensator milling and mounting operations are expected to lead to larger differences for compensators having larger thickness gradients.

5.3.5   Compensator Thickness Uncertainties

5.3.5.1 Compensator manufacture

Uncertainties in compensator manufacturing involve both depth (Z axis) variations and lateral shifts (X/Y axes) (Fig. 5.1) in fabrication and mounting.

In our center, long Styrofoam sheets of 5 cm nominal thickness are cut into 25.3 x 25.3 cm^2 slabs in preparation for milling. We measured the thicknesses of ten such slabs sampled over a period of several months and found that they varied from 4.9 cm to 5.2 cm. This variation affects the depth to which the mill bit cuts the slab, resulting in thicknesses that are offset from those intended, as was observed for the hemispherical compensator. From manual measurements of the CAX thickness for our selected set of clinical compensators, we found a mean difference from intended thickness of 0.40 ± 0.41 mm (1 SD). Also, because of variations in the size and shape of the steel granules, their packing density in a compensator can vary with each fill. From the data in Table 5.1, changes in steel shot density are estimated to be < 2.0%. We also observed that for the thickest compensators, over-tightening the Lucite plates on either side of the Styrofoam prior to filling could cause a reduction in cavity thickness arising from compression of the Styrofoam.

Lateral positioning uncertainties are considered to be equal in the X and Y directions. Shifts of up to 0.5 mm in X or Y may occur when positioning the Styrofoam on the milling device to cut the cavity and the guide holes for affixing the Lucite plates. The locations of the holes in the Lucite plates are accurate to within 0.25 mm. Reproducibility in positioning the compensator in the linac accessory mount was assessed using a Lucite tray with a central crosswire. A standard deviation of 0.2 mm in the crosswire location in the plane of the tray was observed for ten consecutive light field measurements. As these positioning uncertainties are independent, we can combine them in quadrature to obtain an overall positioning uncertainty of ~ 0.6 mm (1 SD) in the X or Y direction at SCD.

5.3.5.2 Radiographic measurement

An estimate of the uncertainty inherent in our thickness measurement method can be obtained from Eqs. (5.2) and (5.3). Neglecting beam hardening for simplicity and assuming the remaining variables in the equations are independent, we can write,

162

$$\delta t_P = t_P \times \left[(1/\ln(T_P/\alpha))^2 \cdot \left((\delta T_P/T_P)^2 + (\delta\alpha/\alpha)^2 \right) + (\delta\mu_0/\mu_0)^2 \right]^{0.5}. \qquad (5.15)$$

For measurements made near the CAX in a 20 x 20 cm^2 field we have $\alpha \pm \delta\alpha = 0.909$ $\pm$ 0.005 and $\mu_0 \pm \delta\mu_0 = 0.231 \pm 0.003$ cm^{-1}. If we further assume that the error in calculated scatter transmission is negligible, then uncertainties in primary transmission, T_P, arise solely from uncertainties in total transmission, T_T. The latter can be calculated from our measured data in a straightforward manner using Eqs. (5.8) and (5.9). Estimating uncertainties in this way for our set of flat attenuators, we obtained CAX t $\pm$ δt values of 1.02 $\pm$ 0.03 cm, 2.02 $\pm$ 0.03 cm, 2.99 $\pm$ 0.03 cm, 4.03 $\pm$ 0.03 cm, and 4.34 $\pm$ 0.04 cm. These uncertainty estimates are comparable in magnitude to the observed thickness variations shown in Fig. 5.11(a).

5.4 SUMMARY AND CONCLUSIONS

An algorithm for measuring the two-dimensional thickness profile of a compensator for QC purposes using an a-Si EPID has been presented. This technique enables an end-point check in compensator fabrication to be done via comparison of measured and intended thicknesses. For a set of 31 compensators, measured thicknesses were found to differ from intended values by -0.51 $\pm$ 0.68 mm on average. Furthermore, compensator factors measured using an IC and the EPID agreed to ~1%, providing additional confirmation of the method. Measurement accuracy appears to be quite similar to that reported for a video EPID [Pa, 1999]; both detectors require careful calibration for this particular application.

One area that needs further investigation is the off-axis EPID scatter factor calculation, which is presently done using Day's method for a compensator thickness defined by the primary ray path. Work already underway at our center to model both the radiation and optical components of the EPID point spread function using Monte Carlo methods could provide a means to study the limitations of this approach. We also note that the inclusion of beam hardening in our model for primary transmission (Eq. (5.3)) was found to be important in describing the measured data. In looking at the

thickness measurements as a whole, it seems there is most room for improvement in regions of greatest thickness bounded by thinner regions, as for the hemisphere and neck node compensators (Figs. 5.7 and 5.9). Refinements of the EPID scatter factor calculation may be able to address this shortcoming.

In comparing measured and intended thicknesses, it is essential to be aware of the limitations associated with compensator manufacture and to take these into consideration when assessing the EPID measurement technique. The size of the mill bit (~3 mm dia) and the uncertainties associated with lateral positioning of the Styrofoam block in the mill and between the Lucite plates (~0.6 mm overall) introduce differences in intended thicknesses that are greatest in regions of steep thickness gradient. Such differences, typically up to several mm, are evident for the hemisphere and neck node compensators (Figs. 5.8 and 5.10). For clinical compensators with smaller thickness gradients, the standard deviation in measured thickness is more typically ~0.5 mm (Fig. 5.11(c)), in reasonable agreement with our uncertainty estimates for flat absorbers of 0.3 – 0.4 mm. The flat attenuator data in Fig. 5.11(a) exhibit a mean thickness difference of -0.22 mm and a standard deviation of 0.25 mm. The 1.5 mm difference for the 4.5 cm attenuator, although larger than those for smaller thicknesses, is not unexpected given the flattening of the primary transmission curve at the largest thicknesses (Fig. 5.4). For the clinical compensators in Fig. 5.11(c), the mean difference and standard deviation are larger, -0.63 mm and 0.74 mm, respectively, due to the greater influence of manufacturing and measurement uncertainties for the shaped compensators.

In conclusion, a-Si EPIDs appear to be suitable for two-dimensional compensator thickness measurement. Although uncertainties associated with compensator manufacturing make assessment of thickness measurement accuracy difficult, we estimate that the technique described here is accurate to ~0.5 mm for steel shot compensators of thickness < 4 cm.

164

5.5 APPENDIX

Appendix 5.1: Primary Ray Intersection with the Compensator

For each radiographic measurement of normal thickness $t(x,y)$, the corresponding intended thickness $t_i(x,y)$ must be obtained from the cut file. As illustrated in Fig. 5.12, the appropriate coordinates for thickness lookup, (x'',y''), are defined by the point where the primary ray path intersects the bottom surface of the steel shot layer. For a surface of arbitrary shape, the exit point can be found using numerical iteration.

The initial thickness estimate, t_0, is taken to be the CAX thickness at (x_0,y_0). The algorithm then proceeds to determine the next estimate, t_1, as the thickness at point (x_1,y_1) where the primary ray path intersects the plane of CAX thickness at $z=z_0+t_0$, i.e.

$$(x_1,y_1) = ((x_D - x_0) \times s_1, (y_D - y_0) \times s_1),$$
(A 5.1)

with

$$s_1 = (z_0 + t_0)/ z_D.$$
(A 5.2)

The search for (x'',y'') proceeds iteratively as

$$(x_n,y_n) = ((x_D - x_0) \times s_n, (y_D - y_0) \times s_n),$$
(A 5.3)

with

$$s_n = (z_0 + t_{n-1})/ z_D.$$
(A 5.4)

The iteration is terminated when

$$|t_n - t_{n-1}| < \varepsilon.$$
(A 5.5)

For our compensator fabrication method, we chose $\varepsilon = 0.2$ mm as an appropriate stopping criterion.

165

TABLE 5.1

Changes in the weight of steel shot associated with four consecutive filling trials of a 1 cm flat attenuator, and the average thickness for each obtained from EPID measurements within a central 16 x 16 cm^2 ROI. The thickness uncertainty represents one standard deviation in the ROI.

Trial #	Weight ($\pm$ 2) (g)	Measured thickness (cm)
1	1615	1.12 $\pm$ 0.01
2	1602	1.09 $\pm$ 0.01
3	1590	1.06 $\pm$ 0.02
4	1585	1.09 $\pm$ 0.02
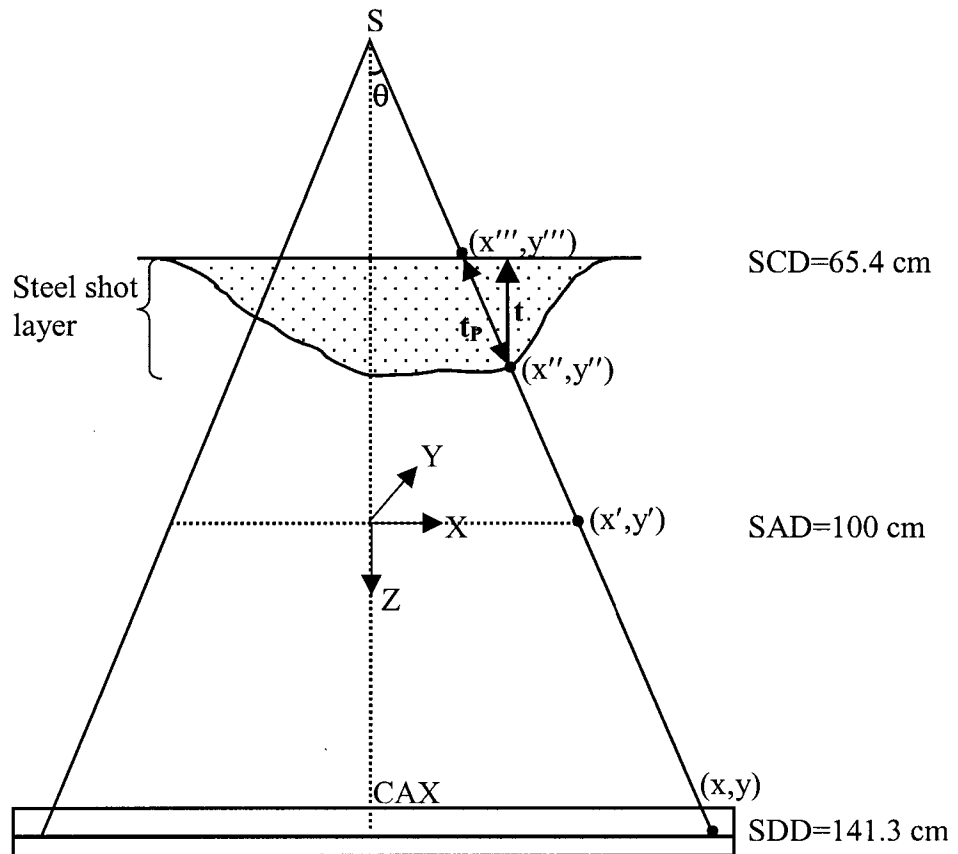
Figure 5.1: The primary ray path thickness, t_p, and the normal thickness, t, calculated from EPID measurements at position (x,y) in the imaging plane. The associated compensator cut file contains normal thicknesses corresponding to different positions (x''',y''') at SCD.
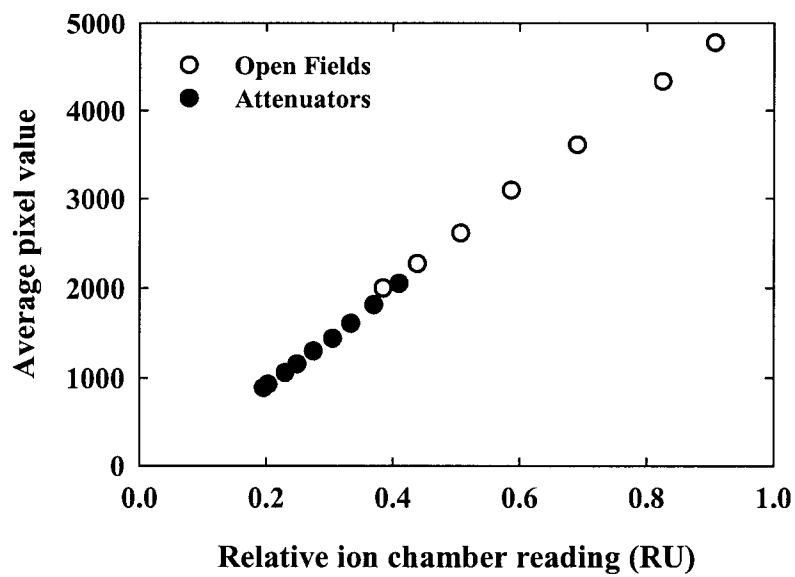
Figure 5.2: aS500 average pixel value at the CAX vs. relative ion chamber reading for a 20 x 20 cm^2 field at SDD. The open field measurements were taken at SED = 105, 110, 120, 130, 140, 150, and 160 cm. The attenuator curve was obtained with flat attenuators of thickness ranging from 0.5 to 4.5 cm in increments of 0.5 cm.
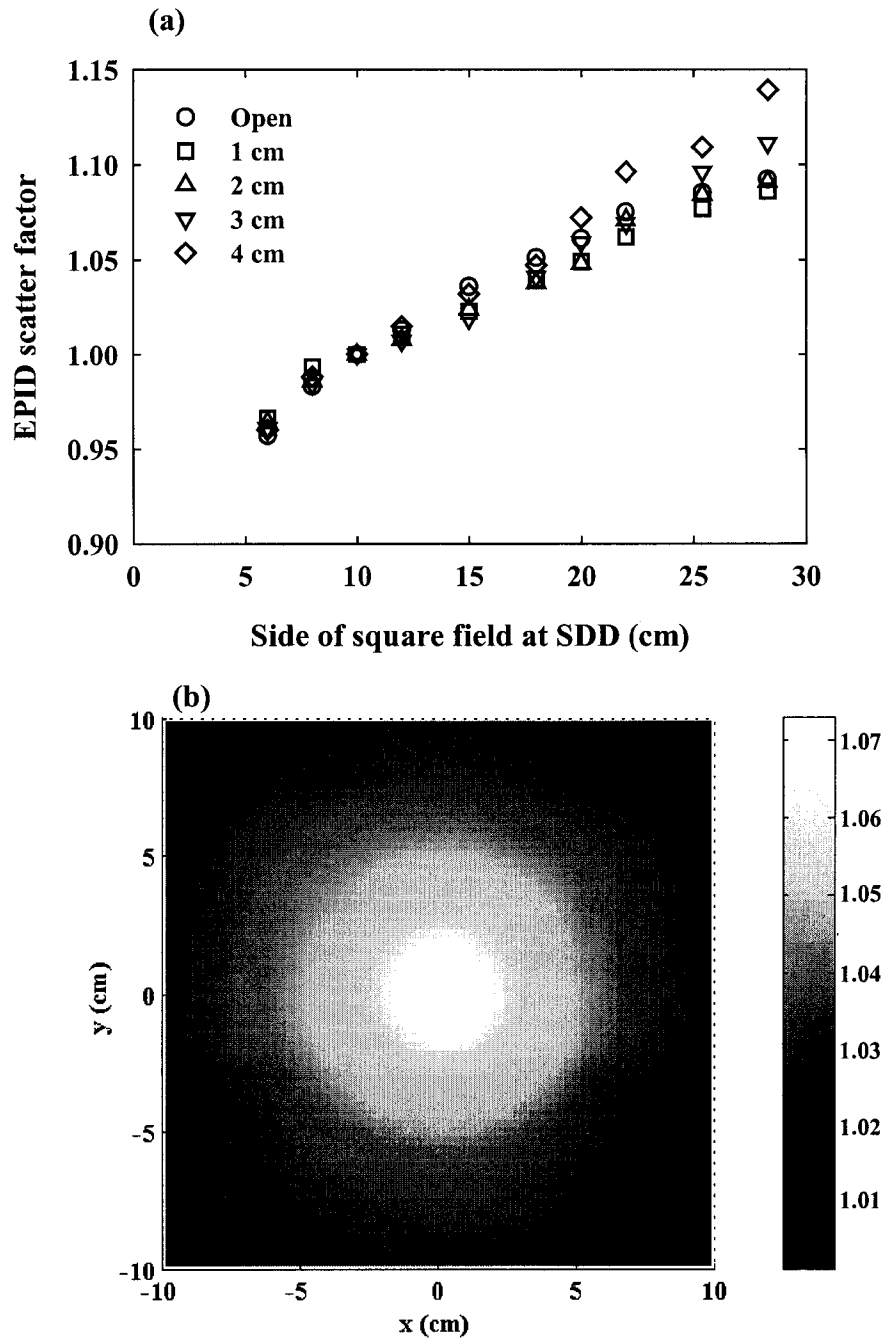
Figure 5.3: (a) EPID scatter factors for open and steel shot attenuated beams, for square fields of size 6 x 6 to 28 x 28 cm^2 at SDD. A linear fit was given to the scatter factor data for each different attenuator thickness. (b) EPID scatter factors calculated for the hemispherical test compensator for a 20 x 20 cm^2 field at SDD.

169
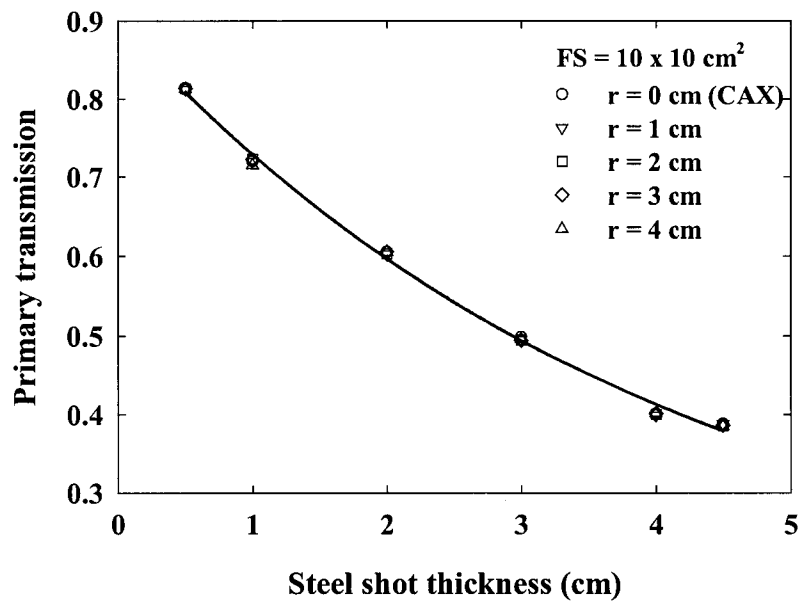
Figure 5.4: Primary transmission data for our 6 MV photon beam in a 10 x 10 cm² field at SDD = 141.3 cm. The different symbols correspond to detector positions at the CAX and at various off-axis distances. The curves (overlapping) represent fits to the data obtained using Eqs. 5.2 and 5.3.
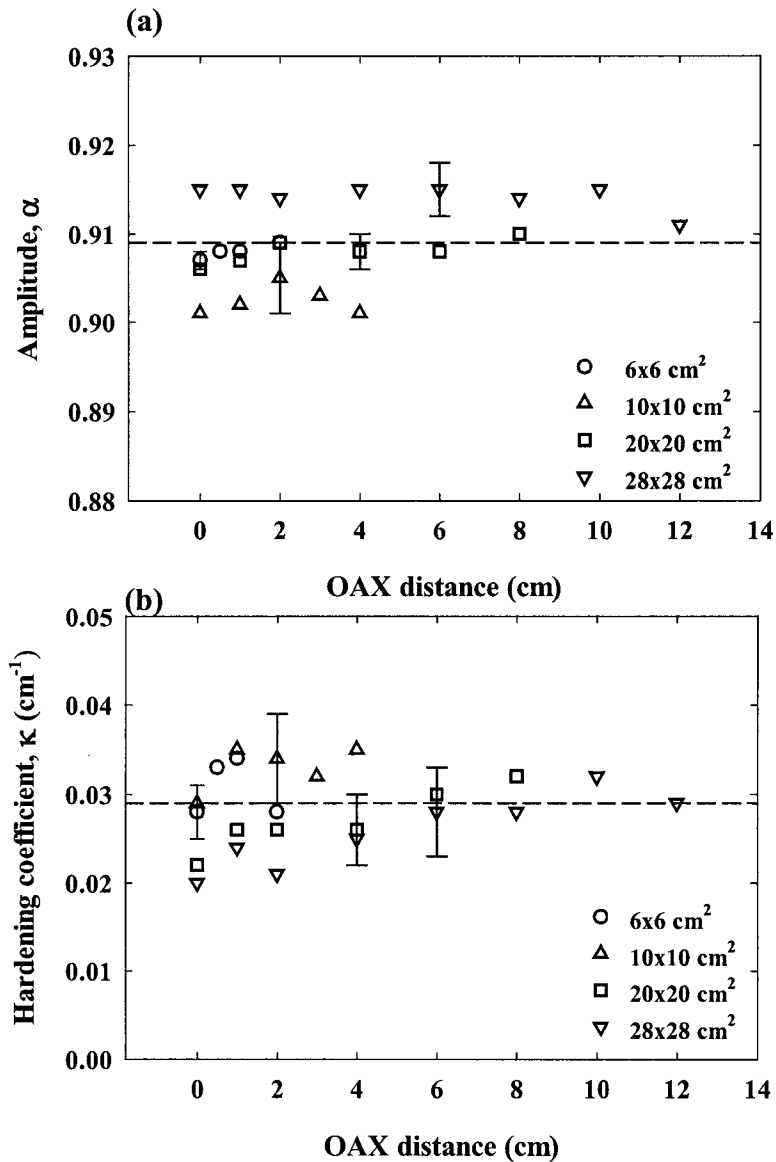
Figure 5.5: Plots of the fitted parameters **(a)** amplitude, α, and **(b)** hardening coefficient, κ, obtained by fitting the primary transmission data with the beam hardening model for increasing field sizes. The error bars on the single data points represent typical fluctuations in α and κ for that particular field size.

171
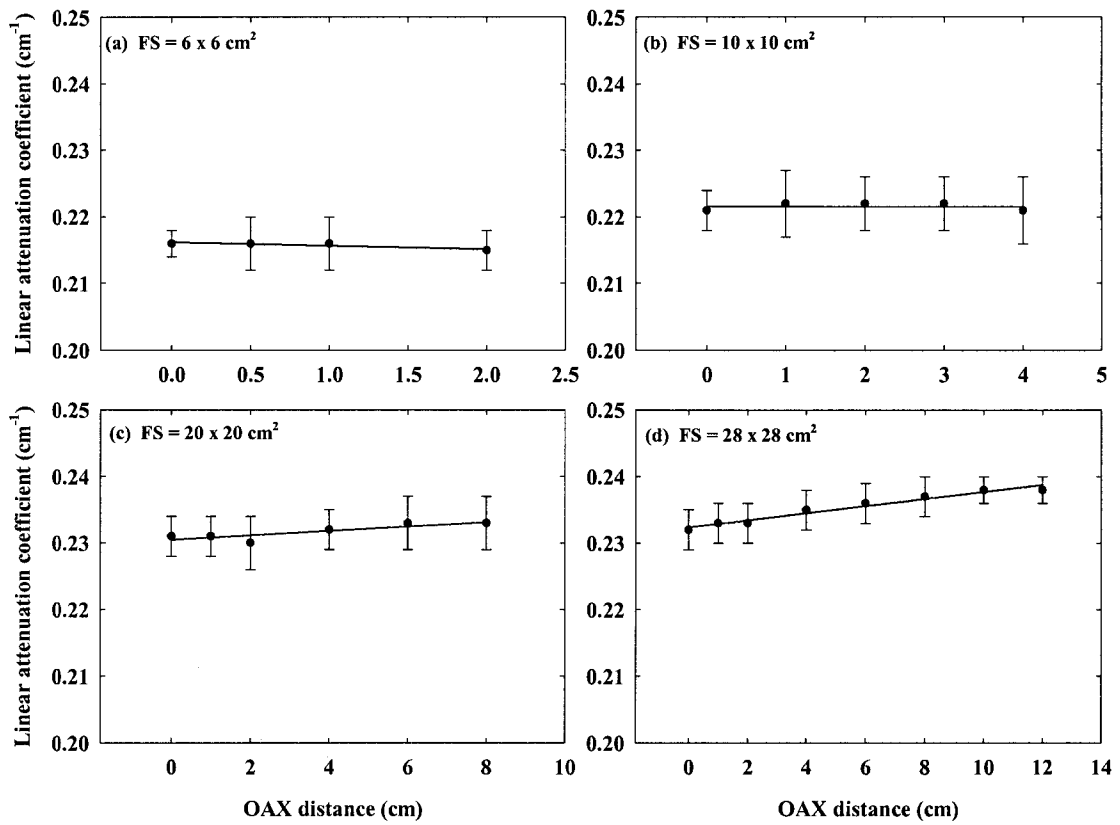
Figure 5.6: Linear least squares fits to steel shot linear attenuation coefficients μ_0 plotted as a function of off-axis distance for different field sizes. The error bars represent the uncertainties in μ_0 values (1 s.d.) reported by the fitting software (Sigma Plot, SPSS Inc., Chicago, IL).

172
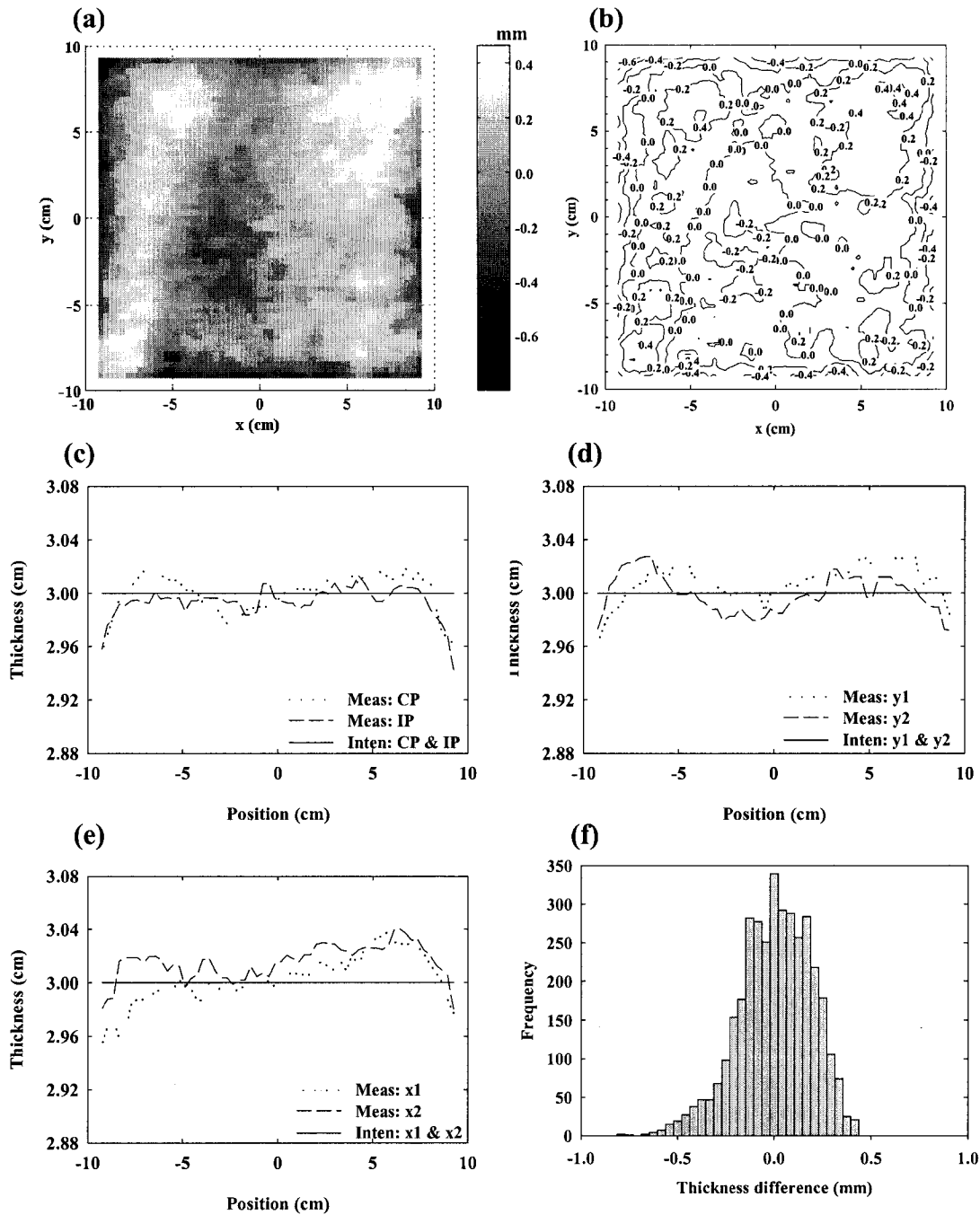
Figure 5.7: Measured minus intended thickness **(a)** surface and **(b)** contour plots for a 3 cm flat attenuator for a field size of 20 x 20 cm^2 at SDD, **(c)** Cross- and in-plane profiles of measured and intended thicknesses along x = 0 and y = 0, **(d)** Thickness profiles along y1 = -5 cm and y2 = +5 cm, **(e)** Thickness profiles along x1 = -5 cm and x2 = +5 cm, and **(f)** Frequency plot of the thickness difference distribution. Thickness differences range from -0.79 to +0.46 mm; the mean value = 0.03 ± 0.19mm.

173
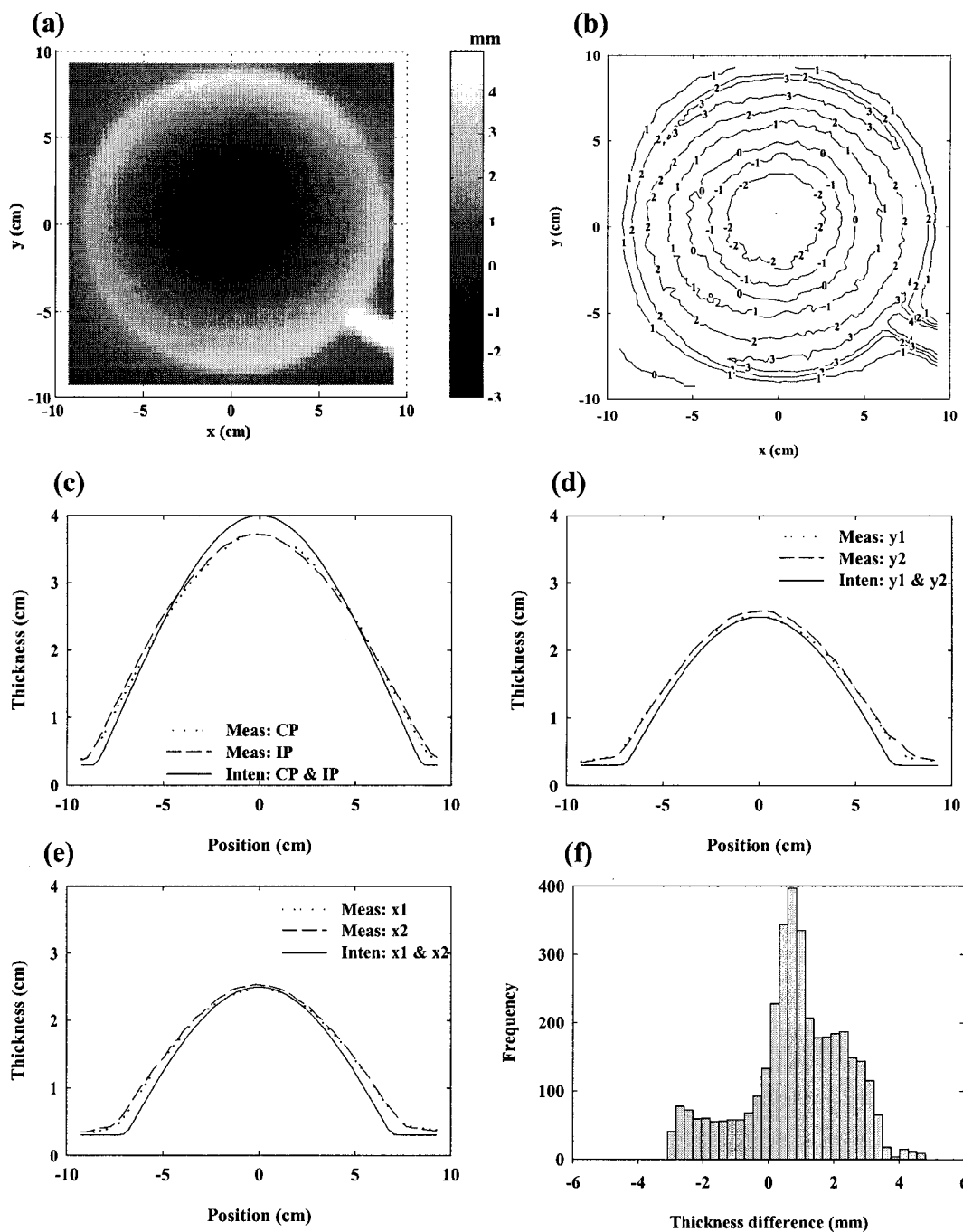
Figure 5.8: Measured minus intended thickness difference **(a)** surface and **(b)** contour plots for a hemispherical compensator for a field size of 20 x 20 cm^2 at SDD, **(c)** Cross- and in-plane profiles of measured and intended thicknesses along x = 0 and y = 0, **(d)** Thickness profiles along y1 = -5 cm and y2 = +5 cm, **(e)** Thickness profiles along x1 = -5 cm and x2 = +5 cm, and **(f)** Frequency plot of the thickness difference distribution. Thickness differences range from -3.00 to +4.70 mm; the mean value = 0.92 ± 1.53 mm.

174
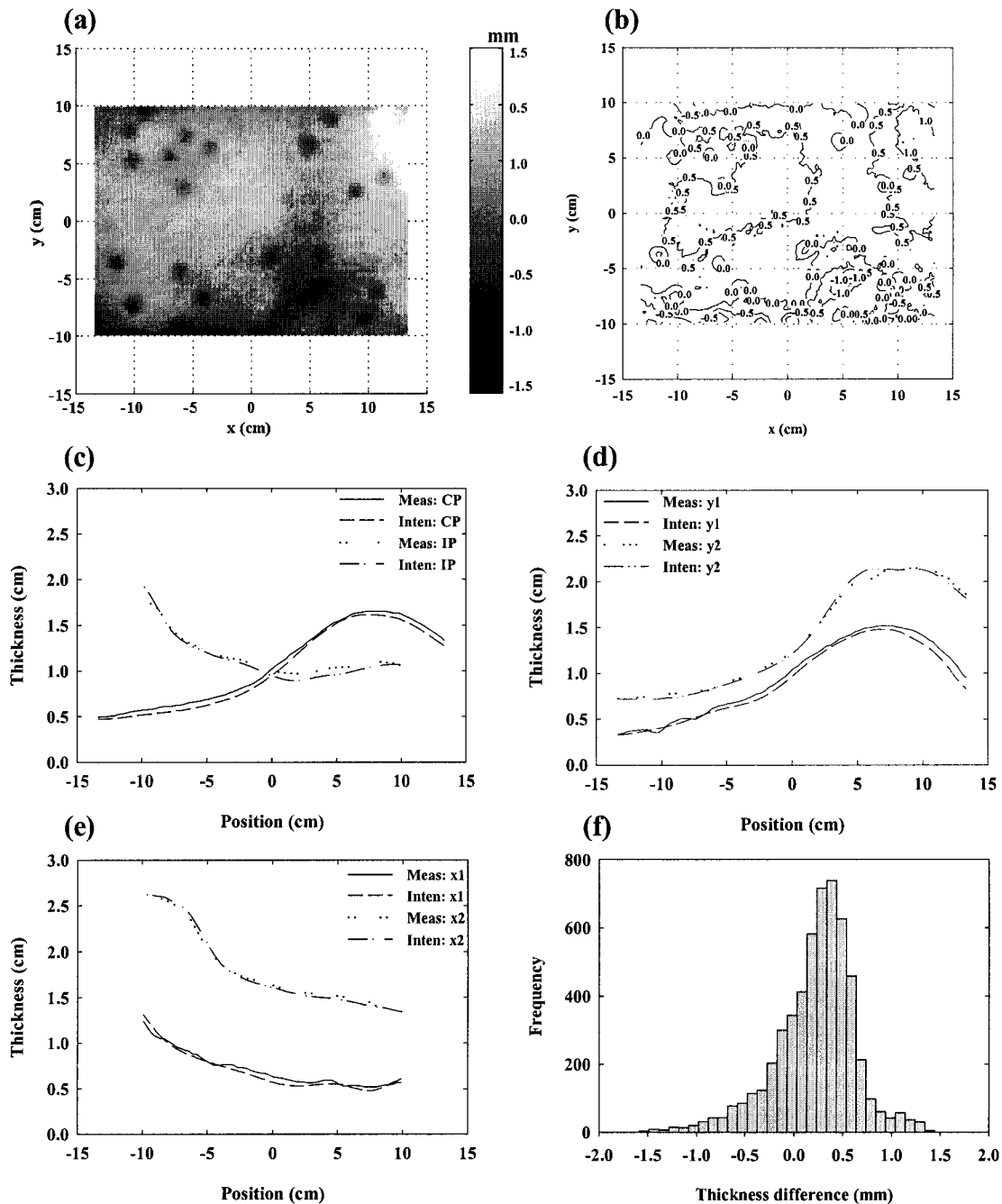
Figure 5.9: Measured minus intended thickness difference **(a)** surface and **(b)** contour plots for a sinus compensator for a field size of 28 x 21 cm^2 at SDD, **(c)** Cross- and in-plane profiles of measured and intended thicknesses along x = 0 and y = 0, **(d)** Thickness profiles along y1 = -5 cm and y2 = +5 cm, **(e)** Thickness profiles along x1 = -7 cm and x2 = +7 cm, and **(f)** Frequency plot of the thickness difference distribution. Thickness differences range from -1.58 to +1.50 mm; the mean value = 0.26 ± 0.42 mm.
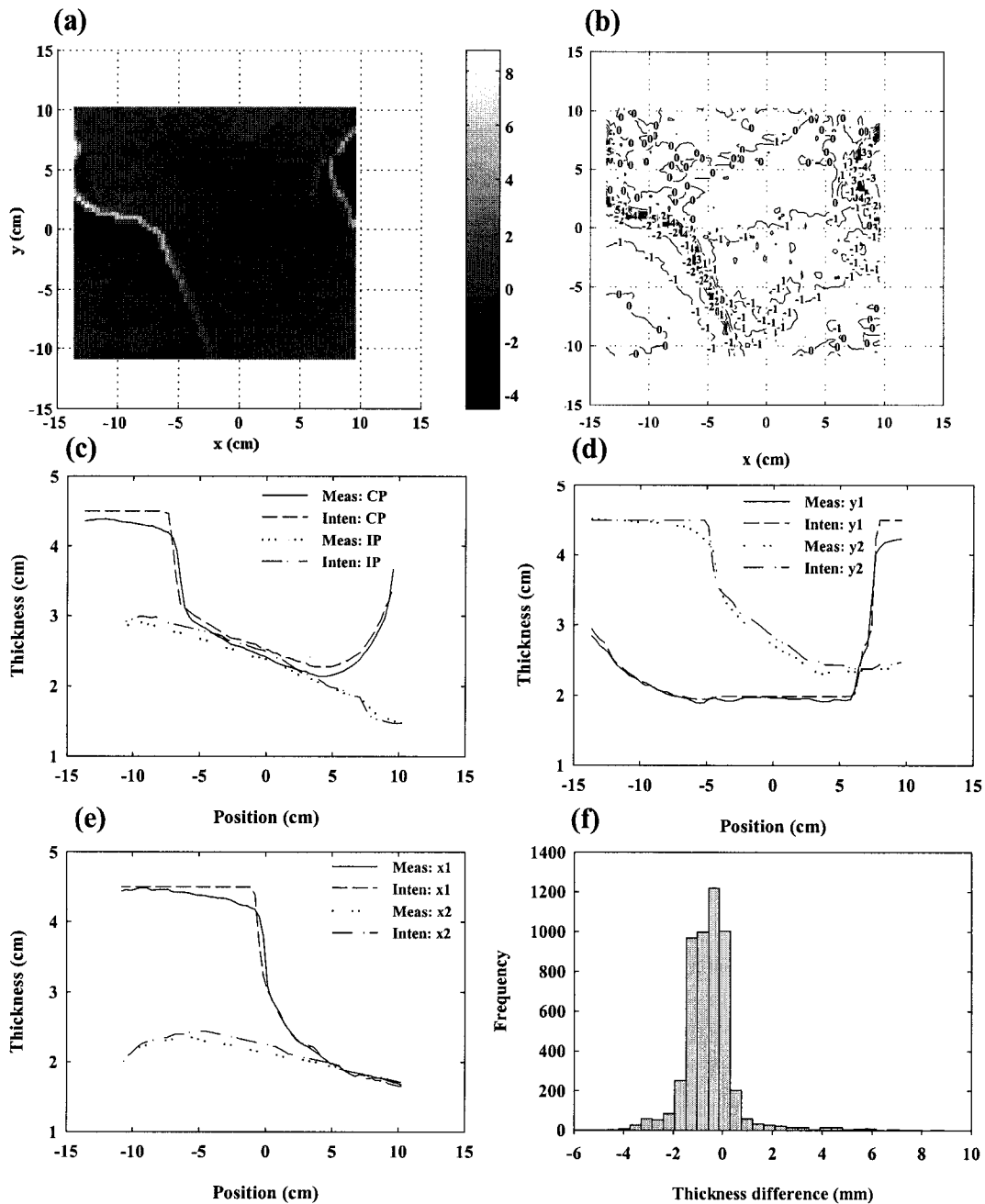
Figure 5.10: Measured minus intended thickness difference **(a)** surface and **(b)** contour plots for a Helax compensator for an asymmetric field of size 26 x 24 cm^2 at SDD, **(c)** Cross- and in-plane profiles of measured and intended thicknesses along x = 0 and y = 0, **(d)** Thickness profiles along y1 = -6 cm and y2 = +5 cm, **(e)** Thickness profiles along x1 = -7 cm and x2 = +5 cm, and **(f)** Frequency plot of the thickness difference distribution. Thickness differences range from –4.46 to +8.76 mm; the mean value = -0.44 ± 1.03 mm.

176
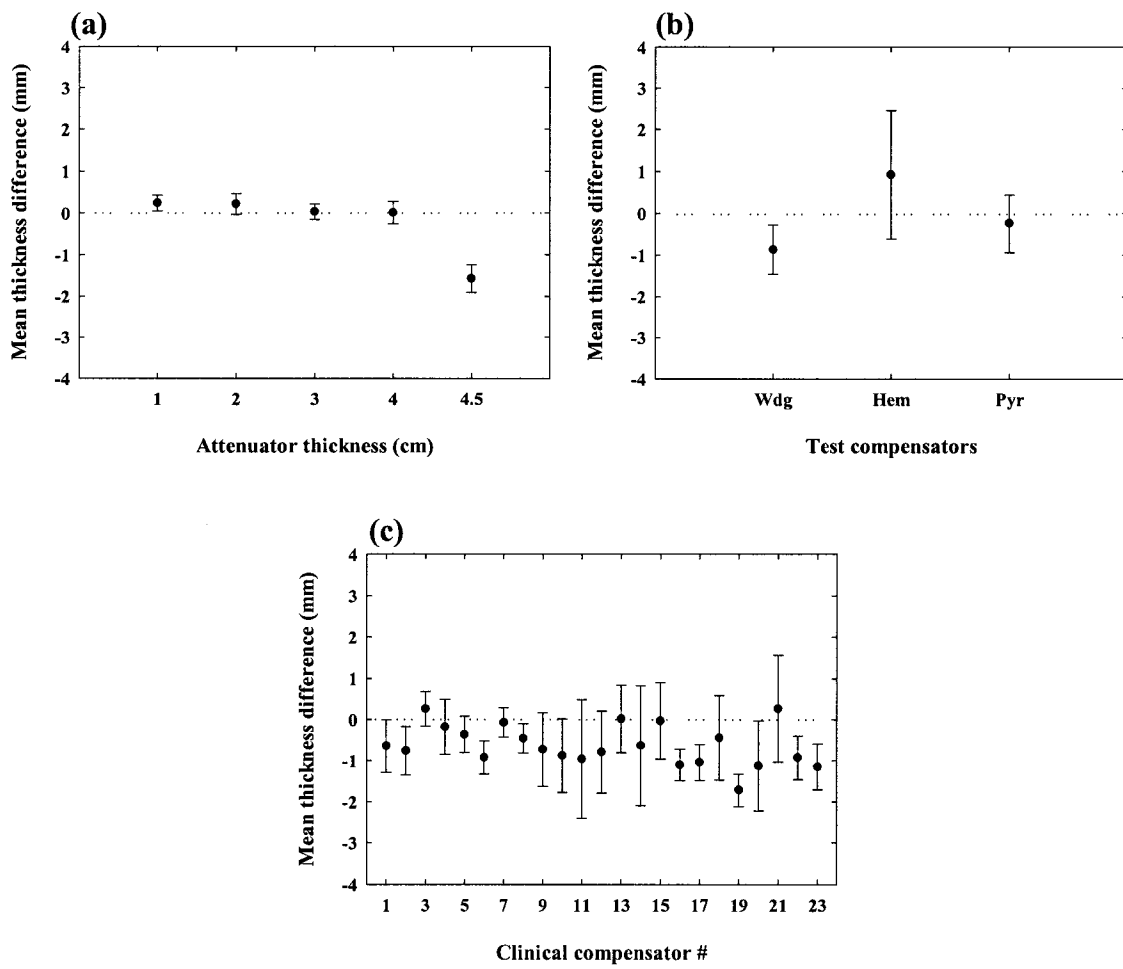
Figure 5.11: Mean ± 1 SD of differences between measured and intended thickness for **(a)** flat absorbers, **(b)** test compensators, and **(c)** clinical compensators.

177
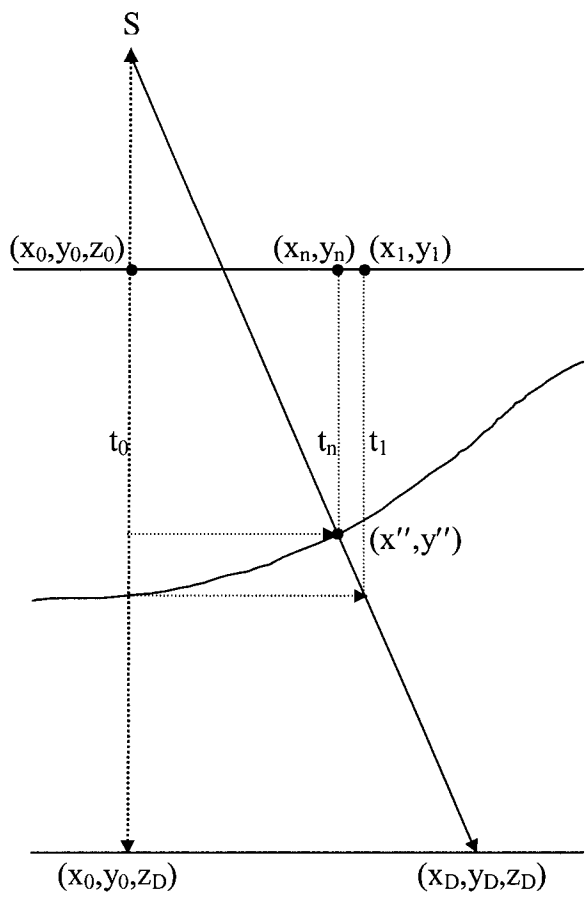
Figure 5.12: Illustration of parameters for our iterative search algorithm to determine ray exit points at the bottom of the steel shot layer in the compensator.

178

5.6 REFERENCES

[Bo, 1997b]   R. Boellaard, M. van Herk, and B. J. Mijnheer, "A convolution model to convert transmission dose images to exit dose distributions," Medical Physics. **24**, 189-199 (1997).

[Ch, 2001]   J. Chang, G. S. Mageras, C. C. Ling, and W. Lutz, "An iterative EPID calibration procedure for dosimetric verification that considers the EPID scattering factor," Medical Physics. **28**, 2247-2257 (2001).

[Da, 1950]   M. J. Day, "A note on the calculation of dose in x-ray fields," British Journal of Radiology. **23**, 368-369 (1950).

[Lo, 1996b]   D. A. Low, Z. Li, and E. E. Klein, "Verification of milled two-dimensional photon compensating filters using an electronic portal imaging device," Medical Physics. **23**, 929-938 (1998).

[Me, 2003]   G. V. Menon and R. S. Sloboda, "Compensator quality control with an amorphous silicon EPID," Medical Physics. **30**, 1816-1824 (2003).

[Na, 2004]   National Institute for Standards and Technology (NIST) Website (http: // physics . nist . gov / PhysRefData / Xcom / Text / XCOM . html) - XCOM: Photon Cross Sections Database.

[Pa, 1999]   K. L. Pasma, M. Kroonwijk, E. B. van Dieren, A. G. Visser, and B. J. M. Heijmen, "Verification of compensator thicknesses using a fluoroscopic electronic portal imaging device," Medical Physics. **26**, 1524-1529 (1999).

[Po, 2000a]   PortalVision™ aS500 Rel. 6 Reference Manual, Varian Medical Systems Inc., June 2000.

[Sh, 2001]   D. Sheikh-Bagheri, and D. W. O. Rogers, "Monte Carlo calculation of nine megavoltage photon beam spectra using the BEAM code," Medical Physics. **28**, 2247-57 (2001).

[Sp, 2000]   L. Spies, P. M. Evans, M. Partridge, V. N. Hansen, and T. Bortfeld, "Direct measurement and analytical modeling of scatter in portal imaging," Medical Physics. **27**, 462-471 (2000).

[Sw, 1996]   W. Swindell and P. M. Evans, ''Scattered radiation in portal images: A Monte Carlo simulation and a simple physical model,'' Medical Physics. **23**, 63–73 (1996).

[Yu, 1997]   M. K. Yu, R. S. Sloboda, and B. Murray, "Linear accelerator photon beam quality at off-axis points," Medical Physics. **24**, 233-239 (1997).

CHAPTER 6: SUMMARY AND FUTURE WORK

The success of a radiotherapy treatment is in many cases profoundly dependent on both the prescribed treatment plan and the accuracy with which it is delivered. Several investigators have delved into the latter problem, first using film, and later, EPIDs, to improve patient setup geometry. More recently, the use of EPIDs has been extended for dosimetric verification. Dosimetric studies with a-Si EPIDs were in their infancy at the beginning of this project. In the introductory chapter we expressed our hope that the present work to investigate the suitability of the aS500 EPID for compensator verification might constitute a translational step in the use of a-Si EPIDs for dose measurement. This final chapter summarizes the progress achieved in reaching the objectives of the thesis as hypothesized in the introduction. The chapter also briefly discusses noteworthy challenges and constraints encountered during the course of the work, and indicates research directions for future work in this area.

6.1 SUMMARY

In this research with an aS500 EPID, the key objectives were:

- To understand the system design and imaging parameters of the Varian aS500 EPID: What acquisition modes and imaging parameters should be selected for high-quality images? How do the detector response and image quality change with time? What are the best parameters for dosimetric operation?

- To explore the feasibility of dosimetric measurements for compensators: How to measure and characterize the relationship between EPID response and incident energy fluence? How to design a protocol, which would use the EPID as an ion chamber replacement for compensator QC?

- To perform transmission dosimetry and compensator thickness measurements with the EPID: How to design a procedure to obtain primary transmission from EPID images? How to relate compensator thickness to primary transmission?

181

- To identify limitations and uncertainties associated with the above studies.

The questions associated with each objective were answered in two broad categories of study – one was a performance evaluation of the EPID and the other its dosimetric application.

Our initial work to understand and assess the operation of the aS500 EPID was successful in identifying suitable values of user-selectable parameters for dosimetry [Sec. 2.4]. The imaging performance and stability study revealed consistency of image quality and a stable radiation response, suggesting the EPID's potential for quantitative dosimetric applications [Sec. 3.3]. Hence we proceeded to investigate its suitability as a quality control tool for clinical compensator verification.

Characterization of the a-Si EPID radiation response was accomplished by building on earlier work for other types of EPID reported in the literature. We developed procedures for EPID dose calibration and scatter factor determination enabling energy fluence measurement with the EPID. Pixel values were related to energy fluences measured with an ion chamber via calibration curves determined for a fixed field size. Even though the a-Si EPID is generally considered to have a linear dose response, it was observed that calibration curves obtained by placing attenuators in the beam had a mildly quadratic shape because of the detector's sensitivity to the photon spectrum, necessitating the measurement of separate calibration curves for open and attenuated beams [Sec. 4.3.1]. To employ the calibration curves for other field sizes, EPID scatter factors were determined using an iterative algorithm. The EPID scatter factors were also measured for both open and attenuated fields, and were found to be dependent on attenuator thickness, source-to-detector distance, and field size [Sec. 4.3.2].

Using the above formalism to convert EPID pixel values to energy fluence readings, we employed the aS500 EPID to investigate an alternative clinical technique for steel shot compensator QC. At our center, this procedure has been conventionally performed using an ion chamber in a water equivalent phantom, and involves measurement of the compensator factor and four off-axis fluence ratios. The suitability

of the EPID-based approach was verified by evaluating several test and clinical compensators. The results indicate that the EPID is capable of reproducing ion chamber measurements to within 2% on average [Sec. 4.3.3]. Hence the EPID can be used as an ion chamber replacement device to perform compensator verification in the clinic, with attendant savings in time and effort.

We further explored the potential use of the aS500 EPID to verify the accuracy of compensator fabrication by radiographically determining compensator thickness on a two-dimensional grid. The main approach involved making total transmission measurements with the EPID, subtracting a calculated estimate of the scatter contribution, and inferring compensator thickness from the resultant primary transmission using a primary transmission model. The results indicate that thicknesses can be estimated with the EPID to an accuracy of ~0.5 mm of steel shot for compensator thicknesses < 4 cm, after accounting for uncertainties associated with compensator manufacturing [Sec. 5.3.4 & 5.3.5].

There were some important observations made during the course of our work with the aS500 EPID that are worth restating. First, one has to be aware that the EPID hand controller displays distances to the top of the detector stack, whereas the imaging plane of the EPID is 1.3 cm downstream. This is not a concern in treatment setup verification but has to be accounted for interpreting energy fluence measurements. Also, the EPID was found to be sensitive to the incident photon spectrum, showing a different response with different types of attenuators in its path. Hence we recommend that when using an a-Si EPID for dosimetry, dose calibration should be done with the same attenuator material that will be present in subsequent measurements [Sec. 4.3.1]. For the most part, the EPID demonstrated good pixel response stability during the period of study, although we occasionally observed slight changes. One reason for this was that the dose calibration was prone to drift over an extended period of time. To overcome this problem, we suggest that it is desirable to update the pixel-to-dose response relation at least quarterly. Another reason was that the image acquisition timing was intermittently premature, whereby aS500 images were occasionally acquired ahead of the specified time (particularly for the 0-50%-0 acquisition mode),

183

resulting in a reduction in pixel value of up to 4% for consecutive images taken with identical setup parameters. Our workaround here was to look at the acquisition time of all images and eliminate those found to be premature. As regards the steel shot compensators examined, we observed non-negligible variations in their physical properties arising from fabrication and mounting uncertainties such as positioning in the milling device and linac, the finite size of the milling tool, non-uniform packing of the steel shot and variability in the thickness of the Styrofoam slabs. Such uncertainties complicate the assessment of accuracy of EPID-based thickness estimates, and have to be accounted for in the analysis.

6.2 FUTURE WORK

Although several issues could not be fully addressed and evaluated within the limited scope of the present work, a number of promising insights have emerged that could be explored to improve and build on our work in future research.

One potential task is to evaluate the accuracy of our off-axis EPID scatter factor estimates that were calculated using Day's method. Although this approach is pragmatic and appeared to generate reasonable values, an independent verification of the factors was not performed. A Monte Carlo study currently in progress at our center to model the blur kernel of the aS500 EPID could provide such verification, since incident energy fluence may be more readily predicted by first deconvolving the blur from the image. This latter method could prove to be a more robust approach to EPID-based dosimetry, and could help to identify any limitations inherent in the present method.

While earlier types of EPID have been used to measure energy fluence transmitted by compensators [Lo, 1996b], it would be interesting to expand our thickness estimation work to include other beam modifiers such as wedges. Furthermore, extending the comparison of energy fluence to include estimates generated by a treatment planning system would enable a check of the consistency between planned and delivered fluences to be done. In such an approach, the EPID

184

measured fluence could be separated into primary and scatter components for detailed comparison purposes.

As our methodology for compensator QC provides a fast measurement that can easily be integrated into clinical practice, it should provide a practical means to verify recently developed innovative treatments such as those using multifield modulators for IMRT, where a single, rotable compensator delivers multiple fields [Od, 2004]. Although developed for a 6 MV photon beam (which yields good radiographic contrast), the method could also be extended to other beam energies. Such extension would also assist in verifying the scope of the methodology in other contexts than the one for which it was developed.

Finally, future work could also employ an a-Si EPID to study changes in the dose distribution brought about by organ motion. In conjunction with the EPID's capability to track the motion of the organ with implanted markers during treatment [Ne, 2001], variations in the associated transmission dose can be measured and related to changes in delivered dose. In this case the methodology is being extended to tissue as the attenuating medium, and scatter factors would have to be remeasured for various thicknesses of patient tissue equivalent material in place of steel shot. The study should also consider a means to incorporate tissue inhomogeneities in the patient. The same idea can also be used to assess consistency in inter-fractional dose delivery by interpreting differences in the measured transmission dose image from one treatment fraction to the next, and from an intended transmission dose image. Such verification of the accuracy of dose delivery can assist in improving understanding of the variability inherent in clinical treatment, and consequently lead to more efficacious treatment techniques.

These future endeavors can be implemented by utilizing some of the tools developed in this work such as the calibration curves, EPID scatter factors, and primary transmission model. With renewed interest in the use of custom compensators for conformal therapy, the demonstrated approach to compensator transmission and thickness measurement can prove useful as a fast verification tool. This same approach can be extended to other beam modifiers (wedges, tissue, etc.), although it is important

to note that the tools developed here will need to be adapted to each application (e.g. for patient transmission dosimetry, a scatter model that accounts for multiple scattering is likely required). Hence, the methodology developed in this thesis for compensators can serve as a foundation for further work in the area of radiotherapy dose delivery verification.

6.4 REFERENCES

[Lo, 1996b]   D. A. Low, Z. Li, and E. E. Klein, "Verification of milled two-dimensional photon compensating filters using an electronic portal imaging device," Medical Physics. **23**, 929-938 (1998).

[Ne, 2001]   A. J. Nederveen, J. J. W. Lagendijk, and P. Hofman, "Feasibility of automatic marker detection with an a-Si flat-panel imager," Physics in Medicine and Biology. **46**, 1219-30 (2001).

[Od, 2004]   J. C. O'Daniel, L. Dong, D. A. Kuban, H. Liu, N. Schechter, S. L. Tucker, and I. Rosen, "The delivery of IMRT with a single physical modulator for multiple fields: A feasibility study for paranasal sinus cancer," International Journal of Radiation Oncology Biology Physics. **58**, 876-887 (2004).

BIBLIOGRAPHY

L. E. Antonuk, J. Boudry, W. Huang, D. L. McShan, E. J. Morton, M. J. Longo, and R. A. Street, "Demonstration of megavoltage and diagnostic x-ray imaging with hydrogenated amorphous silicon arrays," Medical Physics. **19**, 1455-1466 (1992).
p: 3, 9

L. E. Antonuk, J. Yorkston, W. Huang, J. H. Siewerdsen, and R. A. Street, "Considerations for high frame rate operation of two dimensional a-Si:H imaging arrays," Materials Research Society Symposium. Proceedings **297**, 945-950 (1993).
p:9

L. E. Antonuk, J. Yorkston, W. Huang, H. Sandler, J. H. Siewerdsen, and Y. El-Mohri, "Megavoltage imaging with a large-area, flat-panel, amorphous silicon imager," International Journal of Radiation Oncology Biology Physics. **36**, 661-672 (1996).
p: 7

L. E. Antonuk, Y. El-Mohri, J. H. Siewerdsen, J. Yorkston, W. Huang, and V.E. Scarpine, "Empirical investigation of the signal performance of a high-resolution, indirect detection, active matrix flat-panel imager (AMFPI) for fluoroscopic and radiographic operation," Medical Physics. **24**, 51-70 (1997).   *p: 48*

L. E. Antonuk, Y. El-Mohri, W. Huang, K-W Jee, J. H. Siewerdsen, M. Maolinbay, V. E. Scarpine, H. Sandler, and J. Yorkston, "Initial performance evaluation of an indirect-detection, active matrix flat-panel imager (AMFPI) prototype for megavoltage imaging," International Journal of Radiation Oncology Biology Physics. **42**, 437-454 (1998).   *p: 9*

L. Antonuk, "Electronic portal imaging devices: a review and historical perspective of contemporary technologies and research," Physics in Medicine and Biology. **47**, R31-R65 (2002).   *p: 6, 9, 10, 88*

P. S. Basran, W. Ansbacher, G. C. Field, B. R. Murray, "Evaluation of optimized compensators on a 3D planning system," Medical Physics. **25**, 1837-1844 (1998).
p: 103

J. Bijhold, K. G. A. Gilhuijs, and M. van Herk, "Automatic verification of radiation field shape using digital portal images." Medical Physics. **19**, 1007-1014 (1992). *p:9*

J-P. Bissonnette, I. A. Cunningham, and P. Munro, "Optimal phosphor thickness for portal imaging," Medical Physics. **24**, 803-814 (1997).   *p:7, 91*

R. J. Boge, R. W. Edland, and D. C. Matthes, "Tissue compensators for megavoltage radiotherapy fabricated from hollowed Styrofoam filled with wax", Radiology. **111**, 193-198 (1974).   *p:12*

A. L. Boyer, "Compensating filters for high energy X rays," Medical Physics. **9**, 429-433 (1982).   *p:103*

T. Bortfeld, J. Bürkelbach, R. Boesecke, and W. Schlegel, "Methods of image reconstruction from projections applied to conformation radiotherapy," Physics in Medicine and Biology. **35**, 1423–1443 (1990). *p:1*

A. L. Boyer, L. Antonuk, A. Fenster, M. van Herk, H. Meertens, P. Munro, L. E. Reinstein, and J. Wong, "A review of electronic portal imaging devices (EPIDs)," Medical Physics. **19**, 1-16 (1992). *p: 6, 8, 17*

J. M. Boudry and L. E. Antonuk, "Radiation damage of amorphous silicon, thin-film, field effect transistors," Medical Physics. **23**, 743-754 (1996). *p: 9*

R. Boellaard, M. van Herk, H. Uiterwaal, and B. J. Mijnheer," Two-dimensional exit dosimetry using a liquid filled electronic portal imaging device and a convolution model," Radiotherapy and Oncology. **44**, 149-157 (1997). *p: 4, 10*

R. Boellaard, M. van Herk, and B. J. Mijnheer, "A convolution model to convert transmission dose images to exit dose distributions," Medical Physics. **24**, 189-199 (1997). *p: 148*

R. Boellaard, M. Essers, M. van Herk, and B. J. Mijnheer, "New method to obtain the midplane dose using portal in vivo dosimetry," International Journal of Radiation Oncology Biology Physics. **41**, 465-474 (1998). *p: 5, 15*

A. Brahme, "Accuracy requirements and quality assurance of external beam therapy with photons and electrons," Acta Oncologica. Supplement **1**, Chapter 2:9–15 (1988). *p: 1*

A. Brahme, "Optimization of stationary and moving beam radiation therapy techniques," Physics in Medicine and Biology. **12**, 129–140 (1988). *p: 1*

A. Brahme, "The need for accurate target and dose specifications in conventional and conformal radiation therapy: an introduction," Acta Oncologica. **36**, 789-791 (1997). *p: 1*

E. L. Chaney, T. J. Cullip, and T. A. Gabriel, "A Monte Carlo study of accelerator head scatter," Medical Physics. **21**, 1383-1390 (1994). *p: 112*

J. Chang, G. S. Mageras, C. C. Ling, and W. Lutz, "An iterative EPID calibration procedure for dosimetric verification that considers the EPID scattering factor," Medical Physics. **28**, 2247-2257 (2001). *p: 106, 110, 111, 147*

C. L. Creutzberg, V. G. M. Althof, M. de Hoog, A. G. Visser, H. Huizenga, A. Wijnmalen, and P. C. Levendag, "A quality control study of the accuracy of patient positioning in irradiation of pelvic fields. International Journal of Radiation Oncology Biology Physics. **34**, 697–708 (1996). *p: 4*

J. R. Cunningham, D. J. Wright, H. P. Webb, I. J. Rawlinson, and P. M. K. Leung, " A semi-automatic cutter for compensating filters," International Journal of Radiation Oncology Biology Physics. **1**, 355-358 (1976). *p:12*

A. Curtin-Savard and E. B. Podgorsak, "An electronic portal imaging device as a physics tool," Medical Dosimetry. **22**, 101-105 (1997). *p: 5*

M. J. Day, "A note on the calculation of dose in x-ray fields," British Journal of Radiology. **23**, 368-369 (1950). *p: 112, 147*

R. T Droege, "A practical method to routinely monitor resolution in digital images," Medical Physics. **10**, 37-43 (1983). *p: 90*

D. G. Drake, D. A. Jaffray, and J. W. Wong, "Characterization of a fluoroscopic imaging system for kV and MV radiography," Medical Physics. **27**, 898-905 (2000). *p: 7*

A. Dutreix, "When and how can we improve precision in radiotherapy," Radiotherapy & Oncology. **2**, 275-292 (1984). *p: 2*

F. Ellis, E. J. Hall, and R. Oliver, "A compensator for variations in tissue thickness for high energy beams," British Journal of Radiology. **32**, 421-422 (1959). *p: 12, 103*

Y. El-Mohri, L. E. Antonuk, J. Yorkston, K. -W. Jee, M. Maolinbay, K. L. Lam, and J. H. Siewerdsen, "Relative dosimetry using active matrix flat panel imager (AMFPI) technology," Medical Physics. **26**, 1530-1541 (1999). *p:10, 44, 109*

M. Essers, R. Boellaard, M. van Herk, J. H. Lanson, and B. J. Mijnheer, "Transmission dosimetry with a liquid-filled electronic portal imaging device," International Journal of Radiation Oncology Biology Physics. **34**, 931–941 (1996). *p: 8, 10*

A. V. Esch, B. Vanstraelen, J. Verstraete, G. Kutcher, and D. Huyskens, "Pre-treatment dosimetric verification by means of a liquid-filled electronic portal imaging device during dynamic delivery of intensity modulated treatment fields," Radiotherapy and Oncology. **60**, 181-190 (2001). *p: 49*

P. M. Evans, V. N. Hansen, W. P. M. Mayles, W. Swindell, M. Torr, and J. R. Yarnold, "Design of compensators for breast radiotherapy using electronic portal imaging," Radiotherapy and Oncology. **37**, 43-54 (1995). *p: 11*

C. Fiorino, A. del Vecchio, G. M. Cattaneo, M. Fusca, B. Longobardi, P. Signorotto, and R. Calandrino, "Exit dose measurements by portal film dosimetry," Radiotherapy and Oncology. **29**, 336-340 (1993). *p: 4, 9*

B. Fraass, K. Doppke, M. Hunt, G. Kutcher, G. Starkschall, and J. Van Dyke, "American Association of Physicists in Medicine Radiation Therapy Committee Task Group 53: Quality assurance for clinical radiotherapy treatment planning," Medical Physics. **25**, 1773-1836 (1998). *p: 103, 12*

L. M. Girouard, J. Pouliot, X. Maldague, and A. Zaccarin, "Automatic setup deviation measurements with electronic portal images for pelvic fields," Medical Physics. **21**, 1180-1185 (1998). *p: 4*

E. E. Grein, R. Lee, and K. Luchka, "An investigation of a new amorphous silicon electronic portal imaging device for transit dosimetry," Medical Physics. **29**, 2262-2268 (2002). *p: 7, 10, 11, 91*

P. B. Greer and C. C. Popescu, "Dosimetric properties of an amorphous silicon electronic portal imaging device for verification of dynamic intensity modulated radiation therapy," Medical Physics. **30**, 1618-1627 (2003). *p: 10*

H. F. Hare, S. W. Lippincott, D. Sawyer, J. G. Trump, E. W. Webster, K. A. Wright, W. W. Evans, and R. C. Granke, "Physical and clinical aspects of supervoltage rotational therapy," Radiology. **57**, 157-168 (1951). *p: 3*

A. G. Haus and J. E. Marks, "Detection and evaluation of localization errors in patient radiation therapy," Investigative Radiology. **8**, 384-391 (1973). *p: 2*

M. G. Herman, R. A. Abrams, and R. R. Mayer, "Clinical use of on-line portal imaging for daily patient treatment verification," International Journal of Radiation Oncology Biology Physics. **28**, 1017-1023 (1994). *p: 2*

B. J. M. Heijmen, K. L. Pasma, M. Kroonwijk, V. G. Althof, J. C. de Boer, A. G. Visser, and H. Huizenga, "Portal dose measurement in radiotherapy using an electronic portal imaging device (EPID)," Radiotherapy and Oncology. **49**, 125-132 (1995). *p: 10*

M. G. Herman, J. M. Balter, D. A. Jaffray, K. P. McGee, P. Munro, S. Shalev, M. Van Herk, and J. W. Wong, "Clinical use of electronic portal imaging: Report of AAPM Radiation Therapy Committee Task Group 58," Medical Physics. **28**, 712-737 (2001). *p: 7, 12*

International Commission on Radiation Units and Measurements, "Determination of absorbed dose in a patient irradiated by beams of X or gamma rays in radiotherapy procedures," ICRU Rep. **24**, ICRU Publications, Bethesda, Maryland (1976). *p: 2*

International Electrotechnical Commission, "Radiotherapy equipment: Coordinates, movements and scales," IEC 1217 (1996). *p: 37, 38, 88, 105*

H. E Johns and J. R. Cunningham, *The Physics of Radiology*, 4th ed. Charles C Thomas Publisher, Springfield, Illinois, 1983. *p: 89*

J. M. Johnson, M. M. Ali, and F. M. Khan, "Quality control of custom made compensators," Medical Dosimetry. **13**, 109-111 (1988). *p: 103*

S. M. Jones and A. L. Boyer, "Investigation of an FFT-based correlation technique for verification of radiation treatment setup," Medical Physics. **18**, 1116-1125 (1991). *p: 6*

F. M. Khan, *"The Physics of Radiation Therapy,"* 2nd Edition, Williams & Wilkins, Baltimore, MA (1994). *p: 11, 109, 117*

M. C. Kirby and P. C. Williams, "Measurement possibilities using an electronic portal imaging device," Radiotherapy and Oncology. **29**, 237-243 (1993). *p: 9*

M. C. Kirby and P. C. Williams, "The use of an electronic portal imaging device for exit dosimetry and quality control measurements," International Journal of Radiation Oncology Biology Physics. **31**, 593-603 (1995). *p: 10*

H. J. Kim, and R. S. Sloboda, "Image quality assurance for a Varian PortalVision™ EPID," 5th International Workshop on Electronic Portal Imaging, Phoenix, AZ. Proceedings p: 95-96, (1998). *p: 91, 92*

W. Kilby and C. Savage, "The effect of the Varian amorphous silicon electronic portal imaging device on exit skin dose," Physics in Medicine and Biology. **48**, 3117-3128 (2003). *p: 10*

M. Kroonwijk, K. L. Pasma, S. Quint, P. C. M. Koper, A. G. Visser, and B. J. M. Heijmen, "In vivo dosimetry for prostate cancer patients using an electronic portal imaging device (EPID); detection of internal organ motion," Radiotherapy and Oncology. **49**, 125-132 (1998). *p: 4, 10*

G. J. Kutcher, L. Coia, M. Gillin, W. F. Hanson, S. Leibel, R. J. Morton, J. R. Palta, J. A. Purdy, L. E. Reinstein, G. K. Svensson, M. Weller, and L. Wingfield, "Comprehensive QA for radiation oncology: Report of AAPM Radiation Therapy Committee Task Group 40," Medical Physics. **21**, 581-618 (1994). *p: 103*

H. D. Kubo, E. G. Shapiro, and E. J. Seppi, "Potential and role of a prototype amorphous silicon array electronic portal imaging device in breathing synchronized radiotherapy," Medical Physics. **26**, 2410-2414 (1999). *p: 10, 48*

K. A. Langmack, "Portal imaging," British Journal of Radiology. **74**, 789-804 (2001). *p: 5*

P. M. K. Leung, J. van Dyk, and J. Robins, "A method of large irregular field compensation," British Journal of Radiology. **47**, 805-810 (1974).

D. J. Little, L. Dong, L. B. Levy, A. Chandra, and D. A. Kuban, "Use of portal images and BAT ultrasonography to measure setup error and organ motion for prostate IMRT: implications for treatment margins," International Journal of Radiation Oncology Biology Physics. **56**, 1218-1224 (2003). *p: 4*

D. A. Low, E. E. Klein, D. K. Maad, W. E. Umflet, and J. A. Purdy, "Commissioning and periodic quality assurance of a clinical electronic portal imaging device," International Journal of Radiation Oncology Biology Physics. **34**, 117-123 (1996). *p: 89*

D. A. Low, Z. Li, and E. E. Klein, "Verification of milled two-dimensional photon compensating filters using an electronic portal imaging device," Medical Physics. **23**, 929-938 (1998). *p: 11, 12, 103, 104, 118, 178*

K. Luchka, Letter to the editor. PIPS News. **4**, 3 (2001). *p: 91*

J. E. Marks, A. G. Haus, G. H. Sutton, and H. L. Griem, "Localization error in the radiotherapy of Hodgkin's disease and malignant lymphoma with extended mantle fields," Cancer. **34**, 83-90 (1974).   *p: 2*

J. E. Marks, A. G. Haus, G. H. Sutton, and H. L. Griem, "The value of frequent treatment verification films in reducing localization error in the irradiation of complex fields," Cancer. **37**, 2755-2761 (1976).   *p: 2, 3*

K. P. Mandal, D. H. Baxter, and P. Ray, "Thin lead sheets as tissue compensators for larger field irradiation," International Journal of Radiation Oncology Biology Physics. **6**, 513-517 (1980).   *p: 103*

L. Ma, P. B. Geis, and A. L. Boyer, "Quality assurance for dynamic multileaf collimator modulated fields using a fast beam imaging system," Medical Physics. **24**, 1213–1220 (1997).   *p: 7*

B. M. McCurdy and S. Pistorius, "Photon scatter in portal images: physics characteristics of pencil beam kernels generated using the EGS Monte Carlo code," Medical Physics. **27**, 312-320 (2000).   *p: 4*

B. M. C. McCurdy, K. Luchka, and S. Pistorius, "Dosimetric investigation and portal dose image prediction using an amorphous silicon electronic portal imaging device," Medical Physics. **28**, 911-924 (2001).   *p: 10, 11, 47*

L. N. McDermott, R. J. W. Louwe, J.-J. Sonke, M. B. van Herk, and B. J. Mijnheer, "Dose-response and ghosting effects of an amorphous silicon electronic portal imaging device," Medical Physics. **31**, 285-295 (2004).   *p: 4, 49, 50*

H. Meertens, M. van Herk, and J. Weeda, "A liquid ionization detector for digital radiography of therapeutic megavoltage photon beams," Physics in Medicine and Biology. **30**, 313-321 (1985).   *p: 8*

H. Meertens, M. van Herk, J. Bijhold, and H. Bartelink, "First clinical experience with a newly developed electronic portal imaging device," International Journal of Radiation Oncology Biology Physics. **18**, 1173-1181 (1990).   *p: 3, 6*

E. Melian, G. S. Mageras, Z. Fuks, S. A. Leibel, A. Niehaus, H. Lorant, M. Zelefsky, B. Baldwin, and G. J. Kutcher, "Variation in prostate position quantification and implications for three-dimensional conformal treatment planning," International Journal of Radiation Oncology Biology Physics. **38**, 73–81 (1997).   *p: 2*

G. V. Menon and R. S. Sloboda, "Compensator quality control with an amorphous silicon EPID," Medical Physics. **30**, 1816-1824 (2003).   *p: 11, 153*

G. V. Menon, and R. S. Sloboda, "Quality assurance measurements of a-Si EPID performance," Medical Dosimetry. **29**, 11-17 (2004).   *p: 105*

P. Munro, J. A. Rawlinson, and A. Fenster, "A digital fluoroscopic imaging decice for radiotherapy localization," International Journal of Radiation Oncology Biology Physics. **18**, 641-649 (1990).   *p: 3, 7*

P Munro, J. A. Rawlinson, and A. Fenster, "Therapy imaging: A signal-to-noise analysis of a fluoroscopic imaging system for radiotherapy localization," Medical Physics. **17**, 763-772 (1990).   *p: 91*

P. Munro, "Portal imaging technology: Past, present, and future," Seminars in Radiation Oncology. **5**, 115–133 (1995).   *p: 3, 6, 7, 9, 11, 16*

P. Munro, "X-ray quantum limited portal imaging using a-Se flat panel arrays," Medical Physics. **5**, 689-702 (1998).   *p: 3*

P. Munro, "Megavoltage Radiography for Treatment Verification," in *Modern Technology of Radiation Oncology: A Compedium for Medical Physicists and Radiation Oncologists.* Chapter **13**, 481-508. ed: J. Van Dyk. Madison, WI: Medical Physics Publishing (1999).   *p: 5*

National Institute for Standards and Technology (NIST) Website (http://physics.nist.gov/PhysRefData/Xcom/Text/XCOM.html) - XCOM: Photon Cross Sections Database.   *p: 104*

J. Neilsen and S. H. Jensen, "Some experimental and clinical lights on rotation therapy, its basis and possibilities," Acta Radiologica. **23**, 51-66 (1942).   *p: 3*

A. J. Nederveen, J. J. W. Lagendijk, and P. Hofman, "Feasibility of automatic marker detection with an a-Si flat-panel imager," Physics in Medicine and Biology. **46**, 1219-30 (2001).   *p: 11, 179*

J. C. O'Daniel, L. Dong, D. A. Kuban, H. Liu, N. Schechter, S. L. Tucker, and I. Rosen, "The delivery of IMRT with a single physical modulator for multiple fields: A feasibility study for paranasal sinus cancer," International Journal of Radiation Oncology Biology Physics. **58**, 876-887 (2004).   *p: 178*

H. Parsaei, E. El-Khatib, and R. Rajapakshe, "The use of electronic portal imaging system to measure portal dose and portal dose profiles," Medical Physics. **25**, 1903-1909 (1998).   *p: 109*

K. L. Pasma, M. Kroonwijk, J. C. J. de Boer, A. G. Visser, and B. J. M. Heijmen, "Accurate portal dose measurement with a fluoroscopic electronic portal imaging device (EPID) for open and wedged beams and for dynamic multileaf collimation," Physics in Medicine and Biology. **43**, 2047–2060 (1998).   *p: 7, 10*

K. L. Pasma, M. Kroonwijk, E. B. van Dieren, A. G. Visser, and B. J. M. Heijmen, "Verification of compensator thicknesses using a fluoroscopic electronic portal imaging device," Medical Physics. **26**, 1524-1529 (1999).
p: 11, 12, 103, 104, 118, 143, 148

M. Partridge, B.-M. Hesse, and L. Muller, "A performance comparison of direct- and indirect-detection flat-panel imagers," Nuclear Instruments and Methods in Physics Research A. **484**, 351–363 (2002).   *p: 49*

194

C. R. Perryman, J. D. McAllister, and J. A. Burwell, " Cobalt 60 radiography," American Journal of Roentgenology. **83**, 525-532 (1960).   *p: 3*

PortalVision™ aS500 Rel. 6 Reference Manual, Varian Medical Systems Inc., June 2000.   *p: 30, 31, 33, 34, 35, 41, 42, 62, 64, 104*

PortalVision™ aS500 Rel.6. Customer Acceptance Procedure (CAP), Varian Medical Systems Inc., June 2000.   *p: 38*

PortalVision™ aS500 Rel.6. System Verification Summary (SVS), Varian Medical Systems Inc., June 2000.   *p: 38, 92*

PortalVision™ aS500 Rel.6. Software Installation Manual, Varian Medical Systems Inc., June 2001.   *p: 47, 49, 81*

I. Rabinowitz, J. Broomberg, M. Goitein, K. McCarthy, and J. Leong, "Accuracy of radiation field alignment in clinical practice," International Journal of Radiation Oncology Biology Physics. **11**, 1857-1867 (1985).   *p: 2*

R. Rajapakshe, K. Luchka, and S. Shalev, "A quality control test tool for electronic portal imaging devices," Medical Physics. 23, 1237-1244 (1996).   *p: 90, 91, 92*

S. Reise, N. Bleackley, E. M. Donovan, P. M. Evans, V. N. Hansen, M. Partridge, and J. R. Yarnold, "IMRT for breast radiotherapy using physical compensators and MLC," International Journal of Radiation Oncology Biology Physics. **46**, 748 (2000). *p: 103*

D. M. Roback and B. J. Gerbi, "Evaluation of electronic portal imaging device for missing tissue compensator design and verification," Medical Physics. **22**, 2029-2034 (1995).   *p: 11, 12,103, 104, 118*

D. Sheikh-Bagheri, and D. W. O. Rogers, "Monte Carlo calculation of nine megavoltage photon beam spectra using the BEAM code," Medical Physics. **28**, 2247-57 (2001).   *p: 149*

E. B. Springer, L. Pape, F. Elsner, and M. L. Jacobs, "High-energy radiography (Cobalt 60 and Cesium 137) for tumor localization and treatment planning," Radiology. **78**, 260-262 (1962).   *p: 2*

L. Spies, P. M. Evans, M. Partridge, V. N. Hansen, and T. Bortfeld, "Direct measurement and analytical modeling of scatter in portal imaging", Medical Physics. **27**, 462-471 (2000).   *p: 4, 148, 150*

M. Strandquist and B. Rosengren, "Television-controlled pendulum therapy," British Journal of Radiology. **31**, 513-514 (1958).   *p: 3*

M. Strotzer, J. Gmeinwieser, M. Volk, R. Frund, J. Seitz, C. Manke, H. Albrich, and S. Feuerbach, "Clinical application of a flat panel x-ray detector based on amorphous silicon technology," American Journal of Radiology. **171**, 23-27 (1998).   *p: 5*

195

J. C. Stroom, M. Kroonwijk, K. L. Pasma, P. C. Koper, E. B. van Dieren, and B. J. Heijmen, "Detection of internal organ movement in prostate cancer patients using portal images," Medical Physics. **27**, 452-461 (2000). *p: 10*

R. W. Swain and R. J. Steckel, "Beam localization in cobalt and megavoltage therapy during treatment," Radiology. **86**, 529 (1966). *p: 3*

W. Swindell and P. M. Evans, "Scattered radiation in portal images: A Monte Carlo simulation and a simple physical model," Medical Physics. **23**, 63-73 (1996). *p: 4, 148*

C. L. Thomason, "Implementation and clinical use of portal imaging," In: B. B. Mittal, J. A. Purdy, and K. K. Ang, editors. *Advances in Radiation Therapy.* 1st ed. Norwell, MA: Kluwer Academic Publishers; p: 66-99 (1998). *p: 42*

M. van Herk and H. Meertens, "A matrix ionization chamber imaging device for on-line patient setup verification during radiotherapy," Radiotherapy and Oncology. **11**, 369-378 (1988). *p: 8*

M. van Herk, K. Gilhuijs, P. Williams, P. Cinquin, L. Cionini, and W. Swindell, "Role of electronic portal imaging in high dose/high precision radiotherapy," Radiotherapy and Oncology. **29**, 269-270 (1993). *p: 9*

J. P. C. van Santvoort, D. Binnekamp, B. J. M. Heijmen, and P.C. Levendag, "Granulate of stainless steel as compensator material," Radiotherapy and Oncology. **34**, 78-80 (1995). *p: 103, 105*

L. J. Verhey, M. Goitein, P. McNulty, J. E. Munzenriter, and H. D. Suit, "Precise positioning of patients for radiation therapy," International Journal of radiation Oncology Biology Physics. **8**, 289-294 (1982). *p: 2*

S. Vendantham, A. Karellas, and S. Suryananayanan, "Mammographic imaging with a small format CCD-based digital cassette: physical characteristics of a clinical system," Medical Physics. **27**, 1832-1840 (2000). *p: 10*

D. Vetterli, H. Riem, D. M. Aebersold, R. H. Greiner, P. Manser, P. Cossmann, L. Kemmerling, E. J. Born, and R. Mini, "Introduction of a novel dose saving acquisition mode for the PortalVision™ aS500 EPID to facilitate on-line patient setup verification," Medical Physics. **31**, 828-831 (2004). *p: 61*

E. Vigneault, J. Pouliot, J. Laverdière, J. Roy, and M. Dorion, "Electronic portal imaging device detection of radioopaque markers for the evaluation of prostate position during megavoltage irradiation: a clinical study," International Journal of radiation Oncology Biology Physics. **37**, 205-212 (1997). *p: 10*

H. Wallman and N. Stalberg, "A television-roentgen system for pendulum therapy," British Journal of Radiology. **31**, 576-577 (1958). *p: 3*

H. Wang, T. Falco, and B. G. Fallone, "A metal screen-amorphous selenium based image receptor in megavoltage portal imaging," Medical Physics. **21**, 237-244 (1994). *p: 3*

196

B. Warkentin, S. Steciw, S. Rathee, and B. G. Fallone, "Dosimetric IMRT verification with a flat-panel EPID," Medical Physics. **30**, 3143-3155 (2003).   *p: 10*

K. J. Weeks, B.A. Fraass, and K. M. Hutchkins, "Gypsum mixtures for compensator construction," Medical Physics. **15**, 410-414 (1988).   *p: 103*

S. Webb, *"The physics of conformal radiotherapy,"* IOP Publishing Ltd, London (1997).   *p: 4*

J. R. Williams and D. I. Thwaites, *"Radiotherapy physics in practice,"* 2nd Edition, Oxford University Press, Oxford (2000).   *p: 11*

J. W. Wong, W. R. Binns, A. Y. Cheng, L. Y. Gear, J. W. Epstein, J. Klarmann, and J. A. Purdy, "On-line radiotherapy imaging with an array of fiber-optic image inducers," International Journal of radiation Oncology Biology Physics. **18**, 1477-1484 (1990).
      p: 7

J. Wu, T. Haycocks, H. Alasti, G. Ottewell, N. Middlemiss, M. Abdolell, P. Warde, A. Toi, and C. Catton, "Positioning errors and prostate motion during conformal prostate radiotherapy using on-line isocentre set-up verification and implanted prostate markers," Radiotherapy and Oncology. **61**, 127-133 (2001).   *p: 4*

F-F Yin, M. C. Schell, and P. Rubin, "A technique of automating compensator design for lung inhomogeneity correction using an electronic portal imaging device," Medical Physics. **21**, 1729-1732 (1994).   *p: 11*

M. K. Yu and R. Sloboda, "Analytical representation of head scatter factors for shaped photon beams using a two-component x-ray source model," Medical Physics. **23**, 973-983 (1996).   *p: 112*

M. K. Yu, R. S. Sloboda, and B. Murray, "Linear accelerator photon beam quality at off-axis points," Medical Physics. **24**, 233-239 (1997).   *p: 145*